FACULTY OF SCIENCE
UNIVERSITY OF COPENHAGEN

Master Thesis

Ask E. Jensen

Dilepton final states with ATLAS at $\sqrt{s} = 7$ TeV

Submitted for the degree of candidatus scientiarum

CERN-THESIS-2011-004
25/01/2011

Supervised by Stefania Xella

Acknowledgement

The work presented in this thesis could not have been achieved without the help of Mark C. Kruse, Duke University. A special thanks goes to him for contributing and giving priceless advice. A special thanks also goes out to Stefania Xella, Niels Bohr Institute, for supervising and putting time and passion into this project beyond anything that could be expected. Furthermore I want to thank the entire HEP group at NBI for the general helpfulness which exists. Many small questions have been answered with enthusiasm when they were posed. A warm thanks goes to Rasmus Mackeprang and Esben Klinkby for patient corrections and comments. Finally I would like to thank my fellow students and Ph.D's Morten, Jacob, Daniele, Troels, Pavel, Kristian, Lotte, Simon, Morten and Peter for advice, good company and adding to the unique atmosphere of the Institute.

Disclaimer

Some of the plots and tables in this thesis are based on data recorded at the ATLAS experiment during 2010. The plots represent the writer's interpretation of the data and are not officially approved by ATLAS.

Contents

Chapter 1

Introduction

Particle physics studies the smallest known constituents of Nature, the elementary particles. They constitute all matter around us and the interactions between them are best described by the very successful Standard Model of particle physics. The Standard Model describes not only the particles that constitute matter, but also the forces in Nature that govern the interactions at high energies and the particles mediating these forces. The Standard Model is one of the most extensively tested scientific models ever, but also one that is known to be inadequate, as a fundamental theory to explain everything we see in Nature. For the model to be consistent in itself a mechanism for explaining the mass of particles is yet to be found experimentally. One such mechanism requires the discovery of a new particle. This particle is the excitation of a new type of field, that eventually is needed to theoretically explain the observed mass of particles. The field is the Higgs field and the particle, the Higgs particle or simply the Higgs.

The research in particle physics entered a new era with the start of the Large Hadron Collider, LHC, a proton - proton collider of unprecedented energies. These energies allow particle physicists to probe new theories and possibly to find the Higgs if it exists. For the Higgs to be found, a profound understanding of the Standard Model processes, at these energies, is needed especially when attempting to determine the properties of it. If the Higgs is not found, other mechanisms must exist that can generate masses to particles and maybe even explain other mysteries of Nature. Once again a very detailed understanding of the multiple Standard Model processes relevant in this energy regime is needed to observe clear signs of new physics. One of the channels proposed for the discovery of the Higgs is the dilepton channel containing an electron and a muon of opposite charge stemming from the decay of a Higgs boson into a tau anti-tau lepton pair. Additionally, several searches for signs of supersymmetry involve two leptons in the final state.

The study of this thesis was developed as a more global mean of understanding the contribution from the Standard Model to these physics searches. The idea was developed in the CDF experiment at the Tevatron and presented in [1] but has been evolved for the ATLAS experiment at the LHC in this thesis. The analysis starts from the requirement of two high-P_T leptons, after which all processes that can contribute are considered. The only other objects that can exist in these events are neutrinos, that result in missing transverse momentum, $\not{E}_T$, and jets from decay of hadrons, from radiated gluons or from remnants of the colliding protons. This motivates a simple fit of the $\not{E}_T$ vs. N_{jets} 2-D distribution from data to those from the expected Standard Model contributions in order to extract the cross sections from these contributions on a small, initial data sample. Eventually this fit can spot signs of new physics as data is accumulated. The processes that contribute significantly to final states of two high P_T leptons will constitute backgrounds for discovery of e.g. the Higgs, making them important to study.

The fitting of cross sections from the most significant Standard Model contributions in the $\not{E}_T$ vs. N_{jets} space is expected to work well as the main contributions lie in different regions, due to their different sources of $\not{E}_T$ and jets.

The main contributions come from $t\bar{t}$, WW, and $Z \rightarrow \tau\tau$ production. It is the cross section of these three processes we measure with a relative simple analysis. Additionally we have background sources, that will act as noise to the three processes.

This study has the huge advantage over exclusive cross section measurements of single processes, that the only selection needed is the selection of a real electron and muon coming from one of the given signals. This means a much larger amount of events pass the final selection giving much better statistics.

As an understanding of the Standard Model processes is central to the thesis, the first chapter of the thesis will describe the theory of the Standard Model and the Higgs field. This part will describe the particle interactions and symmetries, that govern them.

The second chapter will be dedicated to the transition from theory to experiment. In the world of particle physics, analytical theoretical calculations alone are not capable of predicting what will be observed by particle detectors at the higher collision energies physicists now face. Simulations of proton - proton collisions, with the help of perturbative calculations, including detailed detector descriptions, are fundamental for understanding what we observe.

The actual fit of the three processes will be made against predictions of their contribution in the $\not{E}_T$ vs. N_{jets} space provided by such simulations and a part of the thesis has for this reason been dedicated to the study of these generators and the reconstruction of the events they predict.

The two final parts concern the results of these predictions and the actual fit of them against a control sample and against real data recorded at the ATLAS experiment during the fall of 2010. The fit to Monte Carlo generated pseudo-data is published in [2]

Part I

Theory and experiment

Chapter 2

Theory

2.1 The Standard Model

The Standard Model (SM) is the fundamental theory describing the smallest known constituents of our universe, the elementary particles and the forces that govern their interactions. In Nature one finds two kinds of particles: the matter particles called fermions and the force carriers called bosons.

2.1.1 Fermions - What is the matter?

The fermions are characterised by carrying spin-$\frac{1}{2}$ and make up all matter as we know it today. The matter particles are split into two categories: leptons and quarks. The most well known leptons are probably the electrons. Electrons have electromagnetic charge $-1e$, where e is the elementary charge. Besides the electron another lepton exists named the neutrino. The neutrino has no electromagnetic charge and very seldom interacts with other particles. In fact 10^6 neutrinos pass through each square centimetre of the earth each second or in other words, millions of neutrinos pass through the nail of your thumb while reading this.

In 1933 the first particle of the same mass as the electron, but with opposite charge, was found by C.D. Anderson in a Wilson cloud chamber. The particle was a positron, an anti-particle in all ways looking identical to the electron, but with opposite electromagnetic charge.

The other type of elementary fermion is the quark. Neutrons and protons, that make up the nuclei of all known chemical elements, are composed of *up* and *down* quarks. Two up quarks and a down quark makes a proton while two down and one up-quark constitute a neutron. While the neutron is neutral, the proton has an electromagnetic charge of $+1e$. This charge comes from the fact, that the individual quarks have fractional electromagnetic charge, that add up when combined into a nucleus.

Quarks also have two other types of charge related to the forces acting within the nucleus. They are called weak and strong charge, with the latter often being referred to as the colour charge. Quarks are strongly bound by the colour charge, and cannot exist freely. Instead they combine with other quarks to form what is called hadrons. Hadrons can be split into two categories: mesons where a quark and an anti-quark form a bound state, and baryons, like the neutron and proton, where three quarks combine to form a bound state.

These four particles (e,ν,u,d) and their anti-particles can almost explain everything of what we see around us in everyday life, but the particle world is much richer and a variety of particles become evident, once matter is probed at higher and higher energies (or equivalently, at smaller and smaller length scales). There are in fact three generations of fermions, which can be brought to evidence in laboratory experiments e.g. by colliding particles like electrons or protons at high energies. They have all been listed in Tab. 2.1 with names, symbols, mass and different charges. For quarks and leptons, these charges are quantum numbers defining their interactions. The masses are listed in MeV, $10^6 electronvolts$. The value of one electron volt, eV, is the equivalent of the energy gained by an electron accelerated over a potential of one Volt.

fermions

	Particle name	symbol	EM charge	Weak charge (isospin)	strong charge (colour)	Mass [MeV]
Leptons	electron	e	-1	- 1/2	0	0.511
	electron neutrino	ν_e	0	+ 1/2	0	$\leq 50 \cdot 10^{-6}$
	muon	μ	-1	$-1/2$	0	105.6
	muon neutrino	ν_μ	0	$+1/2$	0	≤ 0.5
	tau	τ	-1	$-1/2$	0	1784
	tau neutrino	ν_τ	0	$+1/2$	0	≤ 70
Quarks	up	u	$+2/3$	+ 1/2	R/G/B	$\sim$5
	down	d	$-1/3$	$-1/2$	R/G/B	$\sim$10
	charm	c	$+2/3$	$+1/2$	R/G/B	$\sim$1500
	strange	s	$-1/3$	$-1/2$	R/G/B	$\sim$100
	top	t	$+2/3$	$+1/2$	R/G/B	$178 \cdot 10^3$
	bottom	b	$-1/3$	$-1/2$	R/G/B	$\sim$ 4700

bosons

	photon	γ	0	no	no	0
	Z	Z	0	yes	no	$91.187 \cdot 10^3$
	W	$W^\pm$	± 1	yes	no	$80.39 \cdot 10^3$
	gluon	g	0	no	yes	0
	Higgs	H^0	0	yes	no	$\geq 114 \cdot 10^3$

Table 2.1: Constituent particles of the Standard Model

2.1.2 Bosons and the fundamental forces

The world has four fundamental forces governing the interaction between particles. The electromagnetic force, the weak and strong nuclear forces, and gravity. A fundamental theory of our world must thus incorporate all four forces.The Standard Model describes three of these forces through their particle carriers - the bosons.

From electrodynamics and Maxwells equations in classical physics, we know, that particles can interact with each other via the electric and magnetic fields. The Standard Model description of electromagnetic interactions between two particles is the exchange of photons. These photons are virtual spin 1 particles that carry the information between the particles, that they are attracted to or repelled from each other by an electromagnetic field. Likewise the weak force is mediated by Z and W bosons while the strong force is mediated by gluons.

Although a graviton has been proposed as the mediator for gravity it has not been observed so far, and is not part of the Standard Model. There is currently no framework for explaining the gravity as part of the Standard Model.

Another particle not observed yet but proposed for the Standard Model is called the Higgs boson. The Higgs boson is the physical resonance of the Higgs field - a field introduced to explain how particles acquire mass. The interaction between the different forces have been visualised in Figure 2.1. A more thorough description of the Higgs mechanism is given later.

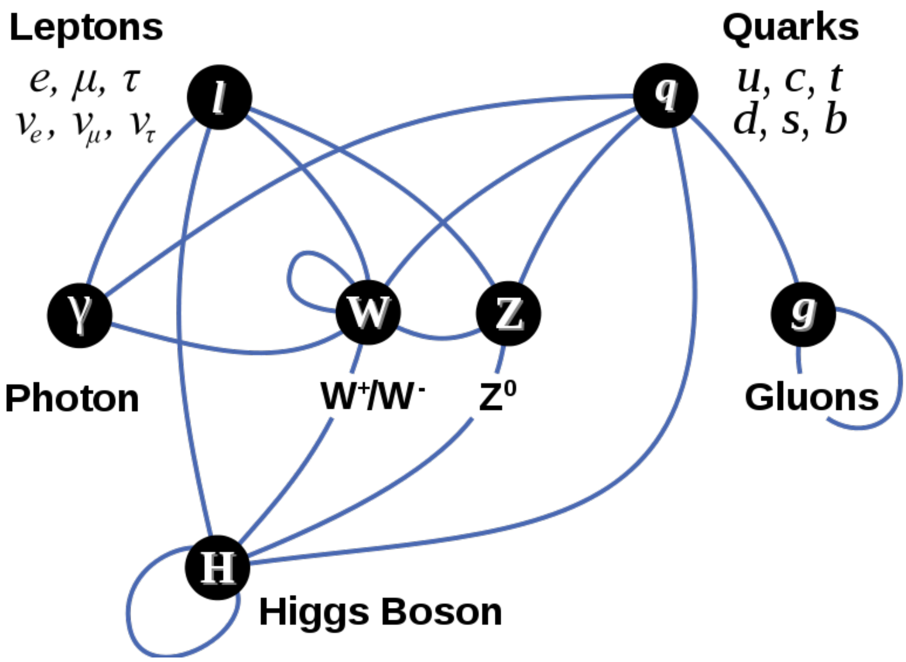

Figure 2.1: The particles in the Standard Model and the interaction governing them are illustrated here. The bosons only interact with particles that carry charge corresponding to the force they mediate. The gluons therefore only interact with quarks and other gluons, as all other particles have zero colour charge, while the W interacts with all particles except gluons, as gluons do not carry weak isospin. It should be noted that the photon only couples to the charged leptons.

2.2 Symmetries of the Standard Model

The particles and interactions presented above add up to what one could call the botanics of the Standard Model. The Standard Model description of particles and forces in Nature is based on the language of the quantum theory of fields, where particles are excitations of fundamental fields. The approach to constructing a valid quantum field theory, to describe natural phenomena at the particle scale, is that it must obey certain symmetries. These symmetries translate into conservation of observables like charge or momentum. The approach is closely connected with a deeper philosophy for understanding Nature.

As for all relativistic field theories, the Standard Model fulfils global Pointcaré symmetry. This consists of the well known translational symmetry, rotational symmetry and the inertial reference frame invariance central to the theory of special relativity. Within the Pointcaré symmetry energy, momentum and angular momentum are conserved. Discrete symmetries play an important role in governing the interactions of particles. Discrete symmetries are symmetries, that describe non-continuous changes in a system like reflection of space coordinates or interchange of charge. For the Standard Model the discrete operators for *charge* and *parity* behave symmetrically. Charge parity changes the electromagnetic charge of the particle while Parity is a spatial transformation. Finally time reversal (T-parity) can be imposed. In short the Standard Model requires CPT invariance, demanding that a system transformed under C,P and T must be invariant. The transformation of a particle under CPT turns it into its own anti-particle. Furthermore an internal gauge symmetry namely the local SU(3)xSU(2)xU(1) *gauge* symmetry defines the Standard Model. Imposing this symmetry on quantum field theory results in description of Nature at the particle level called the Standard Model, which is the best we have of today. The development of the final form of these field theories is closely related to the principles of least action and gauge invariance.

The following attempts to give a brief insight into this framework with focus on the interesting principles involved. For the interested reader a more in-depth study can be found in the excellent textbook [3]

2.2.1 Gauge invariance

In the framework of quantum field theory, particles can, contrary to the point-particles of classical mechanics, be described as the quantised excitations of fields. The description of fields is most commonly recognised from the description of light: the photon exhibiting both wave- and particle-properties. The description of the quantisation of the electromagnetic field into photon quanta was one of two pillars [4] of the development of a field description of Quantum Electro Dynamics, QED [5]. The second pillar is the relativistic theory of the electron, with the Dirac equation in its centre.

In quantum field theory when trying to formulate a description of natural phenomena a central concept to understand is *gauge* invariance. In classical mechanics the fundamental quantity is the action, S. It contains all the information needed to determine the dynamics and kinematics of a system, and is found by time integrating the Lagrangian. The Lagrangian is here the spatial integral of the Langrangian density, $\mathcal{L}$.

$$S = \int L dt = \int \mathcal{L} d^4x = \int (T - V) dt, \tag{2.1}$$

where T is kinetic energy and V is potential energy of the system. The term gauge refers to an excess degree of freedom in the Lagrangian. Transformation between different *gauges* form a symmetry group called the gauge group of the theory. The transformations are called *gauge transformations*. Basically gauge invariance means that if the physical predictions of a theory remain unaltered by a local or global transformation, then the theory is gauge invariant. A gauge invariant Lagrangian is thus invariant under

$$\psi(x) \rightarrow e^{i\alpha}\psi(x), \tag{2.2}$$

where ψ is an arbitrary field and α its phase. α is unmeasurable and can be chosen arbitrarily but as soon as it is fixed, it is specified for all points in space-time and it forms a global gauge transformation. If α is dependant on space time e.g. $\alpha(\mathbf{x})$, it forms a local gauge symmetry. The demand of invariance of the wave equations under gauge transformations is a key step in getting a theory that can describe Nature.

Principle of least action

In classical mechanics a system making a transition from one state to another does so along the path in configuration space, where the action is a minimum. This principle is called the principle of least action. In other words, the classical system will always take the shortest *path* in space-time. The extremum is found by varying the action with regard to a field like the above $\psi(x)$, with the demand, that these variations vanish for a given set of boundary conditions, that correspond to the inherent physics. This gives the Euler-Lagrange version of the equation of motions for that field $\psi(x)$. This principle is not necessarily true when moving to quantum mechanics. The classical path is only one of the paths, and in principle all other paths are allowed. The classical path is however often the dominant path but those close to it, e.g. *quantum fluctuations* can influence the results significantly. We can probe these small fluctuations and get a new form of our Lagrangian.

The dynamics of a fermion field like the electron, $\psi(\mathbf{x})$ are expressed by the Dirac Lagrangian[1]

$$\mathcal{L}_{Dirac} = \bar{\psi}(\mathbf{x})(i\gamma^\mu \partial_\mu - m)\psi(\mathbf{x}) \tag{2.3}$$

It is interesting to try to make a gauge transformation on this equation. The partial derivative will transform as

$$\partial_\mu \to D_\mu = \partial_\mu - iqA_\mu, \tag{2.4}$$

where A_μ is the gauge field. This must, due to gauge invariance, transform along with $\psi(\mathbf{x})$ by a simple phase transformation

$$\psi(\mathbf{x}) \to e^{i\alpha(\mathbf{x})}\psi(\mathbf{x}) \qquad \text{and} \qquad A_\mu(\mathbf{x}) \to A_\mu(\mathbf{x}) + \frac{1}{e}\partial_\mu \alpha(\mathbf{x}), \tag{2.5}$$

Here e is the elementary charge. When this is done, the Dirac Lagrangian changes form and can be written as

$$\mathcal{L} = \bar{\psi}(\mathbf{x})(i\gamma^\mu \partial_\mu - m)\psi(\mathbf{x}) - \mathcal{L}_{int}, \tag{2.6}$$

where $\mathcal{L}_{int}$ is the interaction part of the Lagrangian given by

$$\mathcal{L}_{int} = -e\bar{\psi}(\mathbf{x})\gamma^\mu \psi(\mathbf{x}) A_\mu \tag{2.7}$$

The field A_μ can obviously be interpreted as the photon field, but it cannot propagate in its current form, as it has no kinematic degree of freedom. To give the field the ability to propagate as desired, we impose terms containing first order derivatives in time to our Lagrangian. By imposing simply gauge invariance this gives a series of terms which is unsatisfactory, but by the introduction of P parity, we are left with one allowed term

$$\mathcal{L} = -\frac{1}{4}F^{\mu\nu}F_{\mu\nu} \tag{2.8}$$

for the electromagnetic field strength tensor

$$F_{\mu\nu} = \partial_\nu A_\mu - \partial_\mu A_\nu \tag{2.9}$$

[1] Obviously this is the Lagrangian density, but as is customary in the field's notation, it is henceforth simply referred to as the Lagrangian.

The addition of a mass term is not allowed by the demand of gauge invariance so this is the final form of the quantum electrodynamic Lagrangian given in full by

$$\mathcal{L}_{QED} = \bar{\psi}(\mathbf{x})(i\gamma^{\mu}D_{\mu} - m)\psi(\mathbf{x}) - \frac{1}{4}F_{\mu\nu}F^{\mu\nu} \tag{2.10}$$

QED embodies the imposition of a U(1) gauge symmetry on a field theory of fermionic fields. The gauge field is the electromagnetic field and the symmetry of the group demands electric charge conservation and, as it is part of the Standard Model, it means charge must always be conserved in particle interactions.

The mass term here is the fermion mass term introduced by the Dirac Lagrangian. It has not been explained and is indeed put in by hand without explanation of its origin.

2.2.2 Feynman diagrams

The description of the particle dynamics through their action can be beautifully expressed through a series of surprisingly simple pictorial rules. The calculations are based on the interaction part of the action. The amplitude of this part of the interaction can be denoted by a matrix, $\mathcal{M}$, or the more applicable squared matrix, $|\mathcal{M}|^2$ used in the calculation of cross sections and decay probabilities. The assumption is made, that, the interaction part is weak and can be perturbed around the classical solution.

The Feynman rules describing this are calculated, as mentioned, pictorially. More precisely a type of line is drawn representing each kind of particle (the propagator) and each vertex represents the coupling between the particles meeting in that vertex. An example of a Feynman diagram can be seen in Fig. 2.2a. Here the t-axis represents displacement in time while the s-axis represents displacement in space. The figure shows the scattering of two fermions described by the interaction part of the Lagrangian in Eq. 2.10 when interpreting $\psi(\bar{\psi})$ as the representation of the electron (positron) and A_{μ} as the photon. Figure 2.2b might seem identical to Fig. 2.2a but when keeping in mind, that time goes along the t-axis, it will be clear, that the diagram represents a different physical process described by the same Lagrangian. The first is the interaction (scattering) of an electron on a positron through the emission/absorption of a photon, while the second is the annihilation and pair-creation of an electron-positron pair through a photon. The Feynman diagrams can always be read as a sum of particles coming in from the left and a set of possibly new particles emerging from the right after the interaction has happened.

In this simple description of the interactions of particles, anti-particles can be interpreted as moving backwards in time. For a thorough explanation of this the reader is referred to [3]. Fig. 2.2c shows a loop on the photon propagator from Fig. 2.2b. To calculate full amplitudes from processes the diagrams have to be evolved with regard to coupling constants of the forces involved. To include these higher order corrections all possible diagrams have to be taken into account. Generally diagrams like Fig. 2.2a and 2.2b, that are of leading order, are referred to as *tree* level diagrams while diagrams as Fig. 2.2c are referred to as *loop* diagrams.

When discussing higher order Feynman diagrams it should be noted that for a calculation of the physical cross section, the probability for the process to happen given two incoming particles, an integration over the momentum in the loop will be necessary. These loops can however contain infinite momenta resulting in meaningless integrals. These infinities lead to an important understanding of physics.

In order to solve the problem, renormalisation is used to redefine mass and charge, so the theory contains only measurable quantities. As a result of this, the energy scale now influence

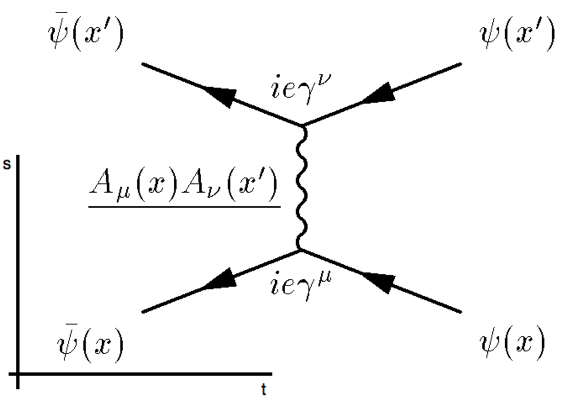

(a) A Feynmann diagram of the scattering of two fermions each described by a Lagrangian like in Eq. 2.10.

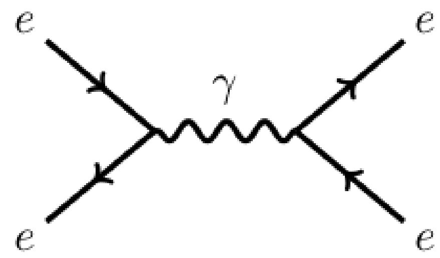

(b) Feynman diagrams representing the annihilation of an electron-positron pair into a photon and creation of a new electron-positron pair.

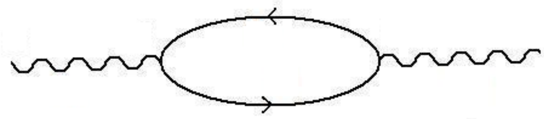

(c) Feynman diagram showing a loop integral as will have to be taken into account for higher order corrections.

Figure 2.2: Different Feynman diagrams

the observed quantities and the theory can retain its predictive power. A gauge invariant quantum field theory like the Standard Model is a renormalisable theory. For a description of renormalisation and the mechanisms involved we refer to [6] or [3].

2.3 The Electroweak theory

Continuing on the success of electromagnetic quantum field theory, electroweak theory [7] attempts to incorporate electromagnetic and weak force into a theoretical description using the idea of local gauge invariance.

As QED could be described with the symmetry of the unitary group U(1), a group exists that combine the description of QED with the description of the weak force. It forms a gauge group of *electroweak* interactions that has a $SU(2)_{I_W} \times U(1)_Y$ structure. This is broken into the $U(1)_{EM}$ symmetry by electroweak symmetry breaking as will be explained. Y is weak hypercharge, I_W is weak isospin and I_W^3 its third component. They are related to the electric charge from QED by

$$Q = \frac{Y}{2} + I_W^3 \tag{2.11}$$

With respect to this weak isospin, the left handed fermions can be arranged in the doublet structure of leptons and neutrinos or up-type and down-type quarks. Right-handed fermions are invariant under transformation of weak isospin which means they do not couple to it, and are therefore singlets under $SU(2)_{I_W}$. They both however couple to weak hypercharge. This equation is central for the understanding of the SM interactions. Weak hypercharge is defined as follows

$$Y \equiv B + X, \tag{2.12}$$

where B is the quantum number called baryon number and X represents a set of quantum numbers for each type of quark. There is a similar quantum number for the leptons demanding conservation of electron, muon and tauon numbers e.g. $L_e \equiv N(e^-) - N(e^+) + N(\nu_e) - N(\bar{\nu}_e)$

Along with the lepton number [8], these numbers govern the possible decays and production mechanisms of all particles. The conservation of charge from QED has thus been extended by the conservation of the third component of isospin and baryon/lepton number conservation from hypercharge. An example of these conservation laws could be the decay of Z to a lepton and pions through taus.

$$Z \rightarrow \tau^+ + \tau^- \rightarrow e^+ + \bar{\nu}_\tau + \nu_e + \pi^- + \nu_\tau. \tag{2.13}$$

First of all charge is conserved, as the neutral Z decays into two taus of opposite charge, that again decay to a positron and a negatively charged pion. Lepton number is conserved, as τ^+ and τ^- have lepton numbers 1 and -1 for the first part. The decay of each tau also has conserved lepton numbers due to the neutrinos present in the decay. The anti-tau neutrino conserves the τ^+ lepton number and vice versa, while the positron is opposed by the electron neutrino. Baryon numbers are conserved as the pion is made of an antiup- and a down-type quark.

The bosons of the electroweak interactions stems from the description of the $SU(2)_{I_W} \times U(1)_Y$ by an isotriplet $W_\mu^{1,2,3}$, and a massless isosinglet, B_μ. Special unitary groups like the SU(2) are described by the so called Lie algebra [9]. The group has generators, T_i that are proportional to the Pauli matrices σ_i:

$$\sigma_1 = \begin{pmatrix} 0 & 1 \\ 1 & 0 \end{pmatrix}, \quad \sigma_2 = \begin{pmatrix} 0 & -i \\ i & 0 \end{pmatrix}, \quad \sigma_3 = \begin{pmatrix} 1 & 0 \\ 0 & -1 \end{pmatrix} \tag{2.14}$$

Because the Pauli matrices do not commute with each other the W_μ fields have, in addition to their kinetic energy, a contribution from their self-interaction [10]

$$W_{\mu\nu} = \partial_\mu W_\nu - \partial_\nu W_\mu - g W_\mu \times W_\nu. \tag{2.15}$$

Here g is the coupling constant between the left handed fermions and the weak isospin via $W_\mu^{1,2,3}$. It is related to g' - the coupling between fermions and the weak hypercharge - through B_μ, the weak mixing angle θ_W and the elementary charge, e, by

$$g \cdot \sin\theta_W = g' \cos\theta_W = e \tag{2.16}$$

For the B_μ field there exist no self-interactions and the kinetic energy is simply described by

$$B_{\mu\nu} = \partial_\mu B_\nu - \partial_\nu B_\mu. \tag{2.17}$$

These fields enter in a Lagrangian of the form

$$\mathcal{L}_{EW} = \mathcal{L}_g + \mathcal{L}_f \tag{2.18}$$

The first term $\mathcal{L}_g$ describes the interactions between the $W_\mu^{1,2,3}$ particles and the B_μ particle. The second term $\mathcal{L}_f$ describes the kinetic term for the Standard Model fermions. $\mathcal{L}_g$ is given by

$$\mathcal{L}_g = -\frac{1}{4}W_a^{\mu\nu}W_{\mu\nu}^a - \frac{1}{4}B^{\mu\nu}B_{\mu\nu}, \tag{2.19}$$

while $\mathcal{L}_f$ is given by

$$\begin{aligned}\mathcal{L}_g = \; & +i\bar{L}\gamma^\mu\partial_\mu L + i\bar{R}\gamma^\mu\partial_\mu R \\ & -g\bar{L}\gamma^\mu\vec{T}\cdot W_\mu L \\ & -g'\tfrac{Y}{2}\bar{L}\gamma^\mu B_\mu L - g'\tfrac{Y}{2}\bar{R}\gamma^\mu B_\mu R\end{aligned} \tag{2.20}$$

Here L is an arbitrary left-handed fermionic $SU(2)_{I_W}$ doublet and R its corresponding right-handed singlet. We know from observation, that particles hold mass but simply introducing mass terms into the Lagrangian would explicitly break gauge symmetry. Instead the mass terms are obtained by introducing the mechanism of spontaneous symmetry breaking.

2.3.1 Spontaneous symmetry breaking

To generate masses a scalar field ϕ is added to the SM. This is the Higgs field, introduced by Peter Higgs[2] in 1964 [11]. In the Lagrangian, it contributes with a term of the form

$$\mathcal{L}_\psi = \left|\left(i\partial_\mu - g\vec{T}\cdot W_\mu - g'\frac{Y}{2}B_\mu\right)\phi\right|^2 - V(\phi), \tag{2.21}$$

describing the kinetic energy and interaction term of the scalar field ϕ with $W^{1,2,3}$ and B_μ fields. $\vec{T}$ are the SU(2) generators related to the Pauli matrices by $T_i = \frac{1}{2}\sigma_i$. The last term is a potential which is given by

$$V(\phi) = \mu^2\phi^\dagger\phi + \lambda(\phi^\dagger\phi)^2 \tag{2.22}$$

The Lagrangian obviously still has to be gauge invariant and it has to break the $SU(2)_{I_W} \times U(1)_Y$ symmetry so masses are generated. This means, that the ground state must have non-vanishing values for hypercharge and weak isospin but cannot be electrically charged e.g. $0 = \frac{Y}{2} + I_W^3$. The simplest choice is a scalar with weak hypercharge $Y = 1$ and weak isospin $I_W = \frac{1}{2}$

$$\phi = \frac{1}{\sqrt{2}}\begin{pmatrix}\phi_1 + i\phi_2 \\ \phi_3 + i\phi_4\end{pmatrix} \tag{2.23}$$

Now a looking back at Eq. 2.22 first of all λ has to be positive as the energy of the ground state should be finite. Choosing $\phi = 0$ is tempting, but this choice will not allow for the generation of mass terms, so furthermore μ^2 has to be negative. This will give an infinite number of equally likely states at lowest energy. These states will have non-vanishing expectation value, ν. The final choice of ground state is assumed to be randomly selected by Nature to be one of the minima of the potential. The idea is represented in Fig. 2.3. After the selection of ground state, the symmetry is broken. The ground state has to yield the correct mass relations and

[2] the Higgs mechanism was in general developed by different people independently and could also be referred to as the Englert-Brout-Higgs-Guralnik-Hagen-Kibble mechanism. The application of the Higgs mechanism was in fact done by Steven Weinberg and Abdus Salam.

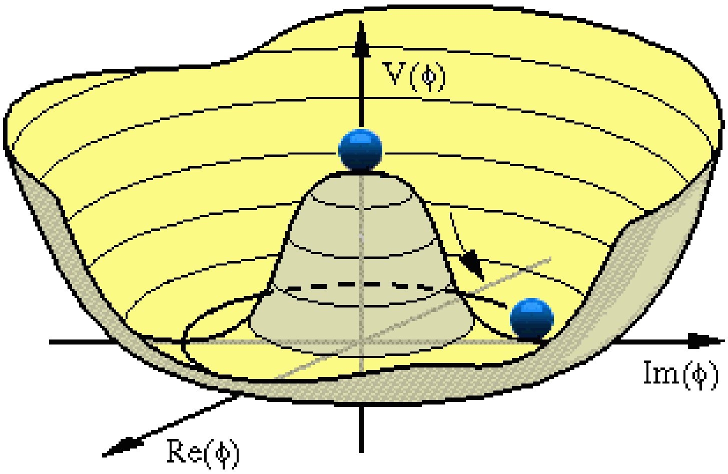

Figure 2.3: The Higgs potential depicted in two degrees of freedom. The $\phi = 0$ state of the field is not stable as is obvious and a ground state is only found after Nature "rolls the ball to side" e.g. selects on of the minima of the potential as physical ground state, thus breaking the symmetry.

break symmetry as well as be invariant under the $U(1)_{EM}$ symmetry so that $Q\phi_0 = 0$. One choice that fulfils this is

$$\phi_0 = \frac{1}{\sqrt{2}} \begin{pmatrix} 0 \\ \nu \end{pmatrix} \tag{2.24}$$

The Higgs mechanism

With the breaking of the symmetry of $SU(2)_{I_W} \times U(1)_Y$ one also has to take into account the existence of massless Goldstone bosons. For each broken generator there exist a massless scalar Goldstone boson. Since the $U(1)_{EM}$ symmetry remains unbroken, three generators are broken, and three Goldstone bosons are created. They are without physical degrees of freedom and their influence on ϕ is seen when parametrising the fluctuations of vacuum in terms of the Goldstone field $\vec{\theta}$ and the Higgs field, h

$$\phi(x) = \frac{1}{\sqrt{2}} e^{i\vec{\sigma}\cdot\vec{\theta}(x)/\nu} \begin{pmatrix} 0 \\ \nu + h(x) \end{pmatrix} \tag{2.25}$$

But as the theory must be gauge invariant any gauge transformation that simply change the "phase" is allowed. The freedom of these Goldstone bosons can be transformed into the longitudinal degree of freedom of the now massive weak bosons in such a gauge transformation where $e^{i\vec{\sigma}\cdot\vec{\theta}(x)/\nu} \to \mathbf{1}$ [12]. This is what is known as the Higgs mechanism. After the transformation the Goldstone fields vanish from the theory and we are left with one massive scalar boson, the Higgs, along with the Higgs field, h

$$\phi(x) = \frac{1}{\sqrt{2}} \begin{pmatrix} 0 \\ \nu + h(x) \end{pmatrix} \tag{2.26}$$

Now it is finally possible to extract equations for the mass eigenstates of Z_μ and A_μ. This is done by introducing the form of the ϕ field from Eq. 2.26 into the Lagrangian from Eq. 2.21.

This yields the following terms relevant for the generation of masses [10]

$$\left|\left(-ig\vec{T}\cdot W_\mu - ig'\frac{Y}{2}B_\mu\right)\right|^2 = (\frac{1}{2}\nu g)^2 W_\mu^+ W^{\mu-} + \frac{1}{8}\nu^2[gW_\mu^3 - g'B_\mu]^2 \tag{2.27}$$

The mass eigenstates becomes

$$W_\mu^\pm = \sqrt{\frac{1}{2}}(W_\mu^1 \mp iW_\mu^2) \tag{2.28}$$

$$A_\mu = B_\mu \cos\theta_W + W_\mu^3 \sin\theta_W \tag{2.29}$$

$$Z_\mu = -B_\mu \sin\theta_W + W_\mu^3 \cos\theta_W \tag{2.30}$$

and the masses

$$\begin{aligned} M_W &= \tfrac{1}{2}\nu g \\ M_Z &= \tfrac{1}{2}\nu\sqrt{g^2+g'^2} \\ M_A &= 0 \end{aligned} \tag{2.31}$$

with the ratio $M_W/M_Z = cos\theta_W$. The vacuum expectation value, ν, of the potential can be found to be 246 GeV but apart from this, the absolute masses of the W and Z bosons are not predicted by the theory. As a side note the mass of the Higgs bosons also comes out of the Lagrangian

$$M_h = \nu\sqrt{2\lambda} \tag{2.32}$$

This cannot be determined theoretically as λ is not known but experimental limits have already been set. The LEP experiments [13] were sensitive to a Standard Model neutral Higgs with a mass up to 115 GeV and yet they did not find the Higgs, thus setting a lower bound on the mass. The mass of the Higgs is limited to around 1 TeV for various theoretical reasons. Demanding that λ is finite at infinitely large energy scales means it will approach zero at small energy scales rendering the theory trivial, as the Higgs coupling vanishes and no symmetry breaking occurs. From this it is clear, that there exist a maximum scale to which the theory is valid. Inserting e.g. the Planck scale into the equation for the Higgs mass as the energy scale yields a Higgs mass of 190 GeV [10]

2.3.2 Quantum Chromodynamics

The Electroweak theory does not form the complete theory known as the Standard Model, since we are still missing a description of strong interactions. To complete the theory of particle interactions, we will add another gauge group. This group represents the strong interactions and has gauge symmetry group SU(3). The theory is known as Quantum Chromo Dynamics or simply QCD [14], as it is the *colour charge* that defines the local symmetry.

The development of QCD takes root in the gauge transformation but is extended by the addition of a change in the phase of the wavefunction, and also in a new quantum number called - the colour state. The symmetry of the SU(3) group is mediated by the gluons and act on the different colours of the quarks. Besides this an approximate symmetry called the flavour SU(3) exists. This symmetry rotates different flavours of quarks to each other.

The gluons mediating the strong force can be described by a field strength tensor like $F^{\mu\nu}$ as we saw in QED. For gluons the gauge invariant gluonic field strength tensors are given by

$$G^a_{\mu\nu} = \partial_\mu G^a_\nu - \partial_\nu G^a_\mu - g f^{abc} G^b_\mu G^c_\nu \tag{2.33}$$

where G^a_ν are the space-time dependent gluon fields, f^{abc} is a structure constant from SU(3) and g is the coupling constant of the theory. The gauge invariant form of the QCD Lagrangian is given by

$$\mathcal{L}_{QCD} = \bar{\psi}_i (i\gamma^\mu (D_\mu)_{ij} - m\delta_{ij})\psi_j - \frac{1}{4} G^a_{\mu\nu} G^{\mu\nu}_a \tag{2.34}$$

Here ψ is the quark field as a function of space-time, and γ^μ are the Dirac matrices. m is a mass constant that together with the coupling g is subject to renormalisation in the full quantum field theory. The theory allows for three basic interactions: a quark may emit (or absorb) a gluon, a gluon may emit (or absorb) a gluon, and two gluons may interact directly creating a four-gluon vertex in Feynman notation. The interactions between gluons are in contrast to the behaviour of photons in QED. Since the photons have no charge, self-interactions does not happen between photons.

The theory is seen to be quantised into the already mentioned force carriers *gluons*. If two quarks are separated a gauge field of gluon self-interactions form between them and the energy needed to separate two particles will grow proportionally to the distance of the separation. This means, that the strong force is weak at short distances but rises quickly to become very strong with separation of two quarks. The phenomenon is known as colour confinement for large distances (small energy) and asymptotic freedom for short distances (large energy). For the framework of Feynman diagrams the force is weak enough due to asymptotic freedom, to allow for a perturbative theory. It also means that the theory is not perturbative at larger distances (lower energies).

Colour confinement plays a crucial role in experiments, because it means particles with colour charge can never exist freely beyond the initial collision. Virtual Quark-antiquark pairs will thus materialise around single quarks forming bound states, that result in jets of particles moving out through the detector. The process is known as hadronisation and will be described later.

2.4 Strengths and weaknesses of the Standard Model

To round off the Standard Model section a short discussion of the strengths and weaknesses of it is in order. On the bright side, the Standard Model is one of the most precisely tested theories in the history of science yielding great breakthroughs like the combination of the weak and electromagnetic forces in one force, the electroweak force. It describes the strong force through the gluons and combines the three forces in a gauge theory that is the best description we have of observations in physics so far. If the Higgs is found, it explains the masses of the particles and the Standard Model would to a certain degree be a consistent theory.

On the downside, the Standard Model leaves a lot of open questions. One of them is the question of the origin of the fourth force, gravity and an understanding of its nature. The idea that all forces should stem from one force at the ultra-high energies present at the earliest fractions of a second in the Big Bang is known as the Theory of Grand Unification, GUT, and is a simple and beautiful idea appreciated by many physicists. This does however not seem to be possible in the SM as the coupling of the forces, i.e. their relative strength, simply do not meet when extrapolated to higher energies.

Another huge question is the lack of symmetry between matter and antimatter in the universe. Some mechanisms in the Standard Model can cause violation of the charge-parity symmetry (CP), which would explain the asymmetry. Examples of this are the decay of neutral kaons and the possibility of neutrinos with mass as anticipated by observations. None of these processes can however explain the degree of imbalance there seems to exist between matter and antimatter. Without such a mechanism matter and anti-matter should naively have been created in equal amounts in our universe.

In the next years we will hopefully find the answers to some or all of these questions, but in order to answer any of them a profound understanding of what can be expected from the Standard Model physics processes at the LHC proton proton collisions is needed. The Standard Model is extremely well tested at the energies of current experiments, but extrapolating the results to higher energies is not yet well understood.

Chapter 3

From theory to experiment

3.1 Cross section calculations

The analysis presented in this thesis will try to estimate the contributions from different Standard Model processes to a sample of data containing an electron and a muon of high P_T and opposite charge. The contribution of any process is described by its cross section, the probability, that the specific interaction will occur given a collision rate. Calculating cross sections for particles in proton - proton collisions relevant for this study like $\sigma(pp \to Z/\gamma* \to \tau\tau \to e\mu + \nu' s)$ is by no means a trivial affair. The difficulty lies in the fact that we start from two protons and not two partons. The next chapter will concern the calculation of the parton - parton interaction but following that we need to take into account that each parton type in the proton contributes with a weight given by the probability of such parton to carry a certain fraction of the momentum of the proton (- the so called parton distribution function). If we make the assumption that the non-perturbative part i.e. what goes on in the proton can be factorized from the perturbative part i.e. the interaction of the two quarks, then we can assume that the quark anti-quark pair is indeed produced in the far past (a demand for calculations using Feynman rules) and the quarks can be seen as incoming free fermions. This means, that we can use one of the simples calculations in QED, the $e^+e^- \to \mu^+\mu^-$ as a foundation, that can be extended to $q\bar{q} \to l^+l^-$ by replacing the muon charge with the quark[1] and charge averaging over the colour orientation of the quarks and antiquarks. Generalising to all leptons from e^+e^- the expression becomes

$$\sigma(q_f\bar{q}_f \to l^+l^-) = \frac{1}{3}Q_f^2 \cdot \sigma_{ee\to\mu\mu} \tag{3.1}$$

where Q_f is the charge of the quark with flavour f. In this way, $\sigma_{e^+e^-\to Z/\gamma*\to\mu^+\mu^-}$ can be calculated based on the $|\mathcal{M}|^2$ method described further in [3]. For the special case of two incoming particles a and b and a two-particle final state the $\mathcal{M}$-matrix can be related to the cross section by the equation.

$$\left(\frac{d\sigma}{d\Omega}\right)_{CM} = \frac{1}{2E_a 2E_b|\nu_a - \nu_b|}\frac{|\mathbf{p_1}|}{(2\pi)^2 4E_{cm}}|\mathcal{M}(p_a, p_b \to p_1, p_2)|^2, \tag{3.2}$$

where $d\Omega$ is $\sin\theta d\theta d\phi$ with $\int d\Omega = 4\pi$, $|\nu_a - \nu_b|$ is the relative velocity of the beams (incoming particles) in the laboratory frame, the subscripts 1 and 2 the outgoing particles and E and

[1] as both are fermions they will behave identically when using the Feynman rules except for the difference in charge as will be seen.

p, their energy and momentum, with E_{CM} being the total initial energy. As mentioned this equation makes the assumption, that the incoming particles can be seen as coming from an infinite past, while the resulting particles are in the infinite future.

Calculations of the matrix element $|\mathcal{M}|^2$ have been included in the appendix A.1. The result is the following equation.

$$\frac{1}{4}\sum_{spins}|\mathcal{M}|^2 = \frac{8e^2}{(q^2-m_Z^2)^2}\left[(p\cdot k)(p'\cdot k') + (p\cdot k')(p'\cdot k) + m_\mu^2(p\cdot p')\right] \tag{3.3}$$

This is obviously still not a final cross section but let us look a bit at the physics of the collision. If the particles are assumed to scatter off each other, as is the case, the incoming and outgoing particles should be separated by an angle, θ. The momentum of the incoming particles is the projection of the total energy in the direction of the beam. In the centre of mass frame this means, that

$$\begin{aligned} q^2 &= (p+p')^2 = 4E^2 \\ p\cdot p' &= 2E^2 \\ p\cdot k &= p'\cdot k' = E^2 - E|\mathbf{k}|\cos\theta \\ p\cdot k' &= p'\cdot k = E^2 + E|\mathbf{k}|\cos\theta \end{aligned} \tag{3.4}$$

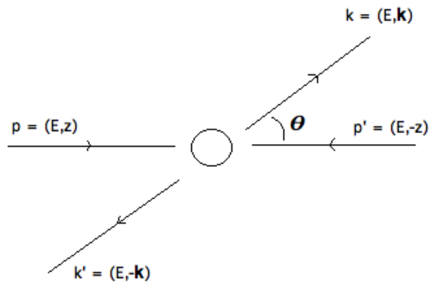

Figure 3.1: 4-momenta for the $e^+e^- \to \mu^+\mu^-$ collision in the centre-of-mass frame. The physical interpretation allows us to rewrite the matrix element resulting in an actual cross section.

which gives us the final equation

$$\begin{aligned} \frac{1}{4}\sum_{spins}|\mathcal{M}|^2 &= \frac{8e^2}{(4E^2-m_Z^2)^2}\left[E^2(E-|\mathbf{k}|\cos\theta)^2 + E^2(E+|\mathbf{k}|\cos\theta)^2 + 2m_\mu^2E^2\right] \\ &= \left(e^4 + \frac{16e^4E^4}{m_Z^4} - \frac{2e^4E^2}{m_Z^2}\right)\left[(1+\frac{m_\mu^2}{E^2}) + (1-\frac{m_\mu^2}{E^2})cos^2\theta\right] \end{aligned} \tag{3.5}$$

As we will be interested only in the high energy limit we can now safely assume, that $E_{CM} \gg m_\mu$. The terms in front are also interesting to look at. The first term e^4 corresponds to what one would get if the calculation was done only for the photon as the mediator. The second and third terms thus represent the contribution from the Z boson, that is small for centre-of-mass energies smaller then the Z mass but rises from there. This equation can now be inserted into Eq. 3.2. In the case discussed here, $|v_a - v_b| = 2$ and $E_a = E_b = E_{CM}/2$ so it will take the form

$$\begin{aligned} \frac{d\sigma}{d\Omega} &= \frac{1}{2E_{CM}^2}\frac{|\mathbf{k}|}{16\pi^2E_{CM}}\cdot(\text{Eq.3.5}) \\ &= \left(1+\frac{8E_{CM}^4}{m_Z^4} - \frac{2E_{CM}^2}{m_Z^2}\right)\cdot\frac{\alpha^2}{4E_{CM}^2}(1+cos^2\theta) \end{aligned} \tag{3.6}$$

Where we have used the common notation, $\alpha = e^2/4\pi$. Thus the leading order cross section in the high energy range is, after integrating over $d\Omega$, given by

$$\sigma_{ee\to\mu\mu} \xrightarrow[E>>m_\mu]{} \left(1+\frac{8E_{CM}^4}{m_Z^4} - \frac{2E_{CM}^2}{m_Z^2}\right)\cdot\frac{4\pi\alpha^2}{3E_{CM}^2} \tag{3.7}$$

This is indeed a very simplified result, and a final result, should take into account the important corrections to higher order of e.g. loop diagrams and virtual particles. In the analysis in this thesis, we calculate cross sections using Monte Carlo generators that includes higher order calculations or are optimised for the relevant processes. For an example of theoretical next to leading logarithm calculations and corrections see [15].

To get $\sigma_{q\bar{q}\to l^+l^-}$ we now simply multiply by the charge averaged over colour orientation of the quarks.

$$\sigma(q_f\bar{q}_f \to Z/\gamma* \to l^+l^-) \quad \xrightarrow[E>>m_\mu]{} \quad \frac{1}{3}Q_f^2 \cdot \left(1 + \frac{8E_{CM}^4}{m_Z^4} - \frac{2E_{CM}^2}{m_Z^2}\right) \cdot \frac{4\pi\alpha^2}{3E_{CM}^2} \tag{3.8}$$

3.1.1 Feynman diagrams for the three signal processes

To compare the cross section to experimental cross sections, we need to consider the fact, that the incoming partons are not from an infinite past, but stems from protons in a collider. Let us look at what diagrams actually contribute to the production of the three processes at tree level. The program MadGraph [16] calculates relevant tree level diagrams and corresponding cross sections based on the calculations described in Section 3.1. The Feynman diagrams have been plotted for each signal and can be seen in Fig. 3.2. The A denotes the photon, the curly lines gluons and u any flavour of quark (antiquark).

The cross sections we get from the various diagrams for two protons colliding with a centre-of-mass energy of 7 TeV have been listed in Tab. 3.1

process	σ [pb]	error [pb]
$d\bar{d} \to Z \to \tau\tau$	104.470	0.765
$\bar{d}d \to Z \to \tau\tau$	103.710	1.051
$u\bar{u} \to Z \to \tau\tau$	85.266	0.754
$\bar{u}u \to Z \to \tau\tau$	84.179	0.746
$d\bar{d} \to \gamma* \to \tau\tau$	13.520	0.246
$\bar{d}d \to \gamma* \to \tau\tau$	13.493	0.191
$u\bar{u} \to \gamma* \to \tau\tau$	52.574	0.361
$\bar{u}u \to \gamma* \to \tau\tau$	52.109	0.407
$d\bar{d} \to WW$	5.939	0.043
$\bar{d}d \to WW$	5.871	0.057
$u\bar{u} \to WW$	8.561	0.0.054
$\bar{u}u \to WW$	8.482	0.057
$gg \to t\bar{t}$	66.526	0.251
$d\bar{d} \to t\bar{t}$	4.558	0.054
$\bar{d}d \to t\bar{t}$	4.553	0.0.058
$u\bar{u} \to t\bar{t}$	7.050	0.055
$\bar{u}u \to t\bar{t}$	7.081	0.054

Table 3.1: The theoretical cross sections calculated by the MadGraph package.

The $Z/\gamma* \to \tau\tau$ cross section is the largest, with a total of 509 pb [2] followed by $t\bar{t}$ with

[2] Actually the $Z/\gamma*$ process is gauge dependant and can only be split up using factorisation. The result for the two processes calculated separately in this way is however identical to the correct calculation of $Z/\gamma*$ in practice.

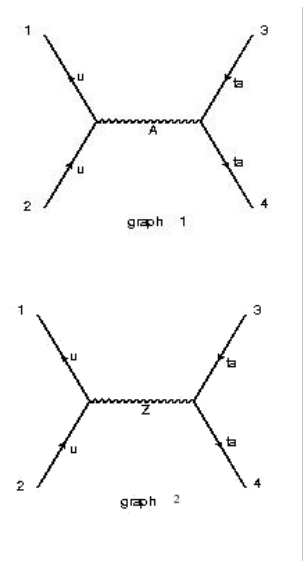

(a) The only tree level Feynman diagram relevant for the production of $Z \to \tau\tau$. u here represents any quark/antiquark.

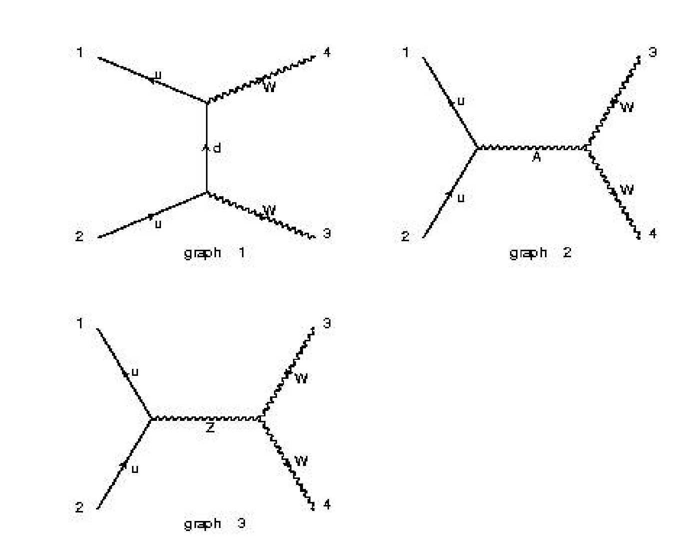

(b) The tree level Feynman diagrams relevant for the production of WW. u again represents any quark/antiquark.

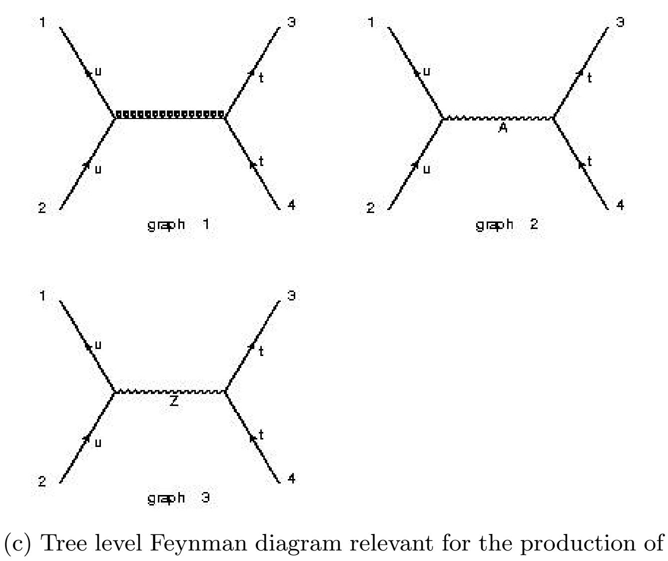

(c) Tree level Feynman diagram relevant for the production of $t\bar{t}$ through a quark and an antiquark.

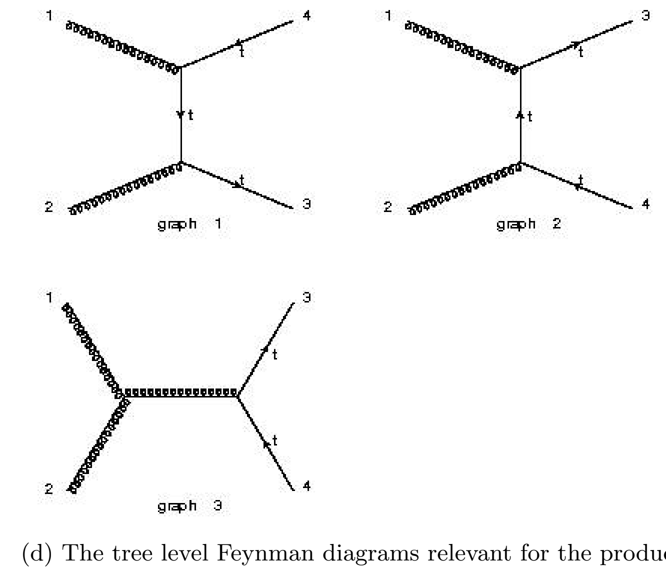

(d) The tree level Feynman diagrams relevant for the production of $t\bar{t}$ through gluons.

Figure 3.2: Tree level Feynman diagrams for the three signal processes generated using MadGraph.

90 pb. The WW production cross section is the smallest with a total of 29 pb. The relevance for our $e\mu$ final states changes slightly with the branching ratios to an electron and a muon for the three processes and corrections should definitely be made for higher order loops. Z and WW can in fact be made from gluons through diagrams containing quark loop and the cross section from this will give a 5% correction. [17] When calculating these cross sections Madgraph relied on a weighting of the initial partons.

3.2 Parton distribution functions

At the Large Hadron Collider, LHC located between Switzerland and France, which will be described in more detail in Section 3.11, protons are collided at a centre of mass energy of 7 TeV. When protons are collided at high energies a very large part of the collisions are soft e.g. elastic or diffractive scatterings between the protons. More relevant for this study is however the hard (inelastic) scatterings where partons from the incoming hadrons hit each other transferring large amounts of energy and creating new particles. If the behaviour of the incoming partons was fully understood theoretically comparing expectations with data from experiments would be a matter of understanding the accelerator and detector alone. But the behaviour of theses partons are not fully understood and we cannot rely simply on our theories to understand the actual cross sections of processes. Which type of partons that dominate the collisions varies significantly with incoming hadrons and centre-of-mass energy. A proton-anti-proton collider like the Tevatron[3] will have a higher chance of colliding quarks and antiquarks than a proton-proton collider of the same energy, as the antiproton consists primarily of antiquarks. The centre of mass energy turns out to be another important factor and whereas valence quarks - the (anti) up and (anti) down quarks constituting (anti) protons, dominate heavy particle production in the Tevatron gluons and *sea* quarks play a much larger role in LHC. Due to the much higher energy of the protons at LHC valence quarks are relativistic and will radiate gluons that are reabsorbed continuously. These gluons can split into virtual quark-antiquark *sea quark* pairs and will be produced and split up at rates that make the gluons and sea quarks the most likely objects to collide when the two proton beams interact. Figure 3.3 show a collision of two partons depicted. The functions f(x) describe the probability to find the i'th parton with a certain amount of the total hadron momentum. The energy fraction is denoted x and is given by

$$x_i = \frac{P_{\text{i'th parton}}}{P_{\text{hadron}}}, \tag{3.9}$$

so that the effective energy of the collision is given by $x_i \cdot x_j \cdot \sqrt{s}$ for two partons i and j colliding with centre of mass energy, $\sqrt{s}$. The probability for different partons to have a given fraction of energy differs and not all partons are equally likely to partake in a certain process. In other words the cross section, $\sigma_{i,j \to X}$ is dependant on the initial partons i and j. This was already postulated when previously calculating the signal cross sections, but it can illustrated more thoroughly now.

[3]The Tevatron is a proton-antiproton collider situated in the United States, at the Fermi National Accelerator Laboratory in Batavia, Illinois. It is second highest in collision energy after the Large Hadron Collider (LHC). The Tevatron accelerates protons and antiprotons in a 6.28 km (3.90 miles) ring to energies of up to 1 TeV, hence the name [18]

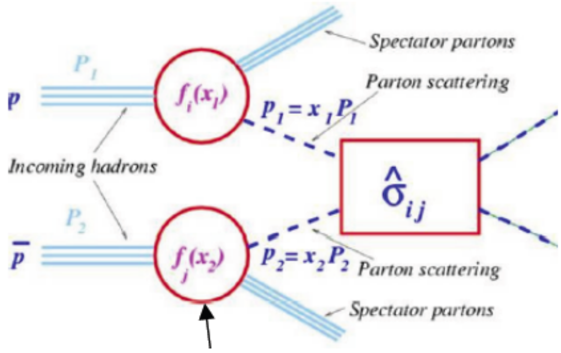

Figure 3.3: The *P*arton *D*istribution *F*unctions, $f(x)$ are a description of the proton constituents behaviour governing the collision outcomes. The functions $f(x)$ describe the probability of a given parton to carry a momentum fraction, x, of the proton momentum. The cross section for a given interaction, $\hat{\sigma}$, is dependant on these function.

The fraction of energy carried by partons must obviously [19] sum to 1

$$\int_0^1 x[f_u(x) + f_d(x) + f_{\bar{u}}(x) + f_{\bar{d}}(x) + f_g(x)]dx = 1 \tag{3.10}$$

For a proton-proton collider constraints can be imposed on $f(x)$, as it should contain an excess of quarks in the proton bound state uud. The probability for a given parton with momentum fraction, x is thus for a proton - proton collider shown in Fig. 3.4. To fully understand the kinematics involved we introduce the variable *rapidity*, y, given by

$$\begin{aligned} E &= m_T \cdot \cosh y \\ m_T^2 &= m^2 + P_T^2 \end{aligned} \tag{3.11}$$

The cross section of a given process relies on the rapidity of the initial particle. As the rapidity depends on the mass of the particle, the final cross section will also depend on the mass of the particle. In the small y region the cross section will be constant due to what is referred to, as the rapidity plateau. The width of the plateau becomes wider with increasing centre-of-mass energy but decreases with particle mass. This can be seen in Fig. 3.5b where the rapidity has been plotted for top quarks and hadrons from up quarks using Madgraph. The momentum transfer will depend on the rapidity which means the momentum of the initial partons will depends on their rapidity. This is all summed up in Fig. 3.5a. To generate particles with high mass, for a centre-of-mass energy of 14 TeV as in the plot, high momentum transfer is needed. A momentum transfer of the order 100 GeV will happen at the rapidity plateau with y small for x around 10^-3. As the creation of W's and Z's will be most probable for momentum transfer with energies around their mass, they will be dominated by the partons with x close to this value. From Fig. 3.4 we can see these are both sea and valence quarks and gluons. The peaks at x close to zero in u and d are from the valence quarks, but these are no longer dominant for the values of x we consider.

Returning to our discussion of the cross section for our signal processes we can now

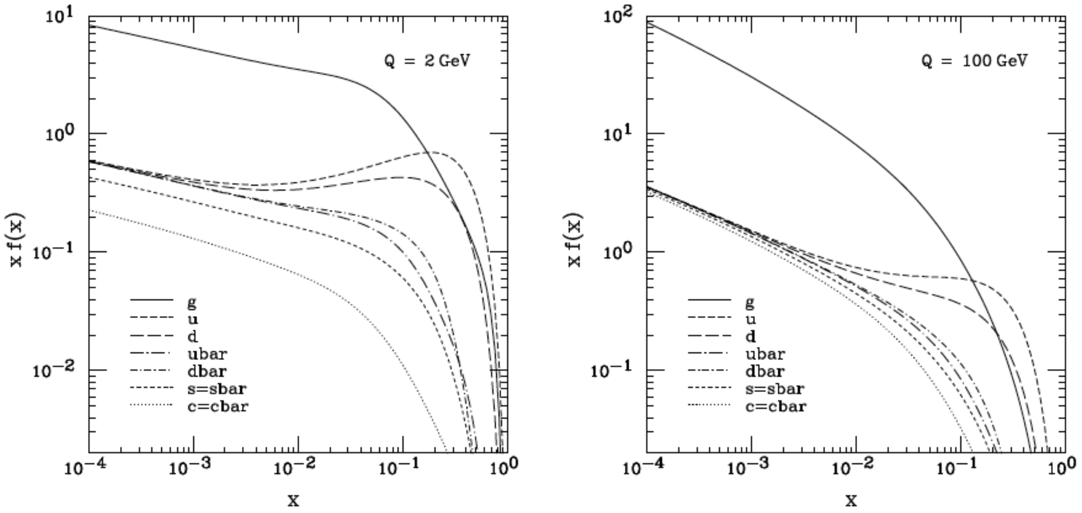

Figure 3.4: The CTEQ6M [20] parton distribution function $xf_f(x)$ for quarks, antiquarks and gluons in the proton for an invariant momentum transfer $Q = 2$ GeV and $Q = 100$ GeV. It is seen, that the picture changes for the proton constituents with energy transferred, or conversely with scale probed in the proton.

complete Eq. 3.8

$$\sigma(p(P_i)p(P_j) \to Z/\gamma* \to l^+l^-) = \int_0^1 dx_i \int_0^1 dx_j \sum_f f_f(x_i)f_{\bar{f}}(x_j) \cdot \frac{1}{3}Q_f^2 \cdot \frac{4\pi\alpha^2}{3E_{CM}^2} \tag{3.12}$$

To get an actual number for the cross section the parton distribution functions, PDFs, still have to be determined though, and this cannot be done analytically as it is not a perturbative theory (soft, long distance physics and not asymptotically free). Instead it must be extracted at a given momentum transfer (Q^2) and extrapolated from there. The data stems mostly from deep inelastic scattering experiments, but experiments of Drell-Yan and High E_T jets along with experiments at the CDF detector at the Tevatron has helped to estimate PDFs at different energy scales. CTEQ [20] and MRST [21] are two of the major groups working on the determination and renormalisation of PDFs from experiments. If precise cross section measurements are performed at higher energies they can be tested against expectations from *Monte Carlo* simulated collisions with various PDFs. In this way the various PDFs can be more precisely constrained by the data hopefully resulting in a better understanding of the physics that governs them. One could perhaps imagine that the uncertainties from the PDF should be small enough, that they will not influence a cross section measurement significantly.

To investigate wether they are, let us look to Fig. 3.6. The right figure shows the cross section for various processes predicted with design energy of the LHC while the left figure shows the energy dependence of the cross sections. An interesting process to probe for the discovery of the Higgs would be its production through $t\bar{t}$ fusion - the fusion of a top and an antitop into a Higgs. Looking at the Fig. 3.6 the cross section for this process is the one denoted $gg \to qqH_{SM}$ which lies around 10^{-3} nb depending on the mass of the Higgs. The Higgs can decay through a variety of channels but one of interest could be the $\tau^+\tau^-$ channel

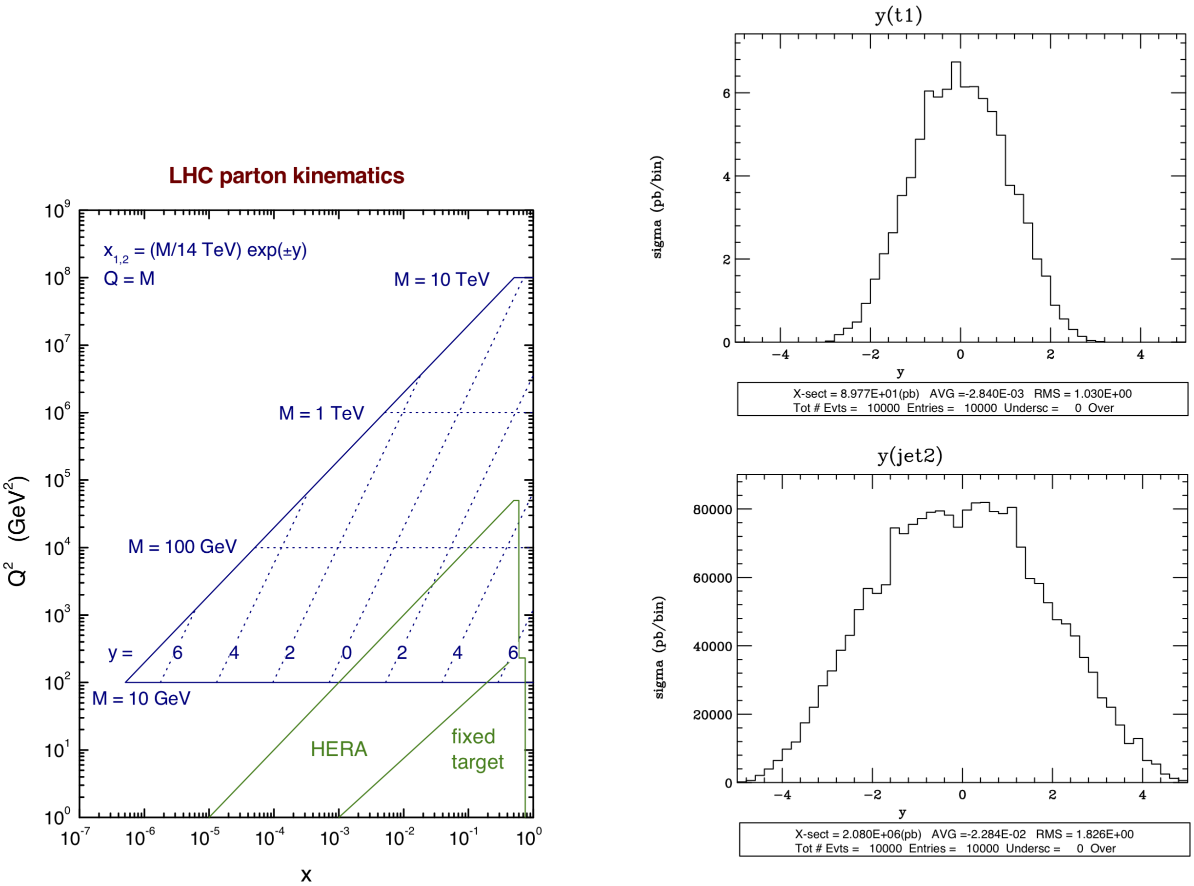

(a) The kinematic distribution of partons with the blue scratched region representing the LHC at design energy. The mass scale i.e. the energy in initial partons to create new particles depend on their rapidity and momentum transfer.

(b) Rapidity distributions of the top quark and jets from up quarks with much lower mass, show the difference the mass of the considered particles has for a given collision energy. The plots have been generated with Madgraph for a centre-of-mass energy of 7 TeV.

Figure 3.5: Kinematics governing the partons

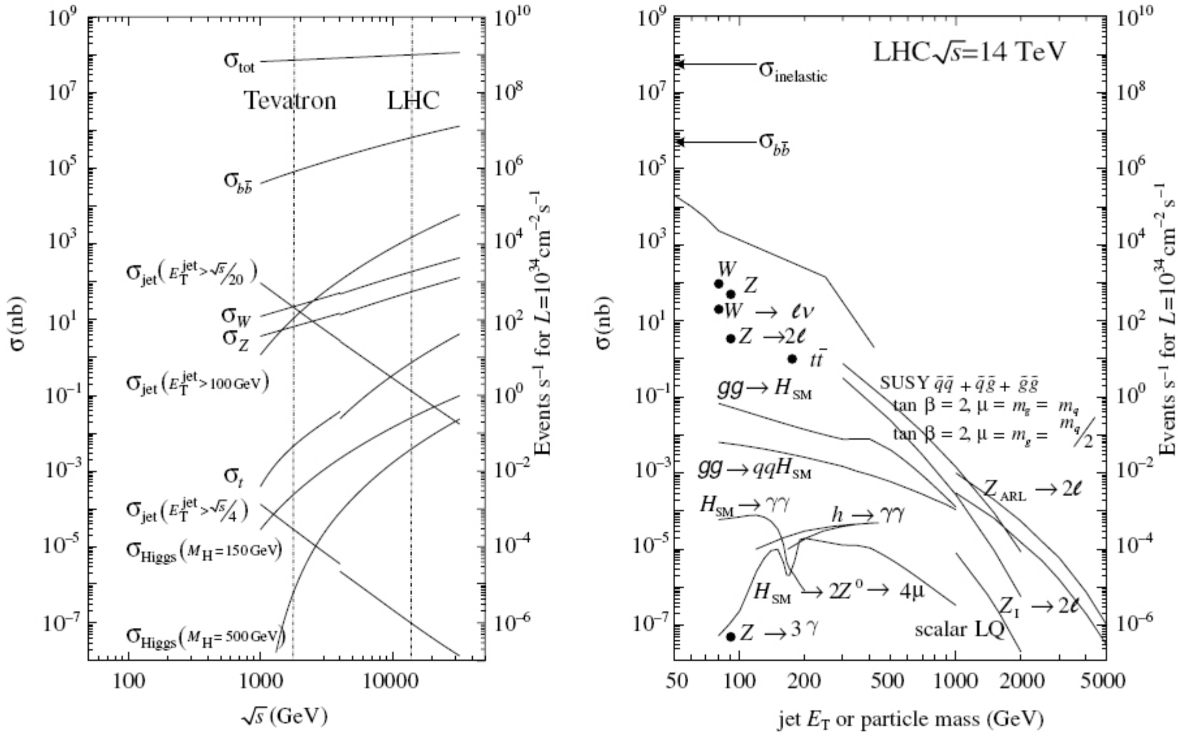

Figure 3.6: The plot on the right shows the different cross sections for processes at the design energy and luminosity of the LHC, while the left plot shows the cross section dependence on energy.

with either semi-leptonic or fully leptonic decay of tau leptons. Now to get a trustworthy signal for this process the backgrounds to such a final state would have to be known well enough, that their uncertainties are smaller than the total signal value. Major background to both the semi-leptonic and fully leptonic final state are exactly the WW,$Z \to \tau\tau$ and $t\bar{t}$ processes studied in this thesis. As can be seen in the figure, these processes are 4 or more orders of magnitude larger than the Higgs vector boson fusion cross section. A 10% uncertainty on the background processes would thus be a huge challenge for a precise measurement of the Higgs cross section. A percentage uncertainty up to 10% on cross sections is actually widely used at the time of writing, just from the pdf.

As we will see in the next sections, including PDFs in the calculations of cross sections for processes at pp colliders is not the only reason why Monte Carlo generators are a crucial tool for comparing theory to data. As these generators have been used extensively in this thesis, we have dedicated the next chapter to a more in-depth description of them.

3.3 The Monte Carlo generation method

Monte Carlo methods rely on computer algorithms that use repeated random sampling to compute particle interaction probabilities in particle physics. In particle physics experiments, Monte Carlo *generators* take up the difficult task of simulating realistic events of entire collisions. The simulations of events can be split up into four different parts. They have been illustrated pictorially for a hadron collision in Fig. 3.7 and are described below.

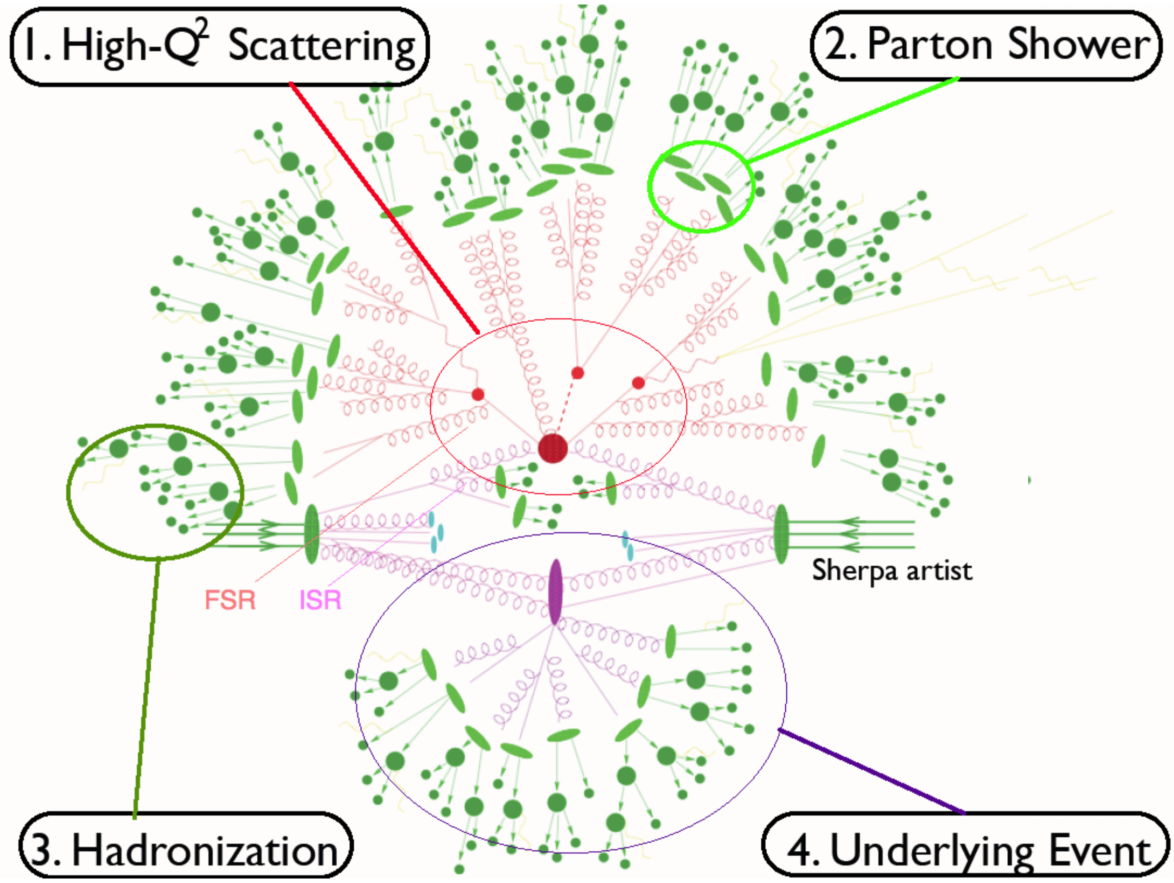

Figure 3.7: The simulation of a hadron collision is factorized into different parts. This is a necessity as the different parts cannot all be calculated analytically. The figure illustrates the complexity of event simulation.

- **High Q^2 scattering - The hard process** is the first step in the simulation of a particle collision event for the Monte Carlo generators. The initial particles of the process have momentum transfer, Q^2 between them, determined from the pdf. For collisions involving high Q^2 all processes will happen within short distances, and the calculations can be done perturbatively. The calculation of the hard process is done at matrix element level, like Eq. 3.12 where the PDFs are determined from experiments. The cross section calculation can take on different forms. If the calculations are simply done with tree level diagrams it is called leading order, LO. Corrections can be made to these calculations but if loop diagrams and virtual particles are taken into account, the calculations are next to leading order, NLO. No programs can as of now calculate 2 - 2 processes to more than NLO.

The hard process is where all interesting physics happen in the sense that it is here that e.g. the Z, WW and top quarks, considered in this thesis, stem from. The hard process is at generator level split into two subcategories: Decays of resonances and final state showers. Decay resonances are the decays of e.g. pions from taus and is correlated to the hard process. Final state showers are a combination of initial state radiation, ISR and final state radiation, FSR. ISR is gluons and quarks that stem from the quarks in the initial composition before the collision. FSR is gluons and quarks emitted after the collision. Particles from ISR will have momentum transfer of the order or even higher than the mass of the particle (e.g. Z or W) created in the collision, whereas FSR will have a momentum transfer lower than the mass of this. This means, that ISR will generally be responsible for the largest part of high P_T radiation in events. Furthermore multiple interactions can exist between beam remnants and particles from the hard process and initial- and final- state radiation. The initial-state composition and substructure and initial-state showers are governed by the parton distribution functions and the probability for gluons or quarks to be emitted before the collision.

- **Matrix Elements, ME, vs. Parton Showers** After the initial hard process the final state showers need to be evolved. The quarks and gluons start with momentum of the order of the transferred momentum, Q^2 but will radiate off gluons until all final state showers are at an energy scale of 1 GeV, where hadrons form.

  There is however a difference between different generator types. A purely Parton Shower based method will only have 2 - 2 or 2 - 1 processes in the hard process. These will be generated with matrix elements, as shown for Drell-Yan in the theory section, but all further showering will be calculated based on an approximation, that gluon radiation will be soft (low energy) and/or collinear. This approximation is used until a given cut-off scale possibly resulting in several separate showers in the same event. This can be seen in Fig. 3.8 which shows the Feynman diagrams corresponding to matrix elements at LO, NLO and NNLO (Next-to-next-to-leading-order) and the following parton showering.

  The first row represents the calculation of the matrix element to leading order and with all radiation coming from parton showering illustrated by the diagrams going towards the right. Alternatively the matrix elements, ME, can also be calculated to NLO and then both LO and NLO diagrams can be evolved via the Parton Showers. This is illustrated by the following rows. There are obviously overlaps between the diagrams with gluons from the initial matrix elements and the gluons from parton showering. The difference between the two, will lie in the momentum or the angle of the emitted gluon. For the matrix elements, the gluon will have energy of the order of the transferred momentum. The radiation from parton showering will have to be either collinear or soft, so for all transverse showers, gluons will be soft. The difference between the calculations is however small. The probability and selection of the diagrams will be decided by a matching algorithm of which several exist. Calculations to NLO has the strong advantage that matching has only to be done between the NLO matrix element diagram and corresponding one parton, Parton Shower diagram. Calculation of NLO diagrams has only been performed for a select few processes.

  After the evolvement of the gluons and quarks into cascades, the final state showers, the energy of the gluons are of the order 1 GeV. At this point, the perturbative theory breaks down as the strong coupling constant becomes large. The particles can no longer be seen as asymptotically free and theoretical calculations are no longer possible. At this point the showers will *hadronise*

- **Hadronisation and final decays** The colour confinement of the quarks means that no free quarks can exist after an interaction. The quarks and gluons emerging from a collision therefore have to be merged into colour neutral objects by the algorithm performing the hadronisation. Hadronisation is performed differently for the different generators but can be split into three different types [22]: Independent fragmentation, string fragmentation, and cluster hadronisation.

  Independent fragmentation does not take into account the colour connections and has not been used for any of the generators we use.

  String fragmentation give better agreement with data so far but also contain a lot of parameters to describe the flavour composition that can be tuned.

  Cluster hadronisation is the main alternative to string fragmentation. It has fewer parameters but also has more difficulties in simulating data correctly.

  Unstable particles like heavy hadrons or taus will have to be decayed after hadronisation. The decays are governed by the branching ratios and can be calculated theoretically, making it a relatively well understood part of the event generation process.

- **The underlying event** The underlying event consists of the partons originating from the protons colliding. They must of course also become colour neutral. The distances are however large enough, that there is generally no colour exchange between these beam remnants and the hard process. The underlying event however depends on the hard process and the evolution is done by Partons Showering and hadronisation.

  It may happen in real colliders, that more than one pair of protons collide in an event. This is referred to as pile-up and multiple interactions. Multiple interactions are far enough away from each other in terms of time scales involved, that pile-up is simply simulated by adding events on top of each other.

3.4 The generators

The combination of these four parts into a Monte Carlo generator is done in many different ways. Often different programs will be used to perform the specific parts of the tasks and then combined with others. For the same reason an accord has been specified for event records. It dictates how particles created in a hard process must be stored numerically, so they can be read by other programs, that do the parton showering, hadronisation and decays. The accord is named the *Les Houches Accord*. There exist programs, that can calculate all four parts themselves, e.g. that can be used as standalone Monte Carlo generators. These constitute the backbone for generating events, but will often be interfaced to other programs to perform one or more of the four parts of the calculation. The two most widely used of these today are Pythia [24] and HERWIG [25], as these generate full unweighted events that can be used directly in physics analysis or interfaced to detector simulation.

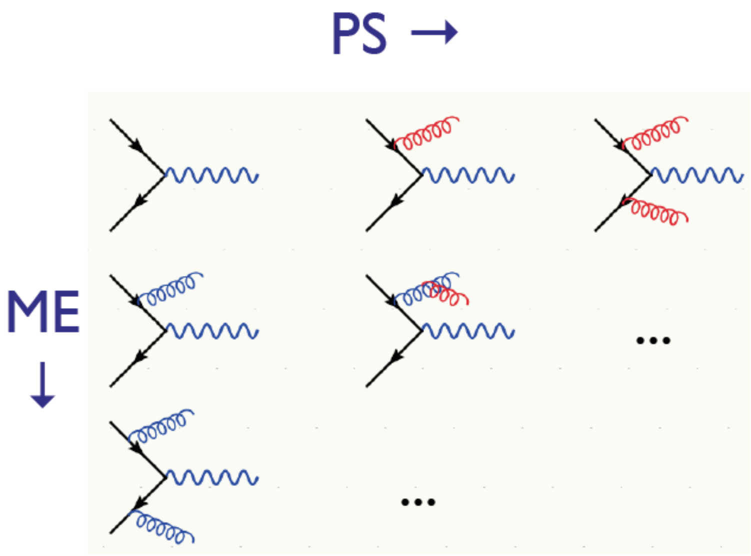

Figure 3.8: The evolution of final state showers can be done in various ways. The interaction can be calculated with matrix elements and parton showering can then be used to produce all additional radiation. Similarely the matrix elements can be calculated up to NLO after which the diagrams can be evolved with parton showering. In both cases there will be overlap between the diagrams as seen in the diagonal. The matching and selection of which diagrams to use, is performed by matching algorithms.

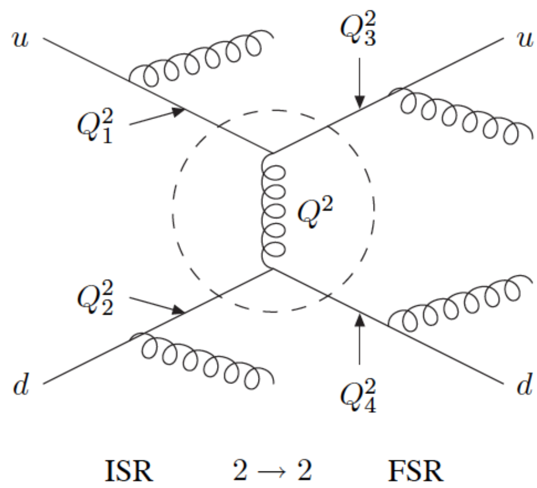

Figure 3.9: The calculation of $2 \rightarrow n$ processes would not be possible in generators for n much higher 2 if not for the method of factorising the event. In this way different parts of the process can be calculated independently and merged afterwards, to a complete numerical calculation. The figure shows the factorisation of a $2 \rightarrow 2$ process with both ISR and FSR. From [23]

3.4.1 PYTHIA

Pythia [24] is one of the most widely used generators, as it is a standalone generator for everything from few-body hard processes to complex multihadronic final states through parton showering and hadronisation. All main aspects of the events are simulated, such as hard-process selection, initial- and final-state radiation, beam remnants, fragmentation, decays, etc. It uses the CTEQ 5L [20] parton distribution function but can be linked with others.

Pythia has the limitation, that it only does $2 \rightarrow 2$ or $2 \rightarrow 1$ interactions of the hard process, which means that all further particles will have to be created by parton showering. $2 \rightarrow n$ final states can however be created this way. The method is called factorisation and is shown in Fig. 3.9. If other programs are used for the calculations of matrix elements, a matching will have to be done between diagrams arising from those, and the Pythia parton showering.

The hadronisation is done, after all partonic activity i.e. initial- and final- state radiation and parton showering, by string fragmentation, followed by the decays of unstable particles. The method used, is the Lund string model that relies on a description of the QCD field lines as compressed tubelike regions for large charge separation. These field lines are represented as gluon strings that, when stretched long enough, break up into quark-antiquark pairs, which form up with the existing quarks forming colour neutral mesons. This part is almost completely non-perturbative, and so requires extensive modelling and tuning or, especially for decays, parametrisation of existing data.

3.4.2 HERWIG

The other standalone generator Herwig [25] works in many ways like Pythia. There is however a wider range of programs that can be interfaced to Herwig for calculating e.g. matrix elements for $2 \rightarrow n$ processes, with n greater than 2. Calculation with Herwig alone will like in Pythia, only be to lowest nontrivial order without e.g. loop corrections. Herwig has emphasis on the detailed simulation of QCD showers. It also uses the Parton Shower approach for initial- and final-state QCD radiation and is based on the angular ordering like the collinear approximation used in Pythia. For hadronisation Herwig does cluster hadronisation. Colourless clusters are formed from colour connected quarks. They consist of quark-antiquark (meson-like clusters), quark-diquark (baryon-like), or antiquark-antidiquark (antibaryon-like) pairs. The basic idea of the model is that the clusters decay according to the phase space available to the decay products. In other words, the initial partons are merged into colourless clusters, that are then decayed to hadrons.

3.4.3 Generators for the hard process

The advantages of interfacing another program with Pythia or Herwig to calculate the hard process are obvious. Programs optimised for a specific process, either with speed or precision in mind, can then be used for calculating the matrix element. As the event is stored in the Les Houches accord format, the task of interfacing is made much simpler. The calculation of the hard process is still done with different approaches each having their own advantages.

NLO calculations, where both first order real and virtual corrections have been included, are much better than simple LO calculations. The program MC@NLO does Parton Showers with next-to-leading-order QCD matrix elements [26] It is a Fortran package that allows linkage between HERWIG and next to leading order calculations of rates for QCD processes.

Although matching between matrix elements and Parton Shower diagrams still has to be done, only NLO and not LO diagrams have to be evolved with parton showering, so fewer diagrams have to be matched. Not all processes are however known to NLO. Despite this MC@NLO includes a range of production mechanisms spanning Higgs boson, single vector boson, vector boson pair, heavy quark pair, single top (with and without associated W or charged Higgs), lepton pair and associated Higgs+W/Z production in hadron collisions. This generator is used in this thesis to simulate events where proton collisions produce lepton pairs through top pair production and subsequent decay. It only supports calculation of W and Z with additional partons (jets) up to two partons.

Instead calculation of Z and WW plus partons, also relevant for the work presented in this thesis, have been done with ALPGEN [27]. ALPGEN is specialised in multi parton processes. It is based on calculations using tree-level matrix elements, but has been developed especially with multi-jet events in mind. It calculates matrix elements to LO, with a fixed number of additional partons in a process. This is a better approach for events with high jet multiplicities with large P_T than the Parton Shower method, where additional partons (with respect to the initial $2 \rightarrow 2$ process) are generated only during the shower evaluation. The Parton Showers and hadronisation and the following matching will be done by e.g. HERWIG. The differences between MC@NLO and ALPGEN have been shown to be small in [28]. Figure 3.10 from [28] shows the difference in number of jets for the two programs. For the description of four or more jets, where the distributions differ, ALPGEN will have the best description, as it is optimised for exactly this, whereas MC@NLO will rely on the parton showering to get probabilities for five-jet events.

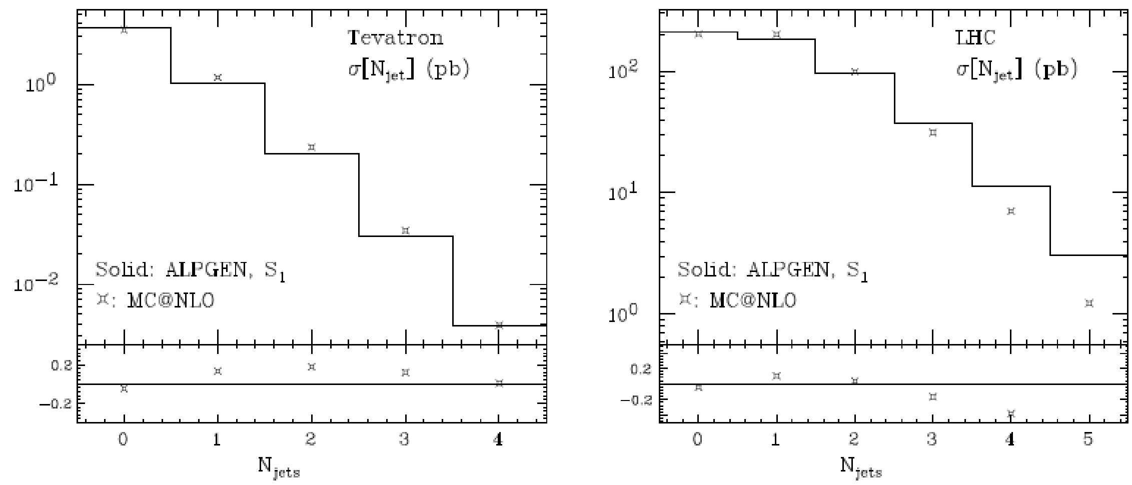

Figure 3.10: The figure shows the number of jets from $t\bar{t}$ events generated with MC@NLO and ALPGEN respectively. The events have all been generated as stable $t\bar{t}$ events with non perturbative calculations i.e. the first two steps in the calculation process has been performed but no hadronisation or calculation for underlying event. As seen the distributions agree well up until 4 or more jets, where they start to differ.

For some background processes optimisation of speed is central as the task of generating these background processes would otherwise be too time-demanding. The program AcerMC

[29] is a program developed specifically for the task of calculating background processes for the LHC experiment. It is a specialised program used mainly for the calculation of the matrix elements for top and bottom quark processes. Even though calculations are not made to NLO the events generated are very reliable. All of the above can be interfaced with Herwig, and works is in progress to allow for interfacing with Pythia for those that do not yet allow this.

Multiple interactions

For the simulation of multiple interactions Herwig can be interfaced with a program called JIMMY [30]. JIMMY focuses on the impact of multiple interactions (from e.g. beam remnants) on the event. This is relevant with a collider like the LHC where particle multiplicities are high for various reasons. PYTHIA has multiple interactions included as default, with various models to choose from.

3.4.4 Detector simulation

Before an event generated by the Monte Carlo generators can be compared to experimental data, a simulation of the detector-system must be performed. In ATLAS this can be done with two official programs, ATLFAST II [31] and Geant4 [32]. ATLFAST II combines full simulation of some parts of the detector with faster simulations and retains the storage format and naming convention of real reconstructed data. It is much faster and retains a high degree of detail compared to full simulations of the detector. If the full detail is however desired GEANT4 can be used. Geant4 is a program for simulating particle movement through all kinds of material and is used in ATLAS to simulate the entire detector. It contains information on the weight of each screw and bolt in the detector down to a precision in grams. For a detector of over 1000 tons, this is astonishing. The datasets used in this thesis have been generated with the generators described above and have all gone through **full** detector simulation.

Part II

Experiment

3.5 The Large Hadron Collider

The Large Hadron Collider, LHC is the largest particle accelerator in the world. It is located at the border of Switzerland and France. It has been built by the international research organisation CERN (Conseil Européenne pour la Recherche Nucléaire - The European Organisation for Nuclear Research) which include more than 40 countries and has more than 6500 employees.

The LHC has been built to accelerate protons to a centre-of-mass energy of 14 TeV and from summer 2010 till November 2010 LHC has operated with mean energies of 3.5 TeV per proton resulting in a centre-of-mass energy of 7 TeV. This is the highest energy ever recorded for a man made proton collider. LHC is built underground with depths ranging from 50 to 175 metres and the circumference of the tunnel is 27 kilometres.

It is designed to accelerate both protons and lead ions depending on the physics of interest. For this study proton collisions are considered. In the accelerator two beams of protons are accelerated inside beam pipes in the tunnel in opposite directions. The protons in the beams are held in position, focused and squeezed tighter together by appropriate magnets along the beam pipes. Particles are initially accelerated by various smaller accelerators before entering LHC and from that point on, superconducting dipole magnets designed for a magnetic field of up to 8.3 Teslas (T) are used to hold them in place. Electric fields will accelerate the protons up to a speed only 3 metres per second slower than the speed of light, $0.999999991c$.

At four points on the LHC ring, the beam pipes cross to allow for collision of protons from the oppositely moving beams. At these points the four major experiments at the LHC are situated; ALICE, ATLAS, CMS and LHC-b. This study focuses on the ATLAS experiment where data taking has been going on for more than half a year at the time of writing.

The rate of produced events at ATLAS is given by $N = L\sigma$, where σ is the cross section and L is the luminosity given in $cm^{-2}s^{-1}$. The luminosity is a measure of the number of collisions per unit of area and time. For data recorded over a period the number of events is given by the time integrate of the luminosity, the integrated luminosity, denoted $\mathcal{L}$.

The total integrated luminosity collected by the ATLAS experiments is now above 45 pb^{-1} but far from all of this data has yet been satisfactorily understood. The data has been recorded from a series of runs where the settings for triggers, which will be elaborated shortly, have been different. The amount of recorded data can be seen in Fig. 3.12 . The first period of data up to a few pb^{-1} has already been understood to a level where physics can be interpreted, and publications done while the bulk of the data collected is being analysed.

3.5.1 A collider designed to look for new physics

As mentioned in the theory section all particles in the Standard Model have been observed with the exception of the Higgs particle. As the Higgs field is the most commonly agreed upon mechanism for generating mass in the Standard Model, it is a necessity to test it. The LHC is at the moment running with a centre-of-mass energy of 7 TeV but is designed to go even higher, peaking at 14 TeV after a planned upgrade in 2012. This allows physicist to probe physics at the limit of TeV regime where a Standard Model description of the world of particles without the Higgs would break down [33]. This in reality means, that the experiment should find the Higgs particle if it is there.

If the Higgs is found, further probing will have to be done to determine if this is indeed a Standard Model Higgs. There are in fact theories, that predict more than one Higgs with some of them being identical to the Standard Model Higgs. These theories are called Super-Symmetric, SUSY, Standard Model theories. They include the framework of the Standard Model but have additional particles - more precisely a supersymmetric partner for each Standard Model particle, and typically 5-7 different Higgs particles depending on the exact type of symmetry theory. These theories could help explain some of the other big questions like what dark matter in the universe is.

On the other hand if the Higgs particle is not there, this energy limit should also be the limit, in which the experiment is able to observe alternative mechanism for giving mass to particles. [34] [35] The proposed form of these are many including theories like Technicolor and top-quark condensates. One of these takes root in the introduction of more spatial dimensions. In reality these dimensions would only be seen at very small distances or very large energy densities like we get at LHC. This opens for the possibility of particles like the *Graviton* to explain the mass of particles and could explain the large difference between the forces in the Standard Model and gravity at small distances. The theory also allows for more exotic particles like mini black holes or the Kaluza-Klein towers, that predict particles with masses even in the TeV's.

To find out which Higgs particle is indeed observed, if it is found, detailed measurements of Standard Model processes at this energy are needed. To determine wether an exotic signal is indeed a signal or simply a misinterpreted background, this understanding makes the difference. To get there, the measurement of cross sections for Standard Model processes are essential.

The energies of the LHC are groundbreaking and the physics that scientist expect could be so as well, but for anything to be seen it has to be detected by one of the four experiments ATLAS, ALICE, CMS and LHCb. Our studies are dedicated to data from the ATLAS detector.

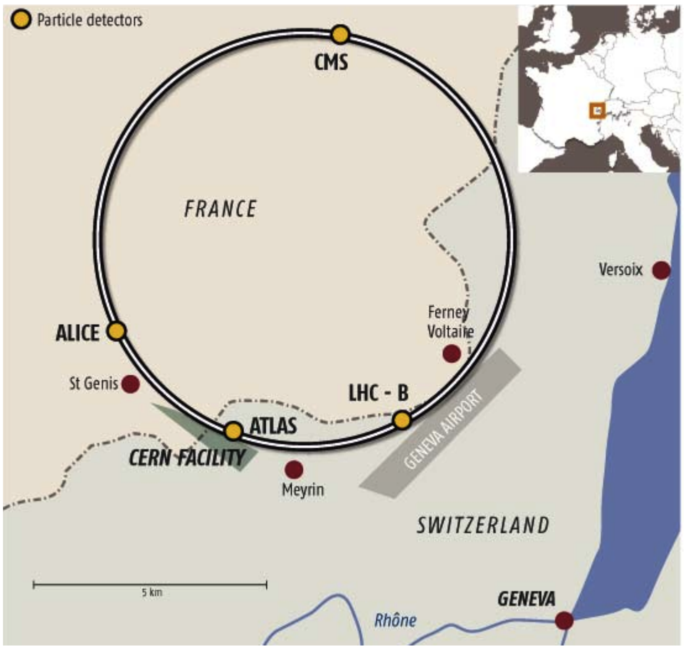

Figure 3.11: The LHC is buried many meters underground to screen the experiments from cosmic radiation and other possible external disturbances. The idea for the ATLAS detector stems from the 1980's and to run and analyse the data collected by ATLAS 3800 scientist are participating from 38 countries.

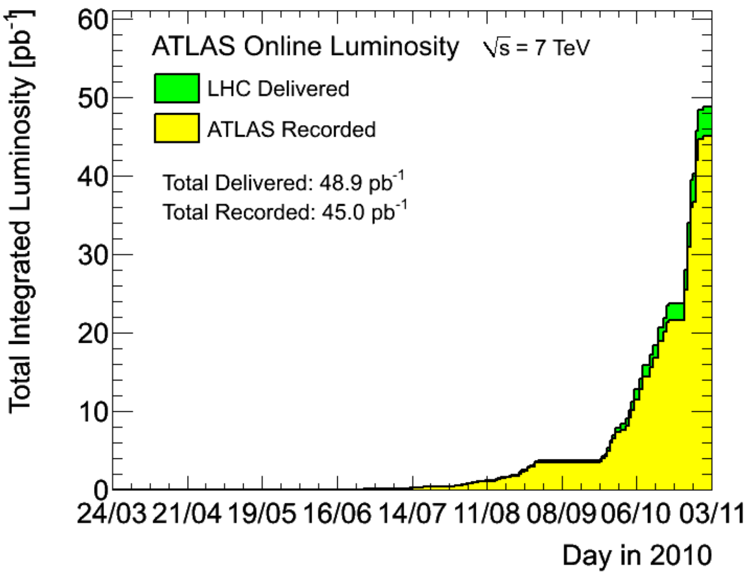

Figure 3.12: Total Integrated Luminosity for the LHC and the amount recorded by the ATLAS experiment during the periods of running in 2010.

3.6 The ATLAS detector

The ATLAS [36] (A Toroidal LHC Apparatus) is a multipurpose detector designed to cover a wide range of physics including tests of the Standard Model and physics beyond the Standard Model. It consists of several parts, referred to as sub-detectors, each designed and optimised for special tasks. If the ATLAS detector was to be compared with a normal digital camera, the resolution would be of the order of 100 mega pixels which in itself is not so spectacular. But ATLAS takes pictures in three dimensions with this resolution. This section is dedicated to the description of the sub-detectors in ATLAS with emphasis on the parts most relevant for this study.

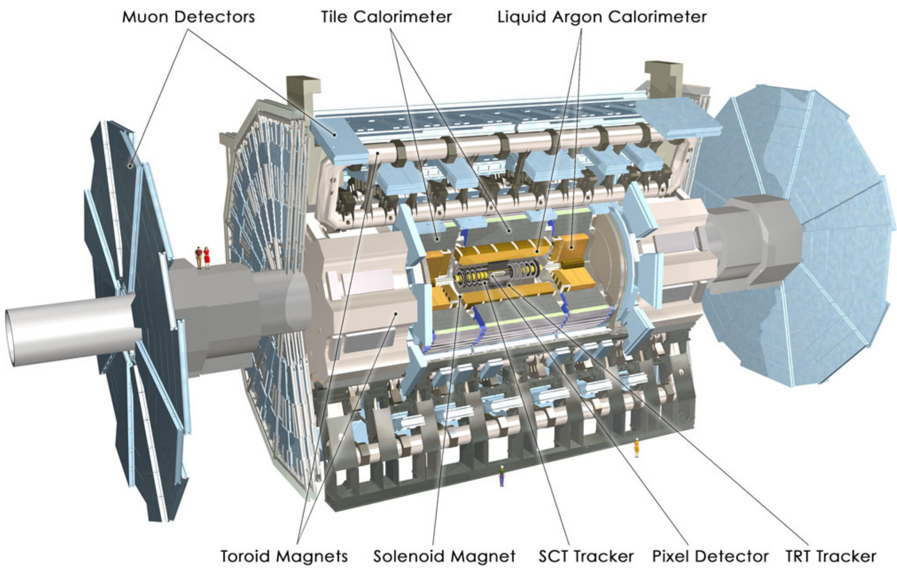

Figure 3.13: The ATLAS detector with name tags on the different sub detectors. To give an idea of the actual size of the detector note the people at the bottom and left of the detector.

3.6.1 Inner Detector

The inner detector consist of three different detectors. The pixel detector, the semiconductor tracker (SCT) and the transition radiation tracker (TRT). All three are arranged into central barrel parts and two end-cap parts composing the forward detector.

Pixel detector

The pixel detector is a silicon pixel detector with 288 modules each with 46080 pixel elements. These are arranged as three central barrels at average radii of ~ 5 cm , 9 cm and 12 cm and three discs on each side at radii between 9 to 15 cm. This means that the pixel detector has a very high granularity which provide high precision measurements of tracks as close to the interaction point as possible.

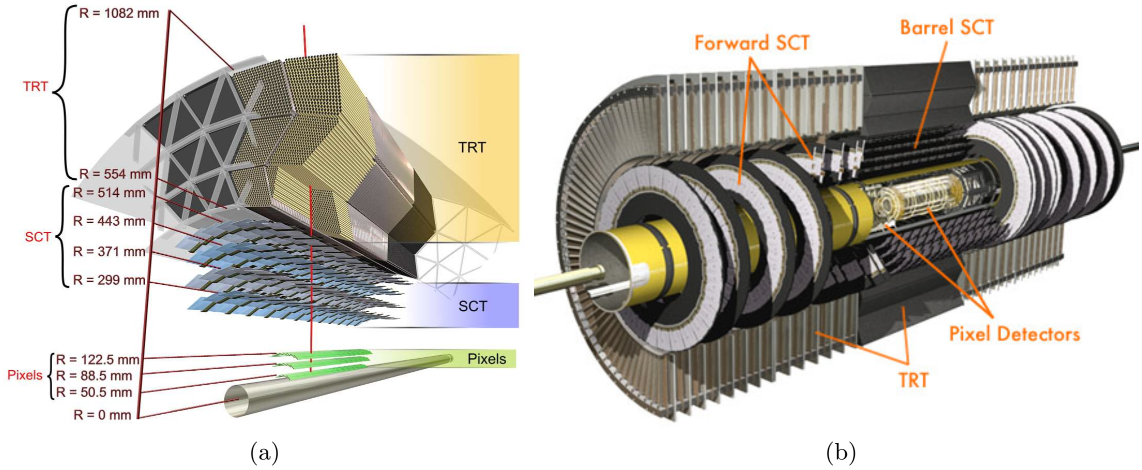

Figure 3.14: The ATLAS inner detector

SCT

The SCT is similar in construction and function to the pixel detector but differs by having long narrow strips rather then small pixels. This enables it to cower a larger area giving more sampled points and with this roughly the same accuracy although the strips are read out one-dimensionally opposed to the pixel detector, where each pixel gives a signal (readout) with two-dimensional information. The SCT is designed to provide eight precision measurements per track in the intermediate radial range. Together with the silicon detector this enables exact determination of where the interaction occurred (the vertex position), how much momentum a particle has (due to its curvature in the magnetic field) and secondary vertices and impact parameter, that help understand the process and is central in the tagging of jets stemming from bottom quarks.

TRT

The transition radiation tracker is the outermost of the three inner detectors. It is a detector made of straws containing gas with a wire at the centre to detect electromagnetic showers. It is designed with straws 4 mm in diameter and with a gold-plated wire 30μm in diameter to allow for the high track and readout rate expected. The barrel contains about 50.000 straws with length up to 144 cm divided at the centre and read out in both ends while the end caps consist of no less than 320.000 radial straws readout at the outer radius. The gases in the straws are a nonflammable mixture of 70% Xenon, 27% Carbon dioxide and 3% Oxygen. When a particle crosses a straw, the atoms of the Xenon gas are ionised resulting in free electrons. As the central wire carries an electric potential of 1.5 kV, the electrons will drift towards the centre. The drift of electrons creates secondary ionisation which results in an avalanche of electrons reaching the wire. This allows for a readout of the signal giving a drift time measurement, that gives a spatial resolution of 170μm per straw.

Additionally the material between the straws, called the radiator, is composed of materials with different dielectric constants. This causes ultra-relativistic particles to radiate off photons in the X-ray region. Xenon is chosen as it is particularly sensitive to absorbing those photons resulting in massive ionisation and a much larger signal readout. This type of signal is called a high threshold signal while signal from simply ionising charged particles is called low threshold. This is used to separate electrons that cause transition radiation from particles like the pion.

3.6.2 The Magnet system

ATLAS has two different magnet systems, the Solenoidal magnet and the Toroidal magnets. The solenoidal magnet is a superconducting magnet made from a composite that consists of a flat superconducting cable located in the centre of a rectangular aluminium stabiliser. The magnet is designed to provide a 2 T magnetic filed parallel to the beam axis with peaks of up to 2.6 T. It is placed so the magnetic field surrounds the inner detector while the field in the calorimeters is minimal and the radial thickness is minimal to insure minimum impact in the calorimeter measurements. The magnetic field causes particles to bend according to their charge and momentum, so these quantities can be determined in offline analysis. This bending also means that particles below roughly 400 MeV are curved to a degree where they will loop repeatedly in the field and are less likely to be measured. This help to reduce the noise of the irrelevant low energy particles.

The Toroidal magnet system is made of eight very large air-core superconducting coils forming a barrel, symmetric around the beam axis, and two end-cap parts rotated with respect to the barrel so the coils interleave. It is situated outside the calorimeter and within the muon systems. For the barrel, each coil has its own cryostat, with the coils connected together to form a rigid cold mass which contains the large magnetic forces acting radially inwards.

The toroid system creates a magnetic field around 4 T which is strong enough to bend particles (muons) with energy up to 1 TeV, poorly measured by the inner part of the detector, so their momentum and charge can be determined.

3.6.3 The Calorimeters

There are two different calorimeter systems in the ATLAS detector. The electromagnetic- (EM) and hadronic- calorimeter. They are both *sampling calorimeters* which means they alternate layers of high density absorbing materials and active sampling layers, which collect the signal from the resulting particle shower. The energy of the passing particles can be inferred from these showers. The physics governing the two calorimeters are however not the same.

EM calorimeter

The electromagnetic calorimeter is a Liquid Argon calorimeter with interlacing layers of lead and stainless steel. To keep the argon in its liquid state a cryostat surounds the entire EM calorimeter. Lead is chosen for the interlacing plates, as it has a short radiation length which means electrons or photons moving through the calorimeter will shower and create a cascade of photons within short distances. The secondary electrons will ionise the argon in the narrow gaps. An electric field results in the electrons drifting in the gas-gaps and being readout by copper electrodes. The size of an electromagnetic shower depends linearly in units of radiation length X_0 of the calorimeter material. Figure 3.15a illustrates the electromagnetic calorimeter. The calorimeter can be split into four layers.

- **The presampler** is a single layer of argon without any lead in front. The sole purpose of this layer is to correct for the energy loss in the inner detector, the solenoid magnet and the cryostat wall.

- **The 1st sampling** has a layer of 4.3 radiation lengths in depth. The readout is done from thin strips positioned in the η direction (see Fig. 3.15a) which provide good resolution in this coordinate for photon/π^0 separation. The magnetic field causes photons to produce showers similar to the π^0 in the ϕ direction hence the above choice.

- **The 2nd sampling** is with its 16 radiation lengths of material the largest layer in the EM calorimeter and it is here the largest part of the energy is deposited. All clusters with energy below 50 GeV are contained within the second sampling. [37]

- **The 3rd sampling** is a layer that will only be reached by the most energetic clusters and the cell sizes have been doubled in η without loss of resolution, as the energetic clusters reaching this layer will be wide. The EM calorimeter is thus essential in the determination of energy of electrons and photons and in separating neutral pions and photons.

The end-cap regions are split into two. Out until $|\eta| = 3.2$ the structure is the same as for the barrel but without the presampler and with less material. From there out to $|\eta| = 4.9$ the calorimeter is made from copper and tungsten. This choice was made to limit the width and depth of showers from high energy jets close to the beam pipe and to contain particles from the forward region.

The overlapping region between the barrel and the end-cap calorimeters result in a "dead area" with poor energy resolution but this area has been made as small as possible with room still for the cables and cooling pipes for the inner detector

Hadronic calorimeter

The hadronic part of the calorimeter in ATLAS is situated outside the cryostat of the EM calorimeter. It is a tile calorimeter build of a steel frame with plastic scintillators inserted as tiles. An outgoing slice of the calorimeter can be seen in Fig. 3.15b. The scintillators emit blue light from ionising particles (both charged and neutral hadrons and leptons). The blue light is sent via wavelength-shifting fibres to the outside of the calorimeter where photomultipliers read out the now longer wavelengths from the fibres.

Unlike the electromagnetic showers, that have a rather constant shower-energy to particle-energy ratio, the energy deposited by hadrons in the hadronic calorimeter varies much. Neutral pions decay to photons like in the EM calorimeter while secondary $\pi^{\pm}$, neutrons etc. from the nuclear processes, caused by incoming particles interacting with the material in the hadronic calorimeter, give large variations in the estimate of their energy. The size of hadronic showers depends linearly on the interaction length λ of the material which is always longer than the radiation length. [37]

In order to compensate for the variations of the hadronic showers, the ratio of the EM- and the hadronic- calorimeter, e/h, is measured. For a good energy resolution this value should be as close as possible to one.

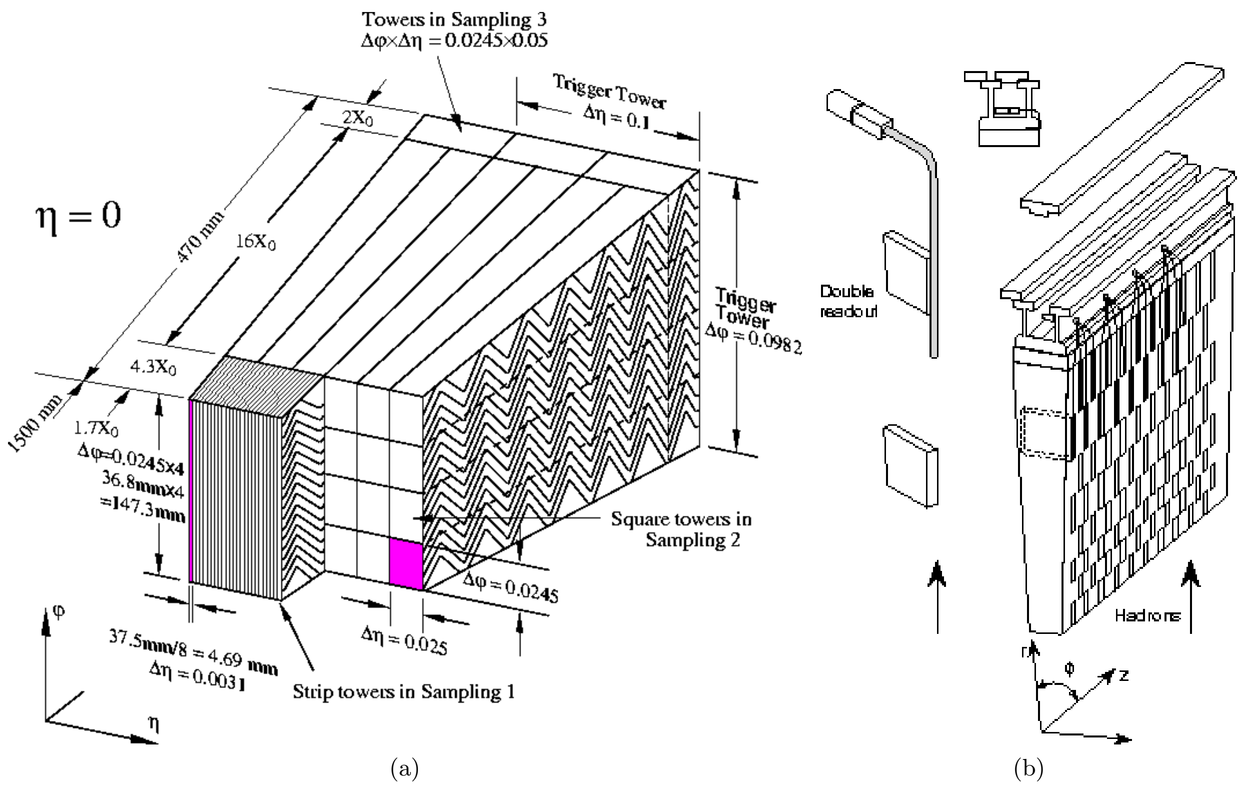

Figure 3.15: The ATLAS Calorimeters. Figures from [37]

3.6.4 The Muon detector

The last and outermost detector is the muon detector designed to catch the muons that have otherwise deposited little energy in the inner parts of the detectors. The principle for the detector is like for the inner detector. The magnetic field from the toroid bend the muons, so their momentum and charge can be identified and nearly all tracks in the muon detectors can be considered muons, as few other particles make it through the calorimeters to the muon detector.

The detector is composed of two types of muon detectors in three layers. The monitored drift chambers (MDT's) and the cathode strip chambers (CSC). The MDTs are drift chambers consisting of pressurised thin-walled aluminium tubes with a diameter of 30 mm. The tubes are placed transverse to the beam axis so the coordinates can be measured in the bending plane. The tubes are filled with a mix of Argon and Carbon dioxide at a pressure of 3-4 bar which give a single cell resolution of about 60μm. Their readout time is high due to the long drift-time (due to radii of 15 mm) which means the MDT's cannot be used for triggering. For that, ATLAS relies on the CSCs.

The CSCs are multiwire proportional chambers of which two different kinds are used. Resistive Plate chambers (RPC) are used in the barrel while Thin Gap Chambers (TGC) are used in the forward regions. The RPC consist of two resistive bakelite plates with metal strips separated by a gas gap. A uniform electric field between the plates creates avalanches which are measured by the metal strips. These chambers have a time resolution of around 1 ns allowing them to be used for triggering purposes as will be described shortly. TGC is a wire chamber with a saturated gas with capacitive strips for readout. This gives a time resolution of less than 5 ns which is also satisfactory for triggering. The reason for choosing two type of chambers for triggering are simply based on costs.

The typical signals left in the ATLAS detector for different particles is drawn in Fig. 3.16. For our study the electrons and muons are important, but as is clear from the above no part of the detector could be left out. The force of the many sub detectors lie both in their individual specialisations but certainly also in their combinational possibilities.

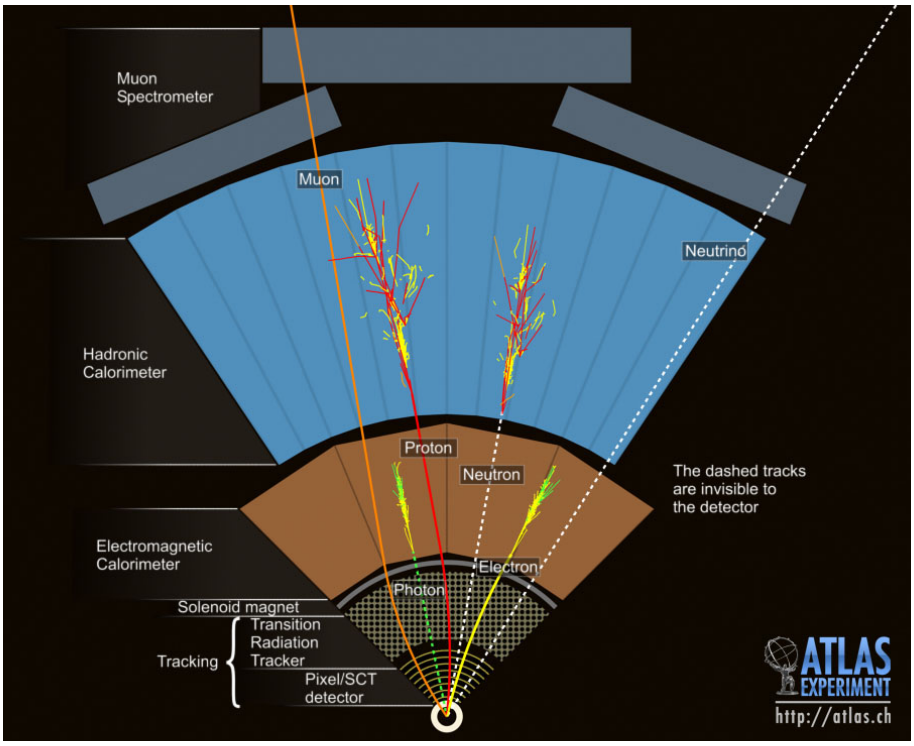

Figure 3.16: The signal from various particles as seen in the ATLAS detector. Different particles leave signals in different parts of the detector and can be identified from this.

3.7 The triggering and data acquisition systems

To round off the experiment section, a few words about the triggering and data distribution- and analysis- systems are needed.

3.7.1 The trigger-system

When LHC is running at peak design luminosity, the interaction rate will be of the order of 1 GHz with a bunch crossing rate of around 40 MHz. This means that approximately 40 million proton bunches collide every second. Each collision results in an event with raw data. If all these events were to be stored, the total amount of data from the ATLAS experiment alone would be in sizes of terabytes or even Petabytes each second. It is impossible to store such an amount and luckily not all events are equally interesting. The cross sections for production of quarks and gluons in the initial collisions are much higher than for creating Z bosons, and for many searches, the quark events are not as interesting and can be filtered away. To do this a set of *triggers* have been developed to select only events with interesting physics. The triggers can be split into two major groups. Level 1 (L1) triggers, and high level triggers (HLT).

The L1 triggers are based on hardware implemented logic decisions in the detector and get their information from the various parts of the ATLAS detector that have fast readout rates. They use this information to select regions in the detector, that might contain interesting physics and does so within microseconds. Events with no interesting regions are immediately thrown away and anaylsis is performed on the next event. This step reduces the rate to around 75 KHz.

The regions of interest, ROI, are then passed on to the HLT. The HLT consist of two steps. The Level 2, L2, trigger and the Event Filter, EF. The L2 trigger runs more thorough algorithms on the ROI's and reconstructs data in those regions to see whether it is interesting. As the rate of events from the L1 trigger is lower, there is more time to decide whether the event in question is interesting and the algorithms can be more complex. If interesting physics is found, the event is passed on with a rate around 1 KHz.

Finally the event is sent to the EF where reconstruction algorithms are run to find particles in the entire detector or just the regions of interest. If the event is found to be of interest in the end, it is sent to be recorded and is now ready for further analysis.

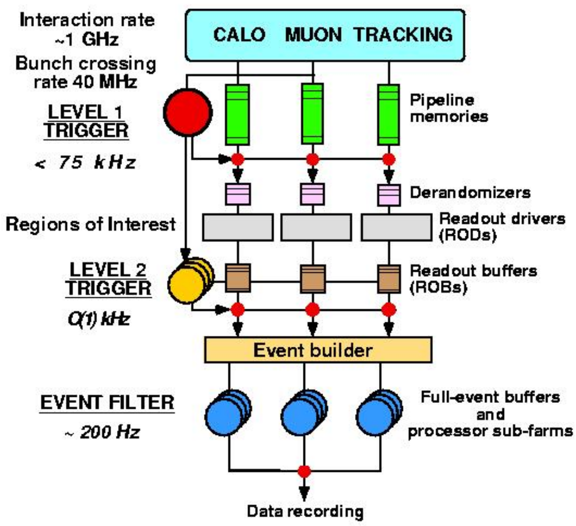

Figure 3.17: The triggering system can be split into the low-level Level 1 trigger and the high-level Level 2 and Event Filter triggers. Level 1 triggers are hardware based and use only very fast algorithms while the high-level triggers use more advanced algorithms and incorporate larger part of the detector.

There are many different triggers spanning from triggers that demand a reconstructed electron of a specific P_T to triggers demanding jets and various other processes. For triggers like the electron trigger, there are often an entire range of triggers demanding electrons with different minimum P_T or with different degree of certainty in the identification, called tightness.

The triggers have been systematically deployed during 2010.

3.7.2 The GRID

In order to analyse the huge amount of data that is being stored even after triggers, scientists use *GRIDs* of computers all around the world. Computers are at many different locations around the world placed in clusters typically of a few thousand computers. For the analysis of data, the different runs are then reprocessed into more manageable sizes.

The grid framework of the LHC is called the WLCG (Worldwide LHC Computing Grid). It incorporates 140 computer centres in 34 countries. This GRID is made up of four levels of "tiers" [38]. The tiers range from 0 to 3. Tier 0 is at CERN and has the highest degree of detail available in data-samples. The degree of detail is cut down going outwards and the tier 3's are left with only what should be needed for physics analysis. The Monte Carlo- and data- samples of this thesis have all been made and analysed using the GRID.

Part III

Analysis

Chapter 4

Generator level studies

4.1 Motivation for an $e\mu$ final state

The study presented in this thesis focuses on final states of type $e^{\pm} + \mu^{\mp}$. The study of this channel in other experiments, at a similar early stage, has proven to provide better statistical precision in cross section measurements than an exclusive and separate measurement of each single Standard Model process contributing to this final signature [1].

Exclusive analyses rely on cuts to separate a single signal process, from all backgrounds in a channel. These cuts can be relaxed significantly, if an inclusive study is performed, letting more events pass which result in better statistics. Hence this study will allow for a detailed test of several Standard Model processes in the new energy regime, before the results of exclusive analyses are likely to become available for all of them.

If indeed better statistical uncertainty can be achieved the method is useful for other studies concerning measurements of various signals in the dilepton channel. As already emphasised the dilepton channel is central for some of the most interesting signals that could exist at the LHC with the obvious example of Higgs decay to dilepton final states.

This study will also provide a valuable comparison to separate studies of these Standard Model processes in different analyses with other decay final states, as well as comparison with existing exclusive studies in the same decay channel.

4.1.1 Signals in an $e\mu$ final state

For a high-P_T $e^{\pm}\mu^{\mp}$ final state there are three major Standard Model processes contributing. These are

$$\begin{array}{lllllll} pp & \rightarrow & Z/\gamma * & \rightarrow & \tau^{\pm} + \tau^{\mp} & \rightarrow & e^{\pm} + \mu^{\mp} + \nu' s \\ pp & \rightarrow & W^{\pm} + W^{\mp} & \rightarrow & e^{\pm} + \mu^{\mp} + \nu' s & & \\ pp & \rightarrow & t + \bar{t} & \rightarrow & b + \bar{b} + e^{\pm} + \mu^{\mp} + \nu' s & & \end{array} \tag{4.1}$$

The Feynman diagrams for the processes were already shown in Figure 3.2. The Z interacts with both leptons and quarks and can therefore decay to either. The rate for decays can be calculated and it is found, that $\sim 70\%$ of the Z decays are into hadrons, $\sim 20\%$ are into two neutrinos and $\sim 3\%$ are into each of the lepton flavours. It cannot decay directly into an electron and a muon, as this would violate the lepton number conservation, but τ has $\sim 17\%$ chance of decaying into an electron or a muon. The branching ratio for all processes are in Table 4.1

The W also interacts with both leptons and quarks. It has a $\sim 68\%$ probability to decay into hadrons and $\sim 11\%$ to decay into either of the charged lepton flavours. $e\mu$ pairs are created from collisions resulting in a $W^{\pm}W^{\mp}$ pair, that decays into $e^{\pm} + \bar{\nu}(\nu) + \mu^{\mp} + \nu(\bar{\nu})$. The contributions from W's decaying to taus, that decay to leptons is negligible.

Finally the top quark couples to the Z, photon and W's but also to gluons. Decays of tops to lighter quarks through a photon or a Z boson has been excluded to are branching ratio less than 0.6% and 4% respectively. [39] The only relevant decay is thus by a W to a lighter quark through emission of a lepton pair or a quark-antiquark pair. The probability of this being a $l^{\pm}\bar{\nu}(\nu)$ pair is $\sim 9\%$ for each top.

$\Gamma(Z \to \tau\tau \to e\mu)$	0.2%
$\Gamma(WW \to e\mu)$	2.3%
$\Gamma(t\bar{t} \to e\mu)$	1.8%

Table 4.1: Branching ratios

From this it is clear, that the only other objects apart from the leptons in the events are neutrinos and jets both from initial and final state radiation and from quarks (b's) from top decays [1]. The neutrinos can be identified by measuring the missing energy in the detector which make it an obvious choice when selecting the observable for the fit of data to expectations. The neutrinos from the W decays are expected to have higher energy than neutrinos from the Z, as the Z decays through taus, that share the energy of the Z. The neutrinos from the top quarks are also expected to take away a significant part of the total energy.

Various variables could be used to measure the jets content of the event. The demand is that it separates well the three different signals. From studies at the Tevatron [1] we know that number of jets is a good variable. The top decays will result in a minimum of two jets from the two b quarks, while both the Z and WW will prominently not have jets apart from initial- and final state showers. This means the $t\bar{t}$ process is separated further from the two other processes in number of jets. The Z and WW cannot be expected to lie in different regions in number of jets, but they are expected to be separated adequately by their difference in missing energy. Thus the two dimensional number of jets - missing energy phase-space should see the three signals distributed differently.

If the only requirement was an $e^{\pm}\mu^{\mp}$ final state many other processes would contribute significantly to the process, for instance the bottom quark can decay through a W like the top, but by selecting only leptons above a certain P_T many processes are suppressed to a degree where their contribution is no longer relevant.

4.1.2 Background to an $e\mu$ final state

Diboson events like ZZ and WZ will constitute a significant background to this signal as they can obviously decay to the same final state. ZZ will have one Z decaying to a tau pair and the other hadronically or into neutrinos. There is also the possibility that each Z could decay into electrons and muons respectively. If the P_T of one of each of the electrons and muons is lower than the imposed cut to select only high P_T leptons, this could result in an $e\mu$ signal being selected. WZ can also decay with the Z going into taus and the W decaying

[1] The beam remnants will show up as jets in the event as well. Beam remnants are process independent and will characterise any study and is for this reason not discussed further here.

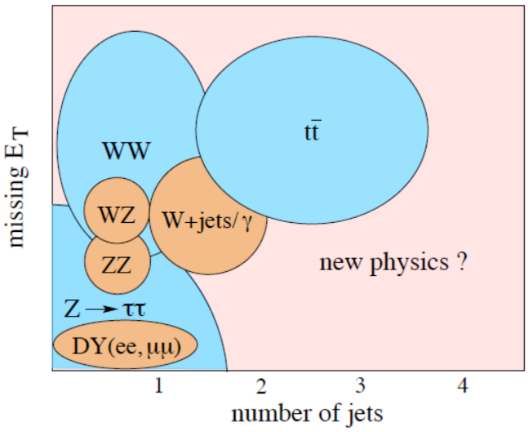

Figure 4.1: The distribution of the different processes in the number of jets vs. missing transverse energy phase-space, as probed by the CDF experiment. [1]

hadronically or alternatively the W decaying to an electron or muon while the Z decays to a pair of muons or electrons, again with one below the P_T cut. As a last possibility the W could decay leptonically while the Z decays semileptonic via taus.

Processes like $W \to l + \nu + jets$ can also contribute to the background, as quarks (hadrons) in the jet can decay to lighter quarks (hadrons) through emission of a leptons. The leptons will here come predominantly from b-quarks. [2] $W \to \mu^{\pm} + \gamma$ will act as a background if $\gamma \to e^+e^-$, with only one electron, carrying P_T larger than the P_T cut, being reconstructed. The photon will not decay to muon pairs so $W \to e^{\pm} + \gamma$ will not constitute a significant background. Top quarks will of course also be generated alone with a significant cross section. There are different channels that could be contributing and these have all been tested. The only channel, that turned out to have a significant contribution based on the Monte Carlo simulations is the Wt channel with the leading order process $b + g \to W^- + t$ [40]. More common QCD dijet final states, stemming from hard partons (quarks , gluons) produced in the collisions, could be a potential background but due to the demand on lepton transverse momentum only bottom quarks are in practice heavy enough to contribute to the true $e\mu$ background.

In a world of perfect detectors this would be the only background, but as detectors have limited precision particles such as pions can actually be misidentified as electrons altering the background. Furthermore the detector has crack and inefficiencies and some leptons might not be reconstructed although they are present in the event. This affects all processes and for what is generally referred to as soft QCD, i.e. processes involving the light quarks, this means that an $e\mu$ signal could come from an event, that had no electrons at all. It becomes important to consider this rather unlikely background due to the very large cross section soft QCD events turns out to have in proton-proton colliders. The significance of the different background processes will be clear after selection has been performed and contributions from each source will be listed later.

[2] The study was performed by Tony Shao from the group working with this analysis but the results have not been published.

Studies have been made in the group working with this analysis that show b quarks are the only significant QCD background for the $e\mu$ channel. The study probed the isolated and non-isolated electrons found in a variety of minimum bias samples. The particles, these electrons originated from, were found to be distributed as shown in Table 4.2.

Table 4.2: The origin of electrons in QCD samples

68% real	32% fake
74% b quarks	10% b quarks
23% conversions	5% c quarks
3% c quarks	85% light quarks

Light quarks faking muons were non-existing. The c-quarks present in Table 4.2 were mainly from b-quark decays. The conclusion was, that the majority of reconstructed electrons came from B meson decays as all lighter quark contributions were killed by simple P_T and isolation demands. The selection of events containing an electron and a muon will be described later, but the next section will concern the reconstruction of jets at generator level, as the number of jets plays a fundamental role in this study.

4.2 A closer look at one of the three main processes

As described in the theory section the electroweak interaction between the initial partons and final state τ's in the Z $\rightarrow \tau^+\tau^-$ process cannot be separated from the same process with an excited photon as the force carrier. From theory we expect the contribution to be mainly from Z in the high energy region, but dominated by γ for the low energy region. In order to test this we have run a series of Monte Carlo experiments using Pythia 8 [24].

4.2.1 The influence of different production parameters

Pythia holds the option to switch on and off different processes like choosing pure Z, a combination of Z and γ^* or pure γ^*. Furthermore initial state radiation (ISR) and additional quarks and gluons as final state radiation (FSR) can be switched on.

In Figure 4.2 the invariant mass of τ's from the decay have been calculated for different production processes. For all cases, 10000 events were generated with a phase-space cut of 5 GeV on the minimum invariant P_T of both particles and with both FSR and ISR. As can be seen in Figure 4.2a the invariant mass of the τ's shows a peak around 91 GeV close to the value measured today for the Z boson of 91.1876 ± 0.0021 GeV/c [39]. In Figure 4.2b the picture changes with the introduction of full Z/γ^* interactions, and the peak disappears completely in Figure 4.2c where the production is purely from γ^*. The γ "tail" of course continues leftward but is cut off here at 10 GeV as the cut on minimum invariant P_T in the phase space has been used to simulate higher energy γ's.

In Figure 4.3 the P_T of the leptons originating from the τ's is plotted. Fig. 4.3a is for the case of pure Z and as can be seen the electrons have P_T ranging up to above 40 GeV and with a large fraction above 15 GeV. The P_T of the electrons from a pure gamma production, as can be seen in Figure 4.3b, falls off much faster and there are only a few electrons with $P_T \geq$ 15 GeV. The same is the case for muons as is seen in Figure 4.3c and 4.3d. A cut on the P_T

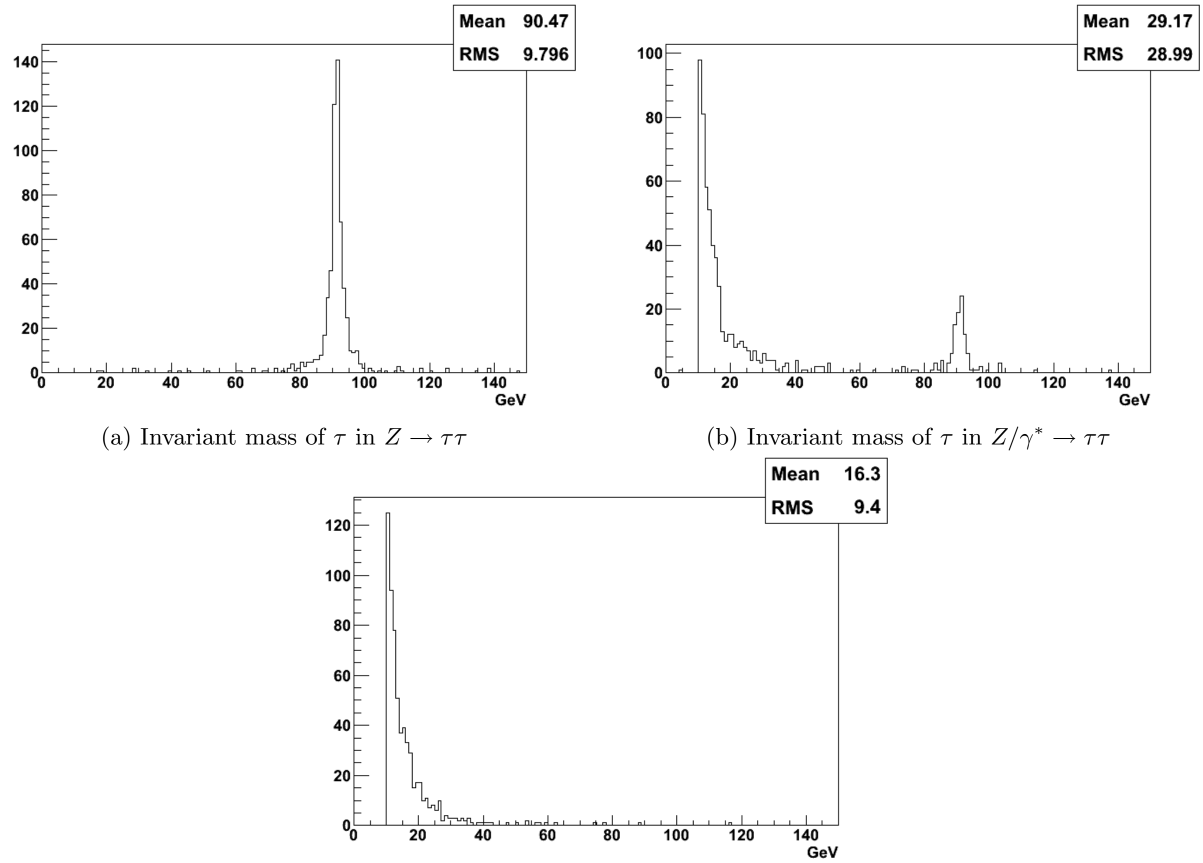

(a) Invariant mass of τ in $Z \rightarrow \tau\tau$

(b) Invariant mass of τ in $Z/\gamma^* \rightarrow \tau\tau$

(c) Invariant mass of τ in $\gamma^* \rightarrow \tau\tau$

Figure 4.2: Invariant mass of taus from different processes

of leptons of 15 GeV will effectively sort away nearly all γ^* contributions. We find, that the percentage of γ^*'s in $Z/\gamma^* \rightarrow \tau\tau$ after the P_T cut is around 1%. More precisely around 1.2% of γ^* events pass the demand of a P_T of 15 GeV when applied on both leptons. The choice of 15 GeV was simply to retain high statistics while surpressing the γ contribution. The cut has been used along with the demand of $e^{\pm} + \mu^{\mp}$ to minimise the signal contribution additionally from background processes while keeping as many events from the signal processes as possible.

The P_T distribution for WW and $t\bar{t}$ in Figure 4.3 shows that the leptons carry more P_T then the leptons from $Z \rightarrow \tau\tau$. This is expected, as the taus carry approximately half the Z energy and give a significant part to the neutrino while leptons from the W and top processes get approximately half the W and heavier top energy respectively. The demand of leptons with a P_T above 15 GeV is obviously much harder on $Z \rightarrow \tau\tau$ compared to $t\bar{t}$ and WW, and choosing the relatively low value of 15 GeV allow a large fraction of the signal from all processes to pass.

The b-quarks in top decays could decay into leptons and thus affect the P_T distribution for $t\bar{t} \rightarrow e\mu$. To test this the amount of events with leptons coming from B-mesons and not top-quarks have been simulated. Before cuts, the ratio of both opposite sign leptons coming from B-mesons to both coming from top quark decays in $t\bar{t}$ is 0.1 % calculated with Pythia. The ratio of one of the opposite sign leptons coming from a B-decay and the other coming

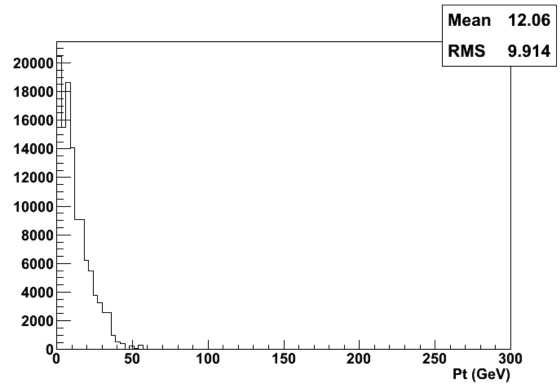

(a) P_T of electrons from τ in $Z \to \tau\tau$

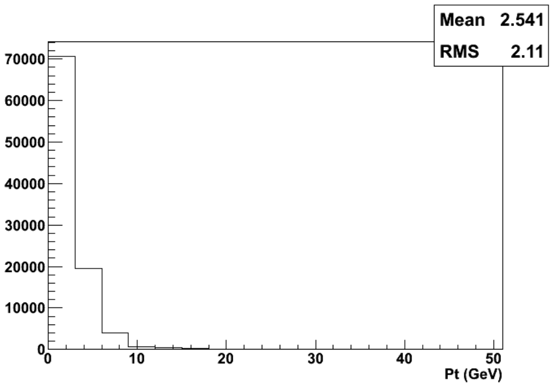

(b) P_T of electrons from τ in $\gamma^* \to \tau\tau$

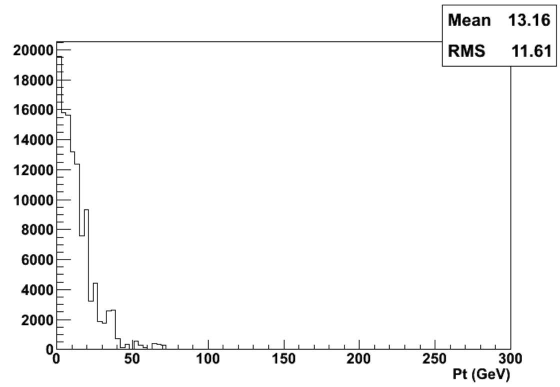

(c) P_T of muons from τ in $Z \to \tau\tau$

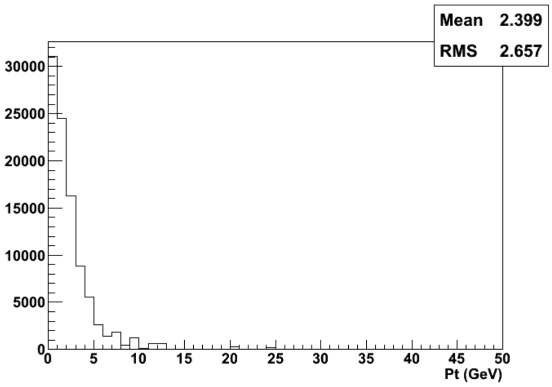

(d) P_T of muons from τ in $\gamma^* \to \tau\tau$

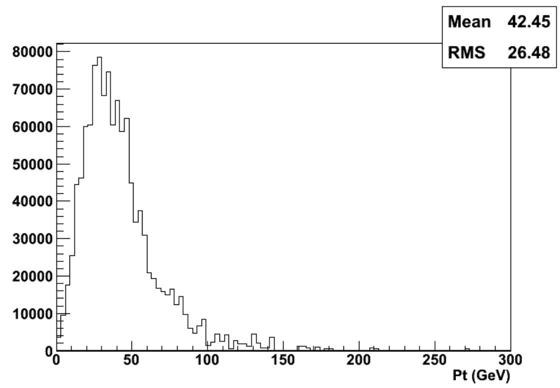

(e) P_T of electrons from WW production

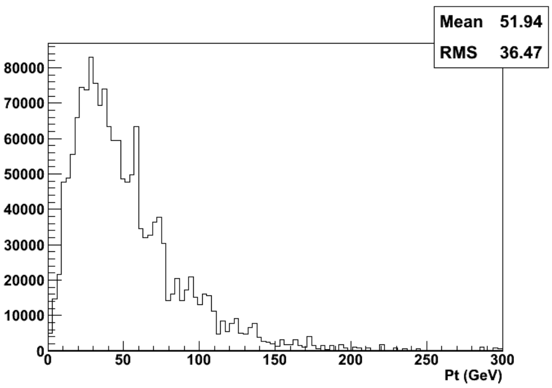

(f) P_T of electrons from $t\bar{t}$ production

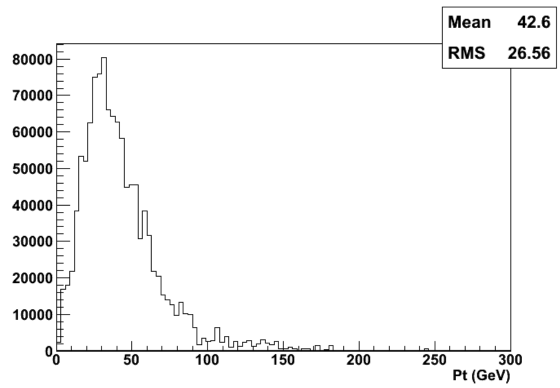

(g) P_T of muons from WW production

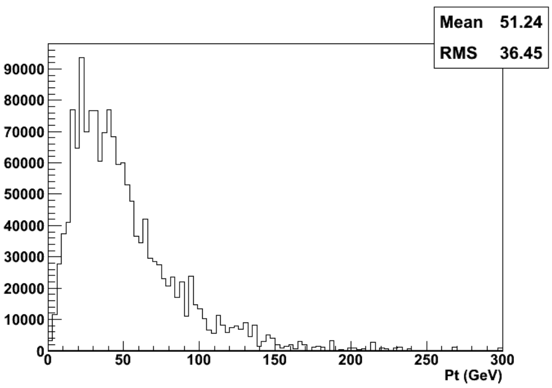

(h) P_T of muons from $t\bar{t}$ production

Figure 4.3: Transverse momentum of leptons from different processes. Numbers on y-axis are arbitrary. Note the different P_T range in the $\gamma*$ distributions.

from a top to both coming from tops is 5%. After a P_T cut of 15 GeV the same ratio is 2%.

Table 4.3: Pythia process cross sections

process	σ_{gen} (pb)
$q\bar{q} \rightarrow Z/\gamma^*$	4089
$q\bar{q} \rightarrow Z/\gamma^* + ISR$	4069
$q\bar{q} \rightarrow Z/\gamma^*$ + FSR	4087
$q\bar{q} \rightarrow Z$	720.6
$q\bar{q} \rightarrow Z + ISR$	721.1
$q\bar{q} \rightarrow Z + FSR$	721.7
$q\bar{q} \rightarrow \gamma^*$	3358
$q\bar{q} \rightarrow \gamma^* + ISR$	3370
$q\bar{q} \rightarrow \gamma^* + FSR$	3369
$q\bar{q} \rightarrow t\bar{t}$	98.80
$gg \rightarrow t\bar{t}$	30.51
$q\bar{q} \rightarrow WW$	32.69

The production cross-sections can be found by Pythia as described in the section on Monte Carlo generators. We have been using the Pythia default pdf CTEQ 5L [20] and results are listed in Table 4.3 for the three signal processes. The σ_{gen} is the signal production cross-section. The cross section for producing an oppositely charged electron-muon pair can be found by multiplying with the branching ratios.

It is interesting to compare these cross sections to the earlier MadGraph cross sections. These were given in Figure 3.1 and looking just at the $Z \rightarrow \tau\tau$ we got a total of 509 pb whereas Pythia gives 4089 pb $\cdot\Gamma_{Z\rightarrow\tau\tau} = 138$ pb. The difference is significant and partly stems from the fact, that Pythia is strictly leading order opposed to MadGraph, that includes some higher order corrections. Furthermore Madgraph uses the newer pdf CTEQL1 [20]. The conclusion is that optimising both calculation of the hard process and including newest parton distribution functions is really important for which reason they have been taken into account in later results.

4.3 Jet Reconstruction

The reconstruction of jets, demands a section by itself. The particle multiplicity per event in a proton-proton collider with energies and luminosity like the LHC are generally very high and an underlying "noise" of low energy particles are almost always present in collisions. The reconstruction of jets are attacked from two very different fronts.

1. Which particles do we combine into a jet?
   - This is described by what is called the jet algorithm and defined by its parameters.
2. How do we combine the momenta of those particles into a single jet momentum?
   - Refered to as the Recombination scheme. Most widely used method is 4-vector sums (E-Scheme) [41]

Fundamentally different algorithms as well as algorithms with different parameters give relatively large differences in number of reconstructed jets. The following will give a description of what physics lies behind reconstructing jets as well as discuss the various definitions that make jets reconstructed from the true particles in the same event differ depending on the method.

4.3.1 A jet

A jet is a general definition of particles originating from the same parton (quark/gluon) and moving out through the detector within a cone or area of some predefined size. Typically jets stems from quarks or gluons that undergo fragmentation due to colour confinement and split up into hadrons that again decay to other particles. As the momentum in the direction of the original decay tends to be much larger than the mass of the decay products in the beam, the result is a narrow beam or cone of particles e.g. an area of relatively high energy density shooting out through the detector. Jets can however also consist of other particles e.g. electrons can be reconstructed as a jet besides being identified as an electron, adding to the number of jets in the event, if measures to avoid this are not introduced.

4.3.2 Reconstruction algorithms

Seeded cones

An obvious way of defining and finding jets based on the above, is based on two parameters: the P_T of the possible constituents and the distance of these from each other or more precisely from the selected centre of the jet. This type of jet is called the seeded fixed-cone jet. [42]. All inputs are sorted by decreasing order in P_T . The object with highest P_T is then selected and if it is above the defined seed threshold, all objects within a cone of given radius, are combined with the seed. More precisely the cone is defined in pseudo-rapidity η and azimuth ϕ with a radius $\Delta R = \sqrt{\Delta\eta^2 + \Delta\phi^2} < R_{cone}$, with R_{cone} being the fixed cone radius. A new direction is calculated from the four-momenta of the initial cone and a new cone is centred around this new direction where objects are collected as before[3]. This procedure is repeated to the point when the direction of the cone does not change with further repetitions. This is now called a jet and the analysis continues with the selection of the object with second largest P_T which is again iterated as before until a jet is found. This continues until all input with values larger than the required seed, have been turned into jets. Now obviously some of the jets share constituents, as there was no demand, that the input object was not already part of a jet. This can be compensated partly for by introducing a merging and splitting mechanism. A jet, that shares constituents with P_T summing to above a fraction f_{sm} of the P_T of constituents of another less energetic jet, is merged with this jet. Vice versa the two jets are split if they share less than f_{sm}. The relevant values for the ATLAS experiment are $f_{sm} = 0.5$, a seed threshold of $p_T > 1$ x and the two cone sizes $R = 4$ and $R = 7$ [4]. This jet is by design only meaningful to leading order for inclusive cross-section measurements and final state W/Z+1 jet. To test what is called infrared, IR, safety, soft particles (low energy) are added to an event with $2 \leq N \leq 10$ hard particles. The seeded cones are reconstructed, and the procedure is repeated. If the jets are IR safe as they should be, this should not change

[3]Bear in mind, that these objects might and often will be the same as already collected in the previous cone.

[4]The values are 0.4 and 0.7 but the notation used in ATLAS is 4 and 7.

jets. For 3 jet (or more) final states like for W/Z + 2 jets as in my study this is not always true even to leading order for the seeded cone with splitting. [41] [42]

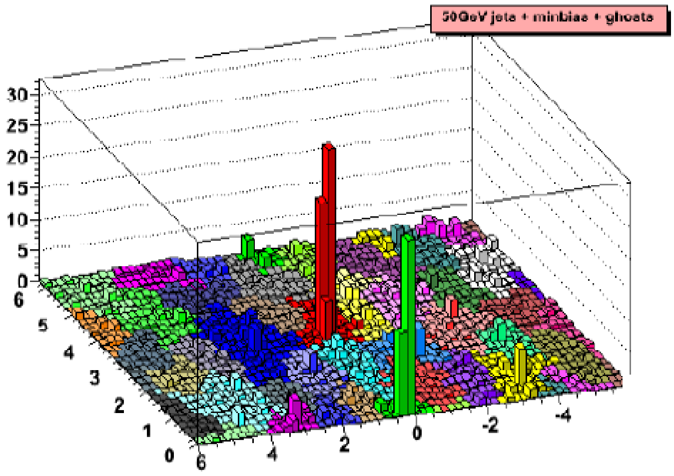

Figure 4.4: As illustrated by the figure a simple two-jet event in ATLAS is not necessarily easy to reconstruct, as "noise" from different particles and from calorimeter out-read create a significant underlying signal, that has to be taken into account by the jet algorithms. The clustering time - the time to combine the different regions of energy - goes up by a factor 1000 due to this noise.

Sequential recombination algorithms and k_T

An alternative procedure for reconstructing jets is sequential reconstruction represented by the k_T algorithms at ATLAS. The idea is that all objects are compared in pairs by a parameter composed of the smallest of the two object P_T's squared multiplied by a distance in η - ϕ space, that is:

$$d_{ij} = min(P_{T,i}^2, P_{T,j}^2)\frac{\Delta\eta_{ij}^2 + \Delta\phi_{ij}^2}{R^2} \tag{4.2}$$

Simultaneously the squared P_T of all objects compared to the beam is calculated

$$d_i = P_{T,i}^2. \tag{4.3}$$

For all objects, if the smallest value of both the mentioned is of the first type, these two objects are merged into a new object using four-momentum recombination and the process is repeated. If on the contrary the smallest value is the second type, the object is considered to be a jet by itself and removed from the list and the process is repeated. This means, that all objects end up as part of a jet or as jets by themselves. In this way no objects are shared between jets. The size of the jets can still be controlled by R and ATLAS values are 4 for narrow jets and 6 for wide jets. Besides k_T there are other variations of the Sequential recombination algorithm including Anti-k_T and Cambridge. Anti-k_T, [43] being different from k_T by changing P_T^2 to P_T^{-2}, is currently being considered as a main candidate together with

SISCone [5] [44] for usage at ATLAS in future analysis.

4.3.3 Jet Calorimeter Input

The jet algorithms base calculations on calibrated energy measurements from the detector calorimeters. The input to the algorithms from detectors can however be reconstructed in different ways. Furthermore jets can be calculated from the actual tracks or truth particles in Monte Carlo generated data in order to measure the performance of jet algorithms in simulations.

Towers

Calorimeter towers refers to one of two ways of reconstructing energy from the calorimeter cells [42]. The towers are built from a 2-dimensional grid in psudorapidity, η and azimuthal angle, ϕ with a standard grid size of $\eta \cdot \phi = 0.1 \cdot 0.1$. They are the energy sum over calorimeter cells calibrated at electromagnetic scale. As some of the cells in the calorimeter are larger, a geometrical weighting has to be done. Towers can be noise-suppressed by using a seed and neighbour cell definition referred to as 4-2-0 scheme, to select which cells to use as input for geometrical towers. The 4-2-0 algorithm is a clustering algorithm which brings us to the next type of calorimeter inputs.

Topological Clusters

Topological Clusters are 3-dimensional energy clusters meant to group calorimeter cells into clusters of energy based on the pattern of neighbouring cells' and their own energy contents. There are various methods of calculating the clusters depending on whether or not adjacent layers or even other calorimeters are used to calculate the cluster. The simplest relation, the **all2D** relation takes cells in same layer and calorimeter. It selects the neighbours in $\pm\phi$ and $\pm\eta$ direction and the four corner cells in $\pm\phi$ and $\pm\eta$. For most cells[6] this gives a total of 8 neighbouring cells. The **super3D** relation on the contrary uses inputs from anywhere across the calorimeter and even from other calorimeters, that overlaps at least partially with the current cell in the $\eta - \phi$ plane. The all3D option is the default in ATLAS and have been used for this study. The algorithm thus works by selecting all cells above a certain signal to noise ratio. Neighbouring cells are collected into the cluster and if they have a signal to noise ratio above a secondary level, their neighbours are collected as well. Finally a ring of so called guard cells are collected with signal significance above a basic threshold. Typical values could be the 4 GeV - 2 GeV - 0 GeV as mentioned earlier.

4.3.4 A study in number of jets from MC

For a more in depth study of the number of jets generated from these events we found that the default jet reconstruction algorithm in Pyhia, was not satisfactory. Instead we used

[5] SIScone is a so called Seedless Infrared Safe Cone jet algorithm i.e. it has no minimum seed, finds jets by cones but similar to the k_T algorithm in that it merges all particles, found to belong to a jet, into a new jet and then run the process again. Infrared safe also refers to the fact, that the algorithm finds the same jets whether or not soft radiation occurred in the event.

[6] This is not the case for cells at the edges of the calorimeter

Fastjet [45] which has the option to choose between different jet algorithms and parameters as well as specifying input particles and minimum jet energy.

The antiKt-algorithm was chosen as the studies include multiple jets which the antiKt-algorithm seems to cope with well. The strategy defines the algorithm for clustering from a set of N^2 and $NlnN$ algorithms [45]. The N^2 and $NlnN$ refer to the scaling of the jet algorithm complexity from N particles. In other words they refer to the number of operations that have to be performed to find the jets. "Best" chooses the best algorithm from the two given the number of particles N and the jet size R, as this may vary from one sample to another. The $NlnN$ is mainly useful for events with very high multiplicity like in heavy ion collisions while the N^2 algorithm is best suited for proton collision relevant for this study. Together with the selection of the E-scheme, where particles are added summing their four momentum, the method used corresponds to the ones described in section 4.3 where the minimum distance is found and the particles are merged into single particles/jets using their four momenta.

Before plotting number of jets, a precaution was introduced, to sort away jets from leptons. This was done by subtracting one from the number of jets each time a muon or electron was found within $\Delta R = \sqrt{\delta\phi^2 + \delta\eta^2} \leq 0.2$ of a reconstructed jet.

Figures 4.5, 4.6 and 4.7 show the number of jets with P_T above 15 GeV we get from the Fastjet algorithm with the specified inputs for Z, γ^* and Z/γ^* production respectively. Electrons or muons making a jet by themselves have been subtracted from number of jets. It is seen, that events with jets occur even when ISR and FSR is switched off. These jets stem from the beam remnants. Figures with FSR have larger number of entries while the distribution mean is lower than without ISR or FSR. What this shows us, is that FSR will lie in the same direction as the leptons from Z decay. As the leptons are subtracted from number of jets, a jet in the same direction as the electron or muon, will result in an additional entry in the zero jet bin compared to the figures without FSR or ISR.

ISR is seen to drastically contribute to the number of jets per event. This is valid for all three processes and ISR will have the main contribution to $Z \to \tau\tau$ events, that have reconstructed jets. The effects of higher order corrections e.g. the addition of a quark or gluon to the hard process has also been tested and can be seen in Figure 4.8. In Figure 4.8b there is a small tail in number of jets but otherwise a very similar distribution. The conclusion from this purely MC generator based study is that ISR is a central parameter in understanding the number of jets space and has to be included in the production mechanism for Pythia. FSR does not contribute as significantly as ISR but will contribute to the number of events having more than zero jets. Beam remnants will also contribute slightly to the number of jets as will be the case for any study. Higher order corrections also affect the outcome and may shift the distribution slightly, so more events are seen with 2 or more jets. The effect is however much smaller than ISR. The next step is to compare with the data samples used in our analysis.

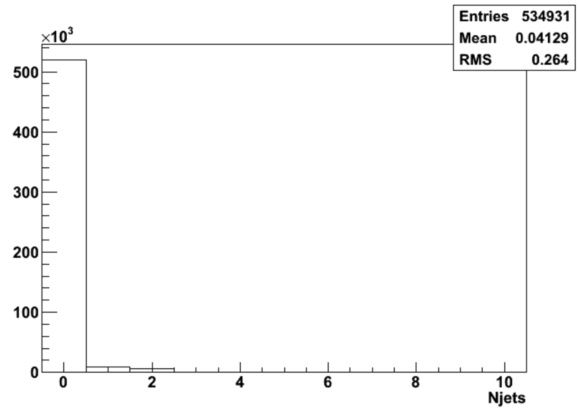

(a) Z production without ISR and FSR. Demand of $e^{\pm}+\mu^{\mp}$

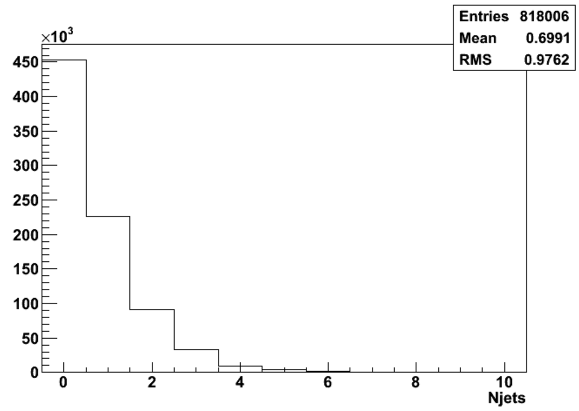

(b) Z production with ISR. Demand of $e^{\pm}+\mu^{\mp}$

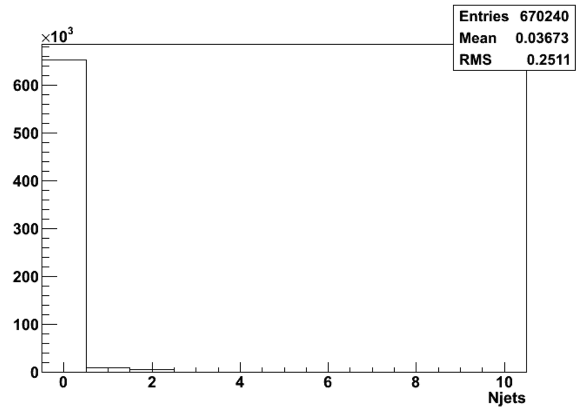

(c) Z production with FSR. Demand of $e^{\pm}+\mu^{\mp}$

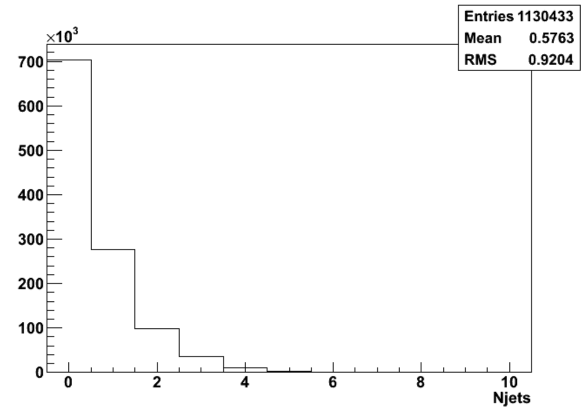

(d) Z production with ISR/FSR. Demand of $e^{\pm}+\mu^{\mp}$

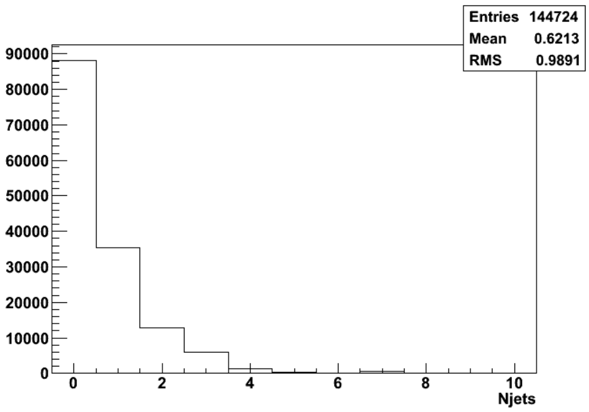

(e) Z production with ISR/FSR and demand of $e^{\pm}+\mu^{\mp}$ with transverse momentum greater than 15GeV each

Figure 4.5: Number of inclusive 15 GeV jets found with Fastjet antiKt-algorithm for Z. Numbers on y-axis are arbitrary.

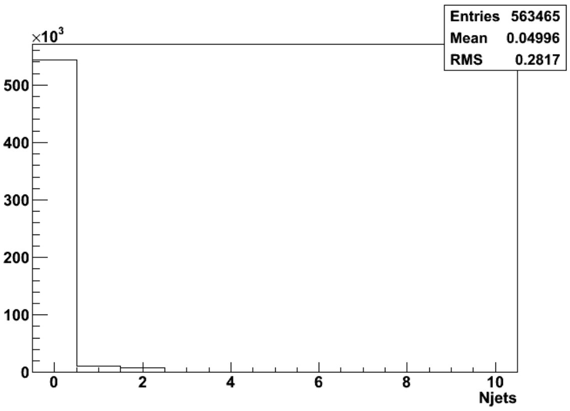

(a) γ^* production without ISR and FSR. Demand of $e^{\pm} + \mu^{\mp}$

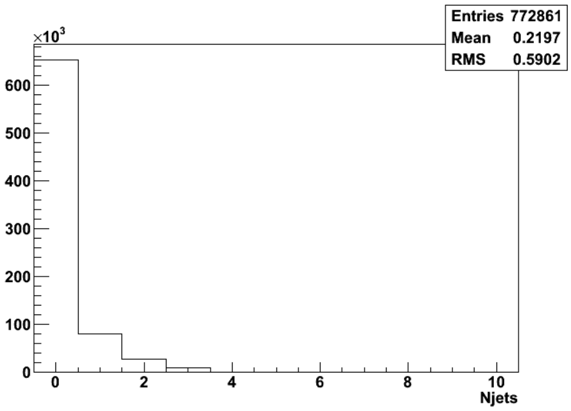

(b) γ^* production with ISR. Demand of $e^{\pm} + \mu^{\mp}$

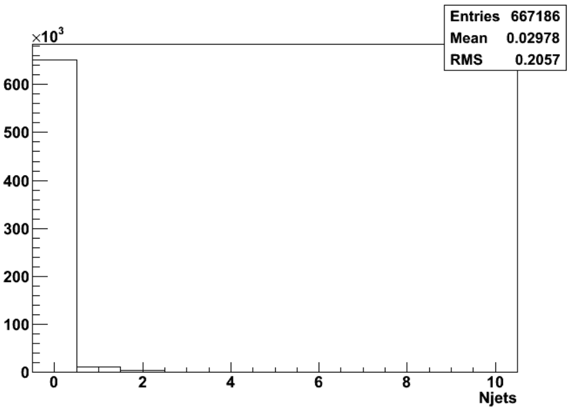

(c) γ^* production with FSR. Demand of $e^{\pm} + \mu^{\mp}$

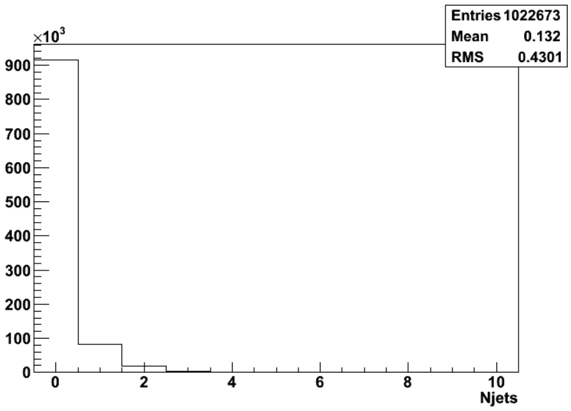

(d) γ^* production with ISR/FSR. Demand of $e^{\pm} + \mu^{\mp}$

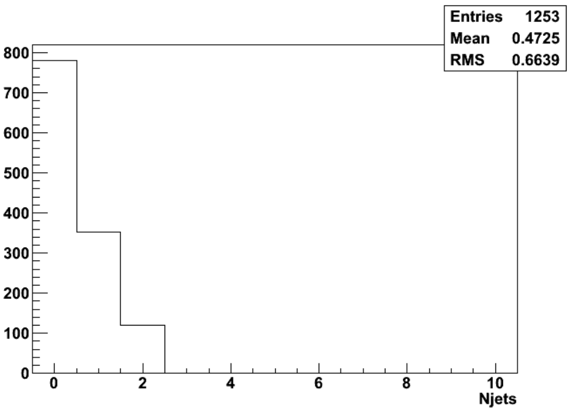

(e) γ^* production with ISR/FSR and demand of $e^{\pm} + \mu^{\mp}$ with transverse momentum greater than 15GeV each

Figure 4.6: Number of inclusive 15 GeV jets found with Fastjet antiKt-algorithm for γ. Numbers on y-axis are arbitrary.

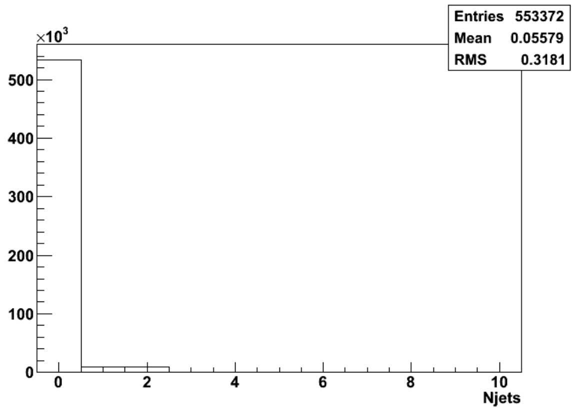

(a) Z/γ^* production without ISR and FSR. Demand of $e^{\pm} + \mu^{\mp}$

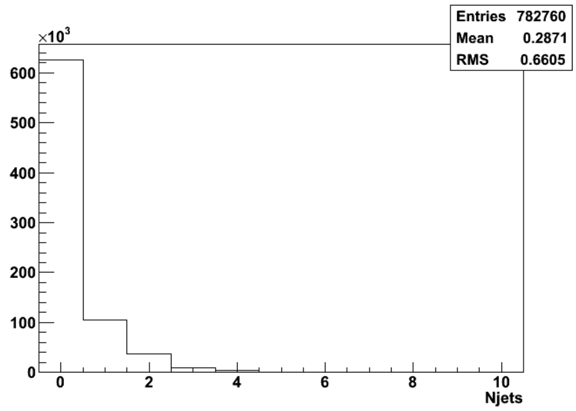

(b) Z/γ^* production with ISR. Demand of $e^{\pm} + \mu^{\mp}$

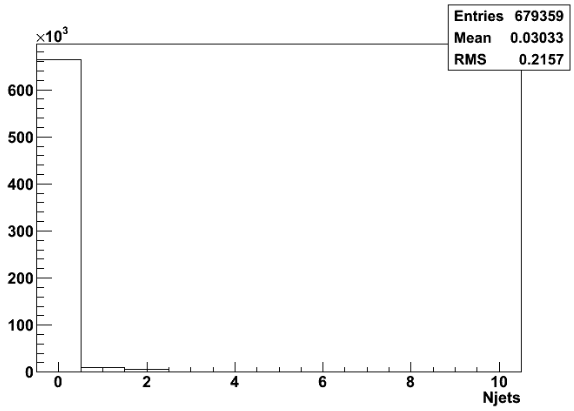

(c) Z/γ^* production with FSR. Demand of $e^{\pm} + \mu^{\mp}$

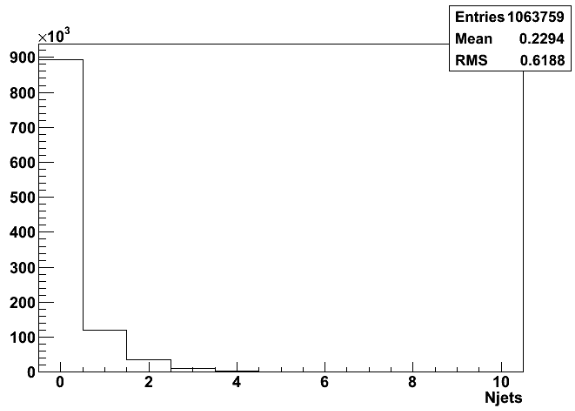

(d) Z/γ^* production with ISR/FSR. Demand of $e^{\pm} + \mu^{\mp}$

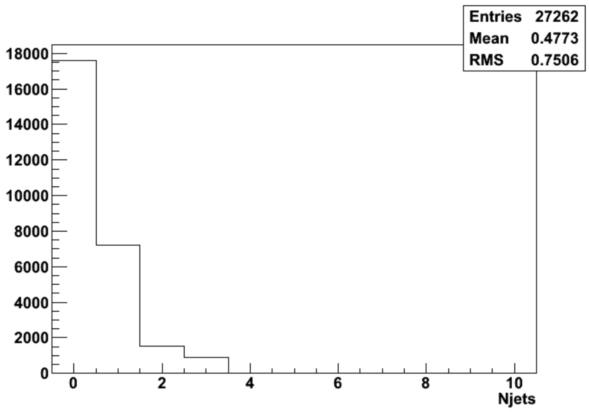

(e) Z/γ^* production with ISR/FSR and demand of $e^{\pm} + \mu^{\mp}$ with transverse momentum greater than 15GeV each

Figure 4.7: Number of inclusive 15 GeV jets found with Fastjet antiKt-algorithm for Z/γ. Numbers on y-axis are arbitrary.

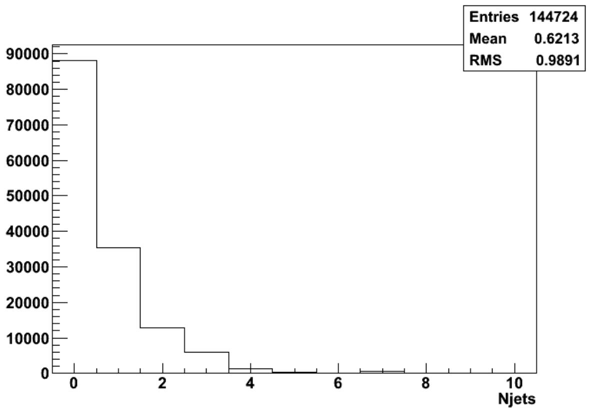

(a) Z production with ISR/FSR with demand of $e^{\pm} + \mu^{\mp}$ with transverse momentum above 15GeV each

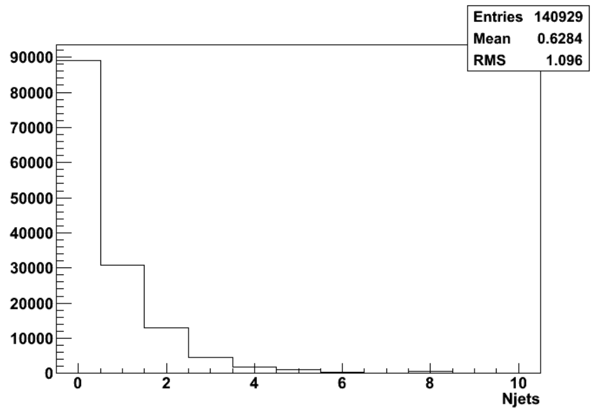

(b) Z production with ISR/FSR and additional partons with demand of $e^{\pm} + \mu^{\mp}$ with transverse momentum above 15GeV each

Figure 4.8: Number of inclusive 15 GeV jets found with Fastjet antiKt-algorithm for Z/γ. Numbers on y-axis are arbitrary.

Chapter 5

Generation of probability distribution functions

5.1 The probability shapes for the signal and background processes

The study considered in this thesis relies on the idea, that probability distributions for the different processes in a 2-D space of number of jets vs $\not{E}_T$ can be used to fit data with better statistical uncertainties then a purely exclusive analysis. To generate the probability distributions Monte Carlo generators have been used, but albeit Pythia does a fine job, making the distributions as precise as possible is important. The specialised generators and programs described in Section 3.3 have therefore been used. Equally important, the events generated must be comparable to the data collected in 2010. The ATLAS experiment uses a set of predefined structures for storing real data and simulated events. For this analysis official Analysis Object Data, AOD's have been used for all datasets. Furthermore the software releases for reconstruction and reprocessing of events are subject to constant development in ATLAS and care has been taken, that these agree between data and Monte Carlo. The datasets used are listed in appendix A.1.

5.2 Reconstruction and selection

After running the Monte Carlo generator and creating a specific process, particles from collisions go through the ATLAS detector simulation. Their response needs to be simulated, to have a realistic expectation of how data will look like. This is done in the Athena framework and reconstruction of different particles vary significantly. The processes we are interested in contain an electron and a muon of opposite charge and therefore need to have both a reconstructed electron and a reconstructed muon. Furthermore to suppress background, the tightness of the reconstruction needs to be rather high. By tightness we refer to how strict the demands are on variables from different detector parts to accept the given particle as an electron or a muon.

At the time of writing the lowest energy trigger thresholds without any prescales are ~15 GeV for muon and electrons. For this reason demanding leptons with any lower value does not make sense. The studies of the Pythia generated signal processes in the previous chapter encourages this value. Setting the cut too high will impact the amount of signal we get, so the lowest reasonable value for the moment, is with minimum P_T of 15 GeV for each lepton. This value has been chosen for the study.

5.2.1 Electron reconstruction

As described in Section 3.13 the different parts of the detector can be used to reconstruct different particle properties. The electron is reconstructed from the trackers and the calorimeters. Different degrees of tightness are being used as default: Loose, Medium and Tight. The three degrees of tightness give different degrees of discrimination of the electron against background. The amount of parameters and parts of the detector used to identify the electrons vary with each degree of tightness. An overview of the different variables can be seen in Fig. 5.1 The Loose identification is based on calorimeter information and takes advantage of the most basic assumptions to reconstruct electrons. The Medium electron identification sets requirements on energy depositions in the first EM calorimeter layer. Furthermore hits are demanded in both the SCT and pixel detector. A Tight electron pose further track and vertex matching requirements and the TRT is included. The ratio of high-threshold hits to total hits is especially useful for separating electrons from pions. The efficiency and jet rejection for the different degrees of tightness are shown in Tab. 5.2. The efficiencies have been listed for both isolated electrons coming from Z decay to two electrons and non-isolated electrons from b and c quark decays.

5.2.2 Muon reconstruction

For the muon reconstruction the muon system is obviously used, but also the calorimeters and the inner detectors play a significant role. There are two muon reconstruction algorithms: Muid [47] and STACO [48]. Efficiencies for the two have been shown to be almost identical [49] with STACO scoring slightly higher. We have chosen STACO for our analysis as it is also currently the ATLAS default. The STACO algorithm combines an inner detector track with a muon spectrometer track using a statistical method. On top of that two other algorithms are used: Muonboy and Mutag [48]. Muonboy starts from hit information in the muon spectrometer and produces standalone segments and tracks, that are extrapolated to the interaction vertex. Mutag associates inner detector tracks with Muonboy segments. To clarify only inner detector tracks not combined in STACO will be used. The same counts for muon spectrometer only tracks, that have not been combined with an inner detector track in STACO. More specifically the principle of the STACO method is the statistical combination of two independent measurements by means of their covariance matrices. A χ^2 test is made to determine how good the matching is [48].

The tightness of the different reconstruction algorithms is shown in Tab. 5.1. It is important to mention, that a tight muon is returned true if a medium candidate is requested like a tight or medium muon is returned true if a loose candidate is requested. The efficiency of the muon reconstruction for both the STACO, Muonboy and Mutag are shown in Fig. 5.3

Tight selections for both electron and muon give the best discrimination against background and retain a large percentage of our signal events. For added statistics a medium tightness requirement can be considered, but this requires another way of discriminating electrons and muons in signal events from the background events. This is indeed what will be done with isolation which we return to later.

Type	Description	Variable name
	Loose cuts	
Acceptance of the detector Hadronic leakage	$\lvert\eta\rvert < 2.47$ Ratio of E_T in the first sampling of the hadronic calorimeter to E_T of the EM cluster	
Second layer of EM calorimeter.	Ratio in η of cell energies in 3×7 versus 7×7 cells. Ratio in ϕ of cell energies in 3×3 versus 3×7 cells. Lateral width of the shower.	R_η R_ϕ
	Medium cuts (includes loose cuts)	
First layer of EM calorimeter.	Difference between energy associated with the second largest energy deposit and energy associated with the minimal value between the first and second maxima. Second largest energy deposit normalised to the cluster energy. Total shower width. Shower width for three strips around maximum strip. Fraction of energy outside core of three central strips but within seven strips.	ΔE_s R_{max2} w_{stot} w_{s3} F_{side}
Track quality	Number of hits in the pixel detector (at least one). Number of hits in the pixels and SCT (at least nine). Transverse impact parameter ($<$1 mm).	
	Tight (isol) (includes medium cuts)	
Isolation	Ratio of transverse energy in a cone $\Delta R < 0.2$ to the total cluster transverse energy.	
Vertexing-layer	Number of hits in the vertexing-layer (at least one).	
Track matching	$\Delta\eta$ between the cluster and the track (< 0.005). $\Delta\phi$ between the cluster and the track (< 0.02). Ratio of the cluster energy to the track momentum.	 E/p
TRT	Total number of hits in the TRT. Ratio of the number of high-threshold hits to the total number of hits in the TRT.	
	Tight (TRT) (includes tight (isol) except for isolation)	
TRT	Same as TRT cuts above, but with tighter values corresponding to about 90% efficiency for isolated electrons.	

Figure 5.1: Demands for electron identification with the three degrees of tightness.

Cuts	**Cut-based method**	
	Efficiency ε_e (%)	Rejection R_j
Loose	87.97 ± 0.05	567 ± 1
Medium	77.29 ± 0.06	2184 ± 7
Tight (isol)	64.22 ± 0.07	$(9.9 \pm 0.2) \times 10^4$
Tight (TRT)	61.66 ± 0.07	$(8.9 \pm 0.2) \times 10^4$

Figure 5.2: The loose, medium and tight electron identification cuts for electrons with P_T above 17 GeV. The quoted errors are statistical [46].

Author	Quality Word
Staco candidate	Tight
MuTag candidate with at least 4 TGC Phi hits in tagging segments	Tight
MuTag candidate with at least 2 tagging segments	Tight
MuTag candidate with only 1 tagging segment in End cap region and no TGC Phi hits in tagging segment	Loose
MuTag candidate not belonging to the preceding categories	Medium
Muonboy candidate	Medium

Table 5.1: Tightness criteria of the muon reconstruction algorithms.

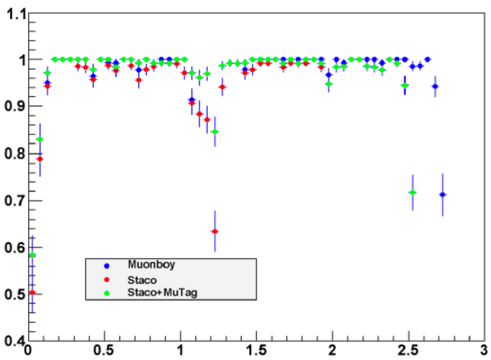

Figure 5.3: Efficiencies as function of $|\eta|$ from standalone and combined μ reconstruction algorithms, obtained on a single muon simulated sample of $P_T = 100$ GeV / c. [50]. The drops in efficiency is dropping stem from regions where the Muon Spectrometer coverage is thin.

5.2.3 Statistical consideration of the used samples

All the different processes relevant for this study have been listed in Tables 5.2 and 5.3. The scaling factor is here for simplicity listed to 1 pb^{-1} as we will be scaling to different integrated luminosities later. The listed luminosity gives a good idea of the statistics for a given process. A study of 10 pb^{-1} will have good statistics for all signal processes and acceptable statistics for most background samples. The QCD samples are however lacking in statistics and give poor shapes for studies with e.g. 10 pb^{-1} integrated luminosity of data where their scaling factor will be around one.

Table 5.2: Main processes

Process	Events generated	$\sigma_{gen} \cdot \epsilon_{filter}$ (pb)	K Factor	σ_{theory} (pb)	Int. lumi. (pb^{-1})	Scale factor to 10 pb^{-1}
$pp \to t\bar{t}$	199828	80.201	1.11	$164.57^{+11.8}_{-16.02}$	2245	0.0045
$pp \to t\bar{t}$ AcerMC	199891	58.23	1.53	$164.57^{+11.8}_{-16.02}$	2244	0.0045
$pp \to W^+W^-$	249837	11.75	1.52	44.9 ± 2.2	13989	0.00073
$pp \to Z \to \tau\tau$	303359	657.4	1.22	969 ± 48 (tot)	378	0.026
$pp \to Z \to \tau\tau$ + 1 parton	63481	133.0	1.22	-	391	0.026
$pp \to Z \to \tau\tau$ + 2 parton	19492	40.4	1.22	-	396	0.025
$pp \to Z \to \tau\tau$ + 3 parton	5497	11.0	1.22	-	410	0.024
$pp \to Z \to \tau\tau$ + 4 parton	1499	2.9	1.22	-	424	0.024
$pp \to Z \to \tau\tau$ + 5 parton	499	0.7	1.22	-	584	0.017

The luminosity should be viewed bearing in mind, that generation filters have been applied. For all listed QCD samples a filter demanding one muon with P_T above 10 GeV has been applied. The cross sections include filter efficiencies except for $W\mu^+ + \gamma$ and $W\mu^- + \gamma$ where cross sections are taken from the ATLAS Metadata Interface, AMI [51] and have been corrected for filter efficiencies.

The K-factor is a scaling factor introduced to correct the production cross section for various processes. It is basically a correction corresponding to the discrepancy between the cross section from the used Monte Carlo generator and higher order theoretical calculations. The K-factor for all Alpgen samples was calculated by taking the ratio between the cross section estimated by Alpgen and a NNLO theoretical calculation at 14 TeV centre-of-mass energy. Reevaluating the K-factor for a centre-of-mass energy of 7 TeV would likely reveal a different value, but the theoretical calculations have not been performed for this value yet. The correction is thought to be needed and be of the order of that calculated for 14 TeV.

The theoretical cross sections for $Z \to \tau\tau$ and WW are from [52] and the $t\bar{t}$ is from [53] for a top mass of 172.5 GeV.

5.2.4 Number of jets

To make sure we understand the number of jets distribution in the official ATLAS samples used (see Section 5.2), we compare it to what we observed for this variable in our own privately produced MC sample (Section 3.3). The comparison has been done for the $Z\tau\tau$ process. To clarify the Fastjet AntiKt algorithm, used in the private MC production, gets its input from

Table 5.3: Background processes

Process	Events generated	$\sigma_{gen} \cdot \epsilon_{filter}$ (pb)	K Factor	Luminosity (pb^{-1})	Scale factor to 1 pb^{-1}
$pp \rightarrow We\nu$ + 0 partons	1381931	6913.3	1.22	163.84	0.0061
$pp \rightarrow We\nu$ + 1 parton	258408	1293.0	1.22	163.81	0.0061
$pp \rightarrow We\nu$ + 2 partons	188896	377.1	1.22	410.88	0.0024
$pp \rightarrow We\nu$ + 3 partons	50477	100.9	1.22	410.06	0.0024
$pp \rightarrow We\nu$ + 4 partons	12991	25.3	1.22	420.88	0.0023
$pp \rightarrow We\nu$ + 4 partons	3450	6.9	1.22	409.8	0.0024
$pp \rightarrow W\mu\nu$ + 1 parton	255909	1281.2	1.22	163.72	0.0061
$pp \rightarrow W\tau\nu$ + 1 parton	254753	1276.8	1.22	163.54	0.0061
$pp \rightarrow Wbb$ + 0 partons	6499	3.2	1.22	1665	0.00060
$pp \rightarrow WZ$	249830	3.432	1.58	46072	$2.2 \cdot 10^{-5}$
$pp \rightarrow ZZ$	249725	0.977	1.20	213003	$4.7 \cdot 10^{-6}$
$pp \rightarrow W\mu^+ + \gamma$	50000	$28.0266 \cdot 10^{-3}$	1.22	1462.3	$6.8 \cdot 10^{-4}$
$pp \rightarrow W\mu^- + \gamma$	49992	$28.0266 \cdot 10^{-3}$	1.22	1462.3	$6.8 \cdot 10^{-4}$
$pp \rightarrow Z \rightarrow ee$ + 0 partons	304216	661.9	1.22	376.73	0.00265
$pp \rightarrow Z \rightarrow ee$ + 2 partons	19497	40.3	1.22	396.55	0.00207
$pp \rightarrow Z \rightarrow \mu\mu$ + 0 partons	303947	657.7	1.22	462.14	0.00216
$pp \rightarrow Z \rightarrow \mu\mu$ + 2 partons	18993	39.6	1.22	479.62	0.0025
$pp \rightarrow$single top tchan $\rightarrow e$	9993	7.152	1	1397	0.0007
$pp \rightarrow$single top tchan $\rightarrow \mu$	9997	7.176	1	1393	0.0007
$pp \rightarrow$single top tchan $\rightarrow \tau$	10000	7.128	1	1402.9	0.00071
$pp \rightarrow$single top Wt $\rightarrow$ inclusive	14995	14.581	1	1028.4	0.00097
$pp \rightarrow$QCD J1 + 2 partons	279895	28343	-	9.875	0.1013
$pp \rightarrow$QCD J1 + 3 partons	10497	1008	-	10.410	0.0960
$pp \rightarrow$QCD J2 + 2 partons	279895	46379.6	-	6.0350	0.1660
$pp \rightarrow$QCD J2 + 3 partons	86425	10660.9	-	8.1070	0.1230
$pp \rightarrow$QCD J2 + 4 partons	12500	1248.9	-	10.009	0.0999
$pp \rightarrow$QCD J2 + 5 partons	1500	148.4	-	10.11	0.0989
$pp \rightarrow$QCD J2 + 6 partons	500	424	-	11.79	0.0848
$pp \rightarrow$QCD J3 + 2 partons	29988	3004.2	-	9.9820	0.100
$pp \rightarrow$QCD J3 + 3 partons	37483	3709.0	-	10.106	0.0990
$pp \rightarrow$QCD J3 + 4 partons	12491	1224.9	-	10.198	0.0981
$pp \rightarrow$QCD J3 + 5 partons	3997	359.1	-	11.13	0.0898
$pp \rightarrow$QCD J3 + 6 partons	498	73.1	-	6.81	0.147
$pp \rightarrow$QCDbb J2 + 0 partons	50981	5071.0	-	10.053	0.0994
$pp \rightarrow$QCDbb J2 + 1 parton	40441	4009.5	-	10.086	0.0991
$pp \rightarrow$QCDbb J2 + 2 partons	11498	1105.9	-	10.397	0.0962
$pp \rightarrow$QCDbb J2 + 3 partons	2499	230.6	-	10.84	0.0923
$pp \rightarrow$QCDbb J2 + 4 partons	500	43.4	-	11.5	0.087
$pp \rightarrow$QCDbb J3 + 0 partons	4000	384.5	-	10.40	0.0961
$pp \rightarrow$QCDbb J3 + 1 parton	11996	1162.3	-	10.321	0.0969
$pp \rightarrow$QCDbb J3 + 2 partons	6999	658.6	-	10.627	0.0941
$pp \rightarrow$QCDbb J3 + 3 partons	2498	231.1	-	10.81	0.0925
$pp \rightarrow$QCDbb J3 + 4 partons	1000	86.6	-	11.55	0.0866

the tracks generated in the event. The AntiKtTopo algorithm in the ATLAS sample works on the fully simulated event and reconstructs jets using topological clusters, as explained earlier.

The comparison can be seen in Figures 5.4a and 5.4b respectively. Both figures have been scaled to 10 pb^{-1}. The reconstructed jets in Fig. 5.4b have been reconstructed from topological clusters of energy while the fastjet AntiKt algorithm in Fig. 5.4a is based on particle track inputs directly from Pythia without detector simulation. To compare the two jet algorithms directly we give them the same input. This is done by letting the AntiKt algorithm work on the MC truth tracks that are stored in the ATLAS $Z \to \tau\tau$ sample. Comparing to Fig. 5.4e where the reconstructed AntiKt is indeed done on particles from the truth container in the ATLAS sample, the resemblance is very good.

Additional algorithms like the seeded cone, and different calorimeter inputs like calorimeter towers have been looked at. The results are plotted in Figures 5.4c and 5.4d at reconstruction level and in Figures 5.4e and 5.4f at truth level. The AntiKtTopo has been chosen as it is recommended officially for ATLAS 2010 data. [42]

5.3 Missing transverse momentum

The second parameter used in our study is missing transverse energy, $\not{E}_T$. Naively, in the Standard Model, $\not{E}_T$ stems only from neutrinos as these will not be detected by any part of ATLAS. In reality other sources contribute to the lack of balance in total transverse momentum measured in the detector and should be taken into account and corrected for. For example, the ATLAS cryostat - the container that hold the liquid argon needed for the EM calorimeters - causes a loss of energy that should be corrected for when reconstructing $\not{E}_T$. E_T is calculated as the total transverse energy from the energy deposited in the EM calorimeters as well as from the muon detectors. The $\not{E}_T$ is the energy imbalance between the E_T and the total transverse energy of the colliding particles. After calculations of the transverse energy, the resulting value can be calibrated to get a more reliable number. Calibration of the energy can be done in different ways, the main difference being whether the EM cells are calibrated locally or globally. An overview of the calculation and calibration process can be seen in Fig. 5.6. The reconstruction methods used are the topologically weighted (topo) and geometrically weighted (H1) discussed in Section 4.3. The default type for reconstructed $\not{E}_T$ is called the refined calibrated $\not{E}_T$. When constructing it, calorimeter cell readouts are associated with a parent object - a reconstructed, identified high-P_T object - in a chosen order: electrons, photons, muons, hadronically decaying tau-leptons, b-jets and light jets. A refined calibration of these objects is then used instead of the initial global calibration of cells allowing for a more accurate calibration and thus a better $\not{E}_T$ reconstruction. This refined $\not{E}_T$ thus contains the sum of $\not{E}_T$ calculated from both interacting particles as well as muons that will generally not interact significantly in the EM calorimeters. The calibrated $\not{E}_T$ should optimally correspond directly to the energy being carried away by non-interacting particles like neutrinos or supersymmetric particles. The true $\not{E}_T$ is calculated both from interacting particles and in $|\eta| \leq 5$ including muons. For comparison the $\not{E}_T$ reconstructed directly from the topological clusters have also been included.

The important question to answer is if the missing energy reconstruction with the refined calibrated method described earlier compares to the true missing energy and how the alternative topologically based method performs relatively.

In Figures 5.7a, 5.7b and 5.7c the $\not{E}_T$ variables have been plotted for events with recon-

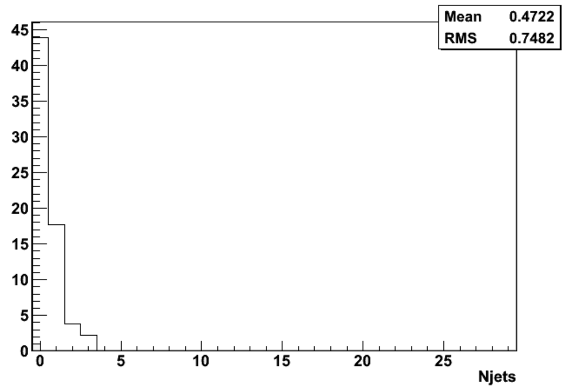

(a) Fastjet AntiKt jet reconstruction of Pythia $Z\tau\tau \to e\mu$ in 10 pb^{-1}

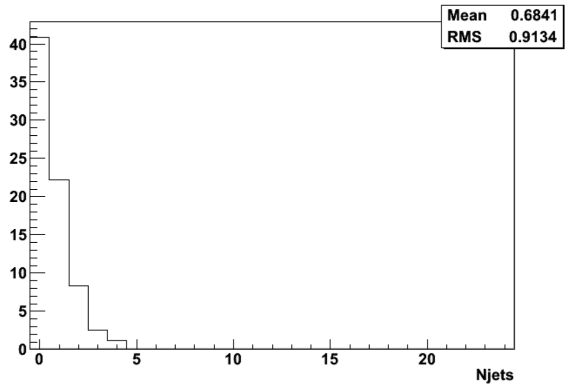

(b) AntiKtTopo jet reconstruction on Pythia $Z\tau\tau \to e\mu$ in 10 pb^{-1}

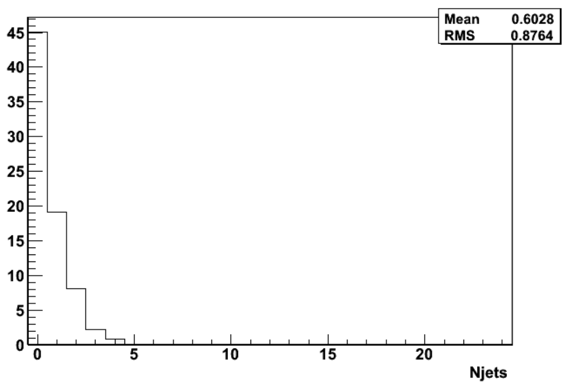

(c) AntiKtTower jet reconstruction on Pythia $Z\tau\tau \to e\mu$ in 10 pb^{-1}

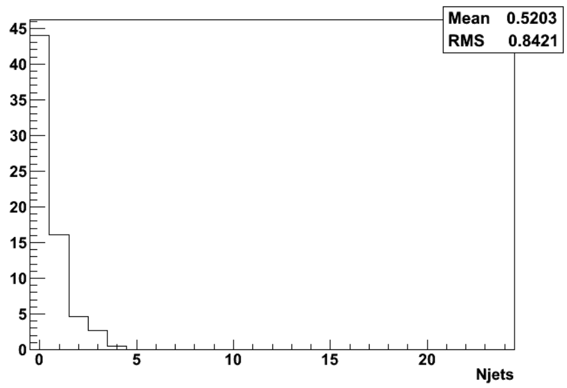

(d) Cone4Tower jet reconstruction on Pythia $Z\tau\tau \to e\mu$ in 10 pb^{-1}

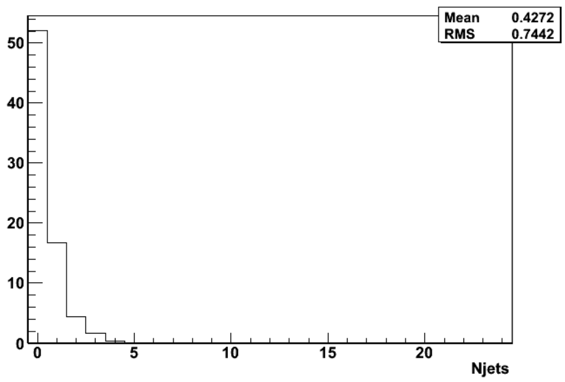

(e) AntiKttruth reconstruction on Pythia $Z\tau\tau \to e\mu$ in 10 pb^{-1}

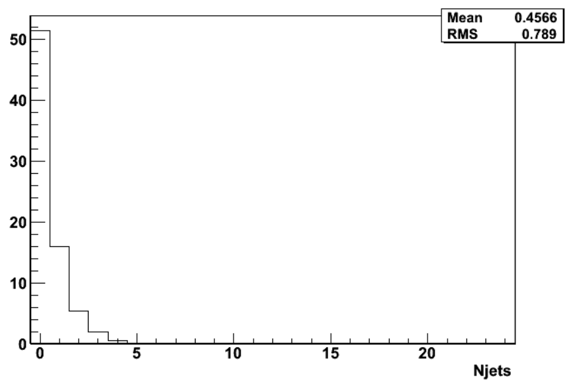

(f) Cone4Truth jet reconstruction on Pythia $Z\tau\tau \to e\mu$ in 10 pb^{-1}

Figure 5.4: Comparison of the performance of the different jet algorithms. The figures are scaled to an integrated luminosity of 10 pb^{-1}.

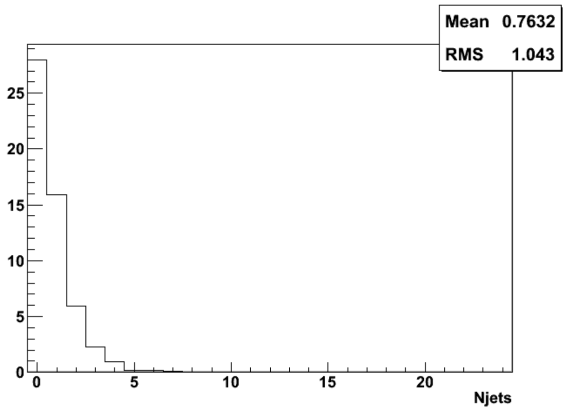

Figure 5.5: AntiKttruth jet reconstruction from the Alpgen + Njets $Z \to \tau\tau \to e\mu$ sample.

structed e and μ. The refined calibrated reconstruction of the $\not{E}_T$ agrees well with the true $\not{E}_T$ while the topologically reconstruction $\not{E}_T$ is shifted significantly towards higher $\not{E}_T$. For the rest of the study missing transverse momentum (MET in figures) will be referring to refined calibrated $\not{E}_T$.

5.4 Lepton isolation

If the reconstructed electrons and muons originate from heavy quark decays in jets, rather than from Z or W decays, particles in a small cone around the lepton should also include mother particles, including these heavy quarks with momentum above 15 GeV. If additionally the reconstructed leptons are in reality pions or other particles faking leptons, these must also have energies of ∼15 GeV and must be found around the reconstructed lepton. We study this in the Monte Carlo samples, where the truth particles around the origin of the reconstructed electrons and muons can be traced.

Figure 5.8 shows the truth particles within a cone of radius $\Delta R = \sqrt{\delta\phi^2 + \delta\eta^2} \leq 0.2$ of leptons reconstructed with tight demands. The Particle Data Group [39] particle codes are plotted on the axis. The particles have all had the demand of having P_T above 10 GeV. It is important to emphasise, that here can (and will) be many more low energy particles from the decays of the heavy quark mother particles for backgrounds and the underlying event in general. These plots, with only particles above 10 GeV, however show us the contributions fromthe contributions from leptons from heavier quarks, conversions or even pions that could fake leptons.

As can be seen in Figures 5.8a and 5.8b electrons or muons from $Z \to \tau\tau$ are well isolated from particles with P_T above 10 GeV, with only a few pions sneaking in through the selection. The electron channel is equally well isolated for the WW process while the muon channel for WW has some additional quarks and mesons.

In Fig. 5.8e the top decays are shown for the electrons channel. The picture here changes and both $\pi's$, $\rho's$ and mesons are present within the demanded radius. This is not surprising as the top decays to an electron through $t \to e + \nu_e + b$. The decay and further hadronisation of the b-quark is likely to be responsible for the particles of this type, that we see. The electrons are still rather well isolated. For Fig. 5.8f the isolation of the muon channel is shown. The same particles, as for the electron channel, are seen in greater numbers and there is the addition of pions and kaons indicating a worse isolation of the muon. Finally Figures 5.8g and 5.8h show the Alpgen QCD dijet samples filtered for b anti-b quark production, from gluon splitting, simulated with up to 5 partons in the final state. The $b\bar{b}$ sample has been selected as it is the dominating background without isolation requirements. As is seen, both the electron and muon channels are poorly isolated. The process is greater than any single signal process and concentrated in the same region as the $Z \to \tau\tau$ signal making them indistinguishable. The suppression provided by requiring isolation, or equally the lack of activity around the high P_T electron or muon, must however keep as much of our signal processes as possible. It seems from Fig. 5.8 that $t\bar{t}$ limits the isolation on muons as this would also cut away a significant amount of the signal, while an isolation cut on the electron might leave most of the signal while sorting away the $b\bar{b}$ background and to some extent the other backgrounds.

Muon isolation

Let us revisit the leptons reconstruction and identification and consider the possible ways of imposing isolation criteria on the leptons. Muon isolation can be separated into two types: calorimeter-based and track-based. The calorimeter isolation is determined from reconstruction by defining a cone around the muon trajectory with a minimum and maximum radius so cells, where the muon deposits its energy, can be excluded. The size of the inner radius must be optimised to collect most of the energy deposited by the muon and as little as possible from other particles. The energy deposited between the inner and outer radius is then the isolation energy. The isolation energy can be effective to cut upon, as muons from different processes have very different degrees of isolation.

This is seen in Fig. 5.9 (left) from [49]. Here the isolation energy of the decay of $t\bar{t}$ to a muon and a neutrino through the W channel and semileptonic to a muon through a b-quark is shown for the electromagnetic and hadronic calorimeter. The figure shows that the muon from W decay is well isolated whereas the muon from b decay is poorly isolated. The effect is seen in the hadronic calorimeter but is more pronounced in the EM calorimeter. The picture changes slightly with increasing muon P_T and isolation cuts should be set a bit higher to account for a possible increase in the energy deposited in the calorimeter caused by increasing P_T of the muon.

Track-based isolation can also be used either together with or as an alternative to calorimeter based isolation as the two are independent.

Figure 5.10 from [49] shows the distribution of number of tracks (including the muon track) with $\Delta R < 0.2$ around the muon spectrometer track for the same $t\bar{t}$ sample as in Fig. 5.9. There has been applied a 2 GeV isolation cut on EM calorimeter and a P_T threshold cut on the muon of 15 GeV. The last cut is to sort away low-P_T muons from quarks etc. and keep muons from Z and W decays, as these have a P_T around 40 GeV on average. [49] It is seen, that the most probable value of number of tracks, for a muon originating from a b-quark, is three while the probability of a muon from a W having more than two tracks is low. By default in the Muid muon reconstruction algorithm the two above cuts have been implemented along with a cut demanding at most one accompanying track inside the tracking cone of $\Delta R < 0.2$. This is not the case of STACO where a track optimisation can, based on what is seen in Fig. 5.10, be done by demanding a maximum of two tracks in a cone of $\Delta R < 0.2$. The energy isolation criteria could also be optimised possibly by dividing the isolation energy with the track momentum as this would take into account the fact, that the muon isolation energy increases with increasing muon P_T. The distributions of number of tracks are seen in Fig. 5.11. Here the number of tracks (excluding the muon track) within a cone of radius ΔR is counted for the muons coming from taus (Z) and W's. It is clearly seen that the distribution for all processes are as expected from Fig. 5.10

Electron isolation

The isolation of the electron is based both on the calorimeter and tracks but tighter demands on number of hits in TRT and ratio of high-threshold to normal hits can also be used to isolate against pions. The isolation criteria described in Fig. 5.1 are no longer up to date. In fact the notion of default isolation for the electron has given way to isolation parameters based on the relevant analysis. The electron is different from the muon as it emit bremsstrahlung directly translated as "brake radiation" or deceleration radiation. Any charged particle being accelerated or decelerated will emit radiation. For the electron the radiation is emitted, as it is being stopped by the material in the detector which decelerates it. Due to their much higher mass, muons are not stopped to the same degree and therefore do not radiate of energy like the electrons. This means, that the electrons will not have a track as clearly defined as the muon. They can however still be isolated based on some of the same variables as the muon.

To determine which variable would be the best to cut on for each lepton, different variables have been tested.

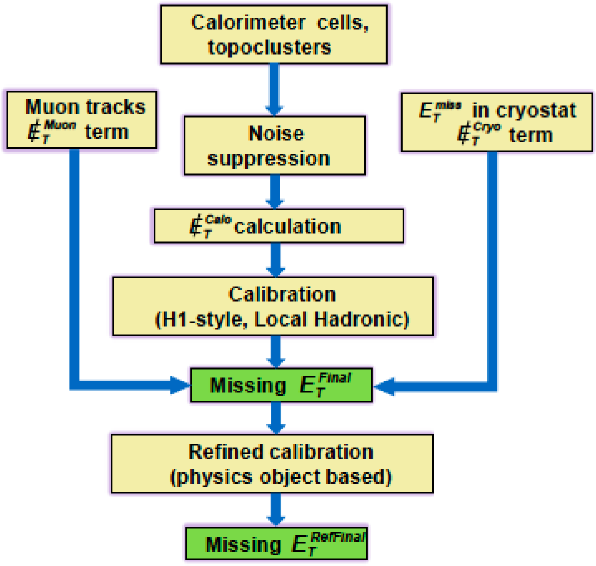

Figure 5.6: The different steps of $\not{E}_T$ calculations and the following calibration

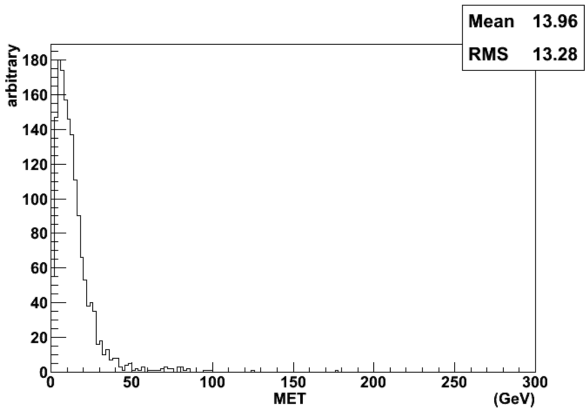

(a) Pythia $Z\tau\tau \to e\mu$ refined calibrated $\not{E}_T$

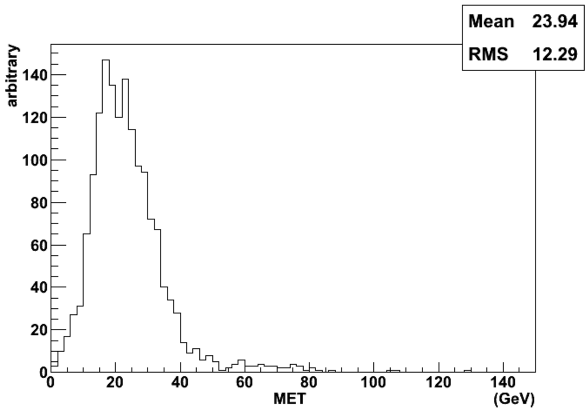

(b) Pythia $Z\tau\tau \to e\mu$ topological $\not{E}_T$

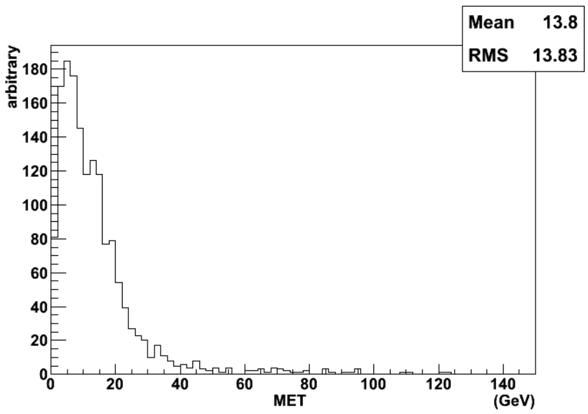

(c) Pythia $Z\tau\tau \to e\mu$ true $\not{E}_T$

Figure 5.7: Missing transverse momentum reconstructed from different containers.

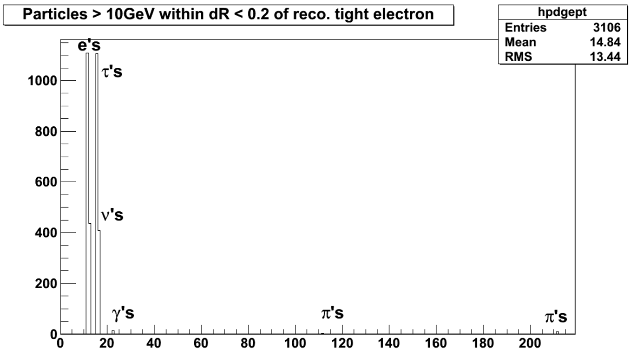

(a) Number of particles of different type in Pythia $Z\tau\tau \rightarrow e\mu$ for electron reconstructed with tight demand

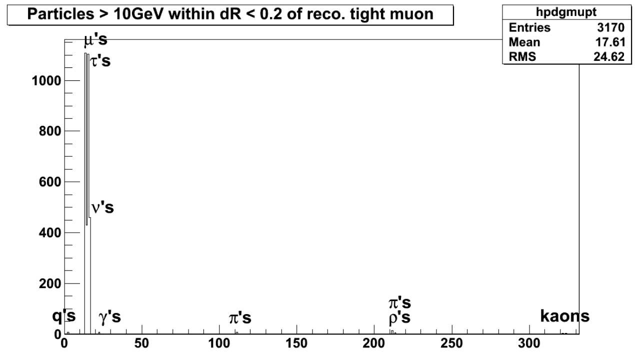

(b) Number of particles of different type in Pythia $Z\tau\tau \rightarrow e\mu$ for muon reconstructed with tight demand

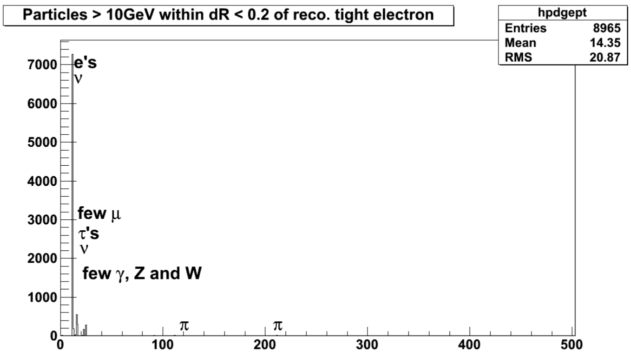

(c) Number of particles of different type in Herwig $WW \rightarrow e\mu$ for electron reconstructed with tight demand

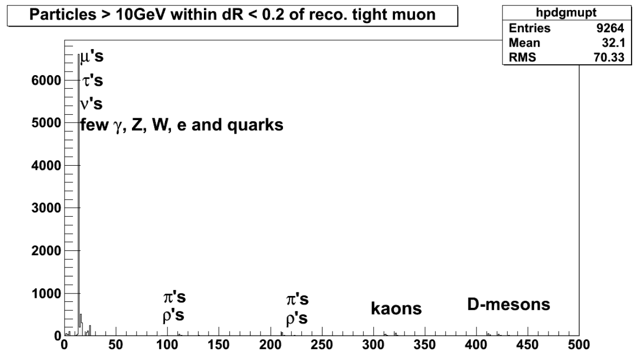

(d) Number of particles of different type in Herwig $WW \rightarrow e\mu$ for muon reconstructed with tight demand

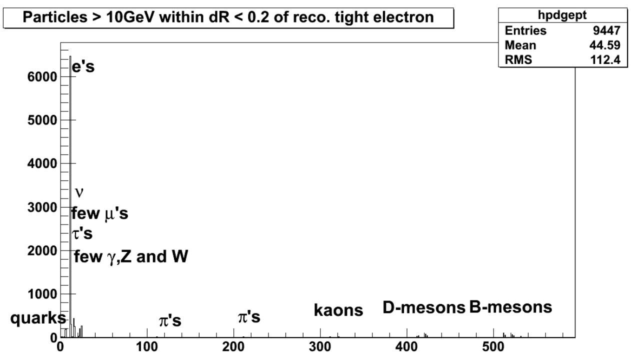

(e) Number of particles of different type in MC@NLO $t\bar{t} \rightarrow e\mu$ for electron reconstructed with tight demand

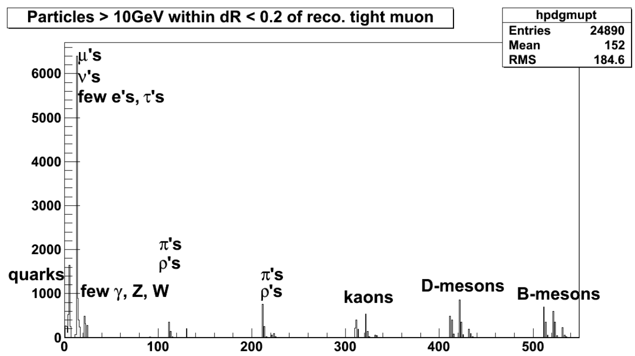

(f) Number of particles of different type in MC@NLO $t\bar{t} \rightarrow e\mu$ for muon reconstructed with tight demand

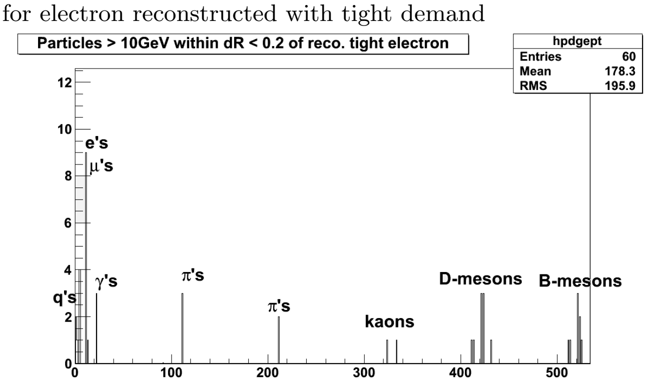

(g) Number of particles of different type in Alpgen QCD$b\bar{b}j2 \leq$ 4 partons for electron reconstructed with tight demand

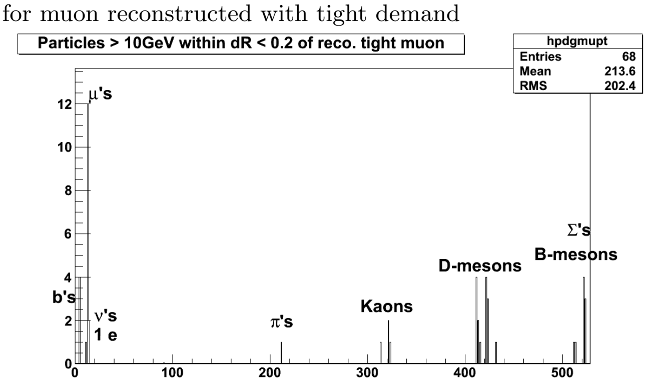

(h) Number of particles of different type in Alpgen QCD$b\bar{b}j2 \leq$ 4 partons for muon reconstructed with tight demand

Figure 5.8: Particles with P_T above 10GeV in a cone of ΔR=0.2 around reconstructed electrons and muons in events reconstructed with a tight electron and tight muon of opposite charge, both with P_T above 15 GeV.

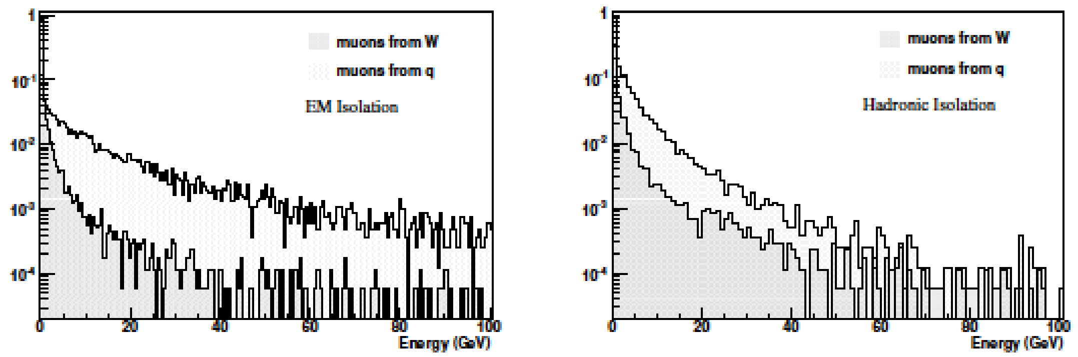

Figure 5.9: Muon isolation energy from EM calorimeter and isolation energy from hadronic calorimeter normalised to first bin.

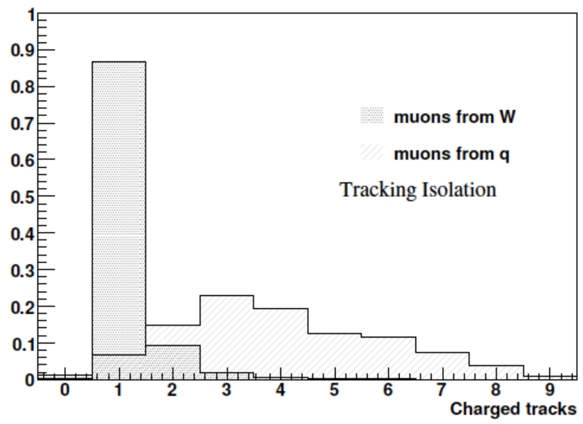

Figure 5.10: Distribution of number of tracks (including the muon track) with $\Delta R < 0.2$ around the muon spectrometer track for $t\bar{t}$ with 2 GeV calo. cut and muon P_T threshold cut of minimum 15 GeV.

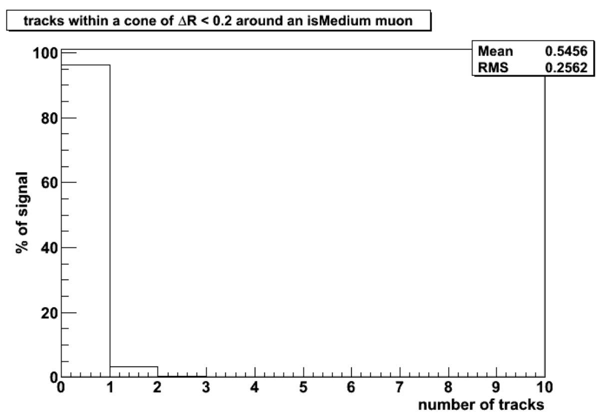

(a) Number of tracks within a cone $\Delta R < 0.2$ around the cone of a medium muon from $Z \rightarrow \tau\tau$

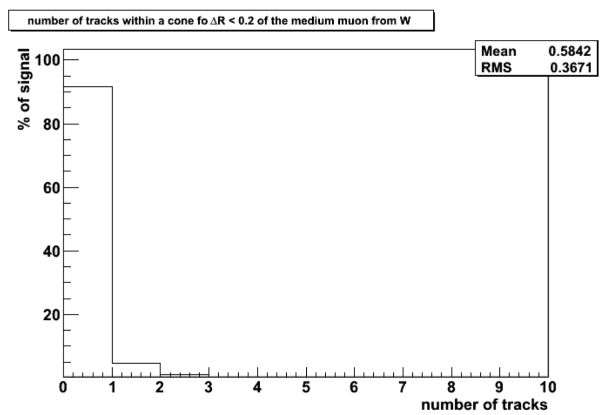

(b) number of tracks within a cone $\Delta R < 0.2$ around the cone of a medium muon from W

Figure 5.11: Number of tracks for WW and Z.

Isolation variables

The E_T measured in the electromagnetic calorimeter within a cone around the lepton (ΣE_T) can be used as a standalone parameter. This variable is often referred to as the isolation energy. It can be based on energy measurements or the sum of P_T from all tracks within the given cone. This variable has been tested in both forms. The relative isolation energy, where the isolation energy is divided by total combined lepton P_T, has also been studied. The relative variable allows for a cut yielding even better isolation. It is given by:

$$\frac{\Sigma E_T}{P_T} < \text{cut} \tag{5.1}$$

As the actual value in the cone is the assumed energy of the lepton subtracted the value of other particles in the cone, the value of ΣE_T can be negative for muons. The isolation energy has, for the relative variable, also been calculated with the P_T of the tracks within a cone divided by the P_T of the lepton. Finally the inverted variables and inverted relative variables have been tested. The inverted variables are calculated as

$$\frac{1}{1 + (\Sigma E_T)} < \text{cut} \tag{5.2}$$

and the inverted relative as

$$\frac{1}{1 + \left(\frac{\Sigma E_T}{P_T}\right)} < \text{cut} \tag{5.3}$$

The number of tracks around the reconstructed lepton was also used as a isolation variable for the muon.

Figure 5.12 shows the muon signal over square root background distributions for cuts on a few of the isolation variables. Many further have been tested. The distributions are based on medium tight muons but the shapes are similar for tight muons. As we need our cuts to have a minimum impact on our signal, we demand that 90% of the total $t\bar{t}$ signal pass the cuts and optimise the cuts based on that. The $t\bar{t}$ distribution was selected, as this is the most delicate with regard to isolation i.e. electrons and muons from both $Z \to \tau\tau$ and WW are better isolated. The 90% value is indicated by the red line. If a higher signal to background ratio is allowed for a looser isolation with more than 90% passing, the cut is indicated with a blue line. For the muon we find, that the optimal cut is $\frac{E_T^{isol}}{P_T} = 0.05$ within a cone $\Delta R = 0.3$.

For the electron in Fig. 5.13 it is seen, that the isolation energy is much higher than for the muon. This is not surprising as the electron emits bremstrahlung. The cut choice is more difficult as the optimal signal over background lie very close. We have chosen $\frac{E_T^{isol}}{P_T} = 0.08$ within a cone $\Delta R = 0.2$.

This results in 89% of the signal passing the cut while 4% of the QCD background passes for the muon and 88% of the signal for the electron with only 13% of the QCD events passing.

In Tab. 5.4 the number of events passing different selection tightness and isolation demands have been summarised for all signal processes and for the largest QCD background. As expected, it is clear that isolation demands on either the electron or muon drastically reduce the number of QCD events passing selection. Also cutting on both leptons sort away more background then simply cutting on one of the leptons. The effect of the tightness is however also seen, and a significantly larger amount of signal is passing with medium, isolated demands on both leptons compared to tight, isolated leptons. For further studies both the

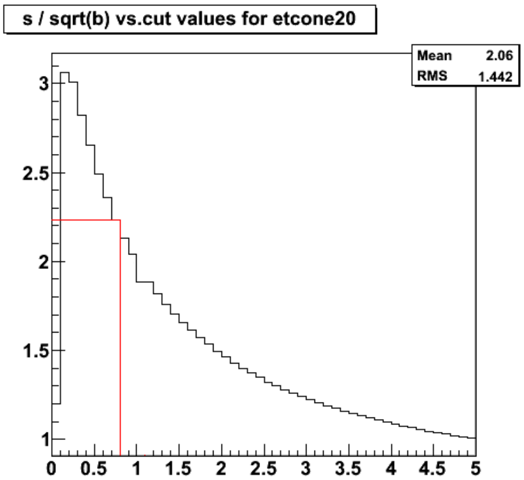

(a) $\frac{t\bar{t}}{\sqrt{QCD}}$ for E_T^{isol} in a cone $\Delta R < 0.2$

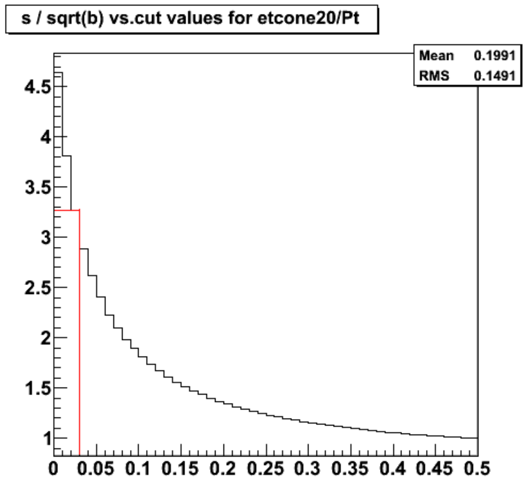

(b) $\frac{t\bar{t}}{\sqrt{QCD}}$ for $\frac{E_T^{isol}}{P_T}$ in a cone $\Delta R < 0.2$

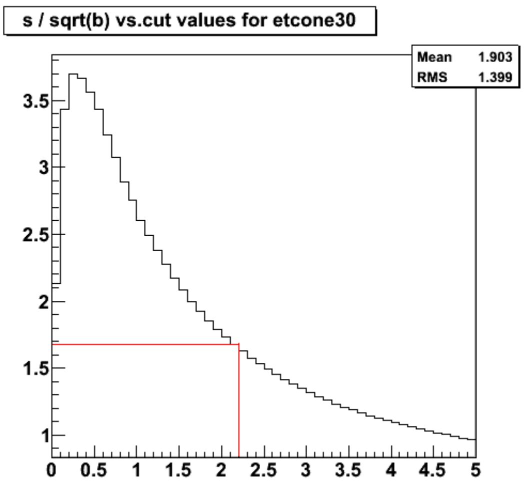

(c) $\frac{t\bar{t}}{\sqrt{QCD}}$ for E_T^{isol} in a cone $\Delta R < 0.3$

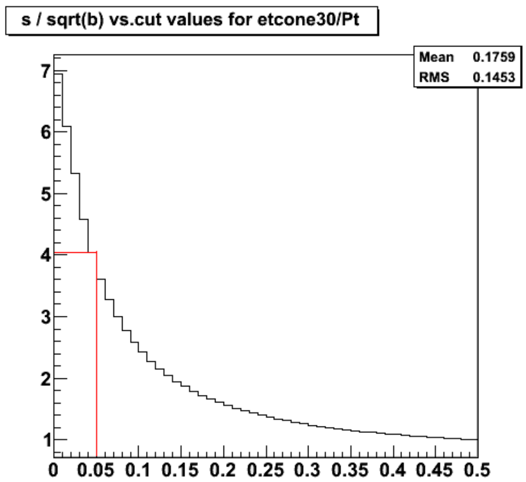

(d) $\frac{t\bar{t}}{\sqrt{QCD}}$ for $\frac{E_T^{isol}}{P_T}$ in a cone $\Delta R < 0.3$

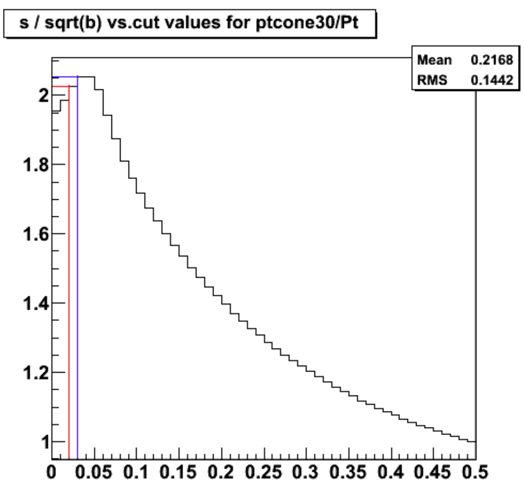

(e) $\frac{t\bar{t}}{\sqrt{QCD}}$ for $\frac{P_T^{track}}{P_T}$ in a cone $\Delta R < 0.3$

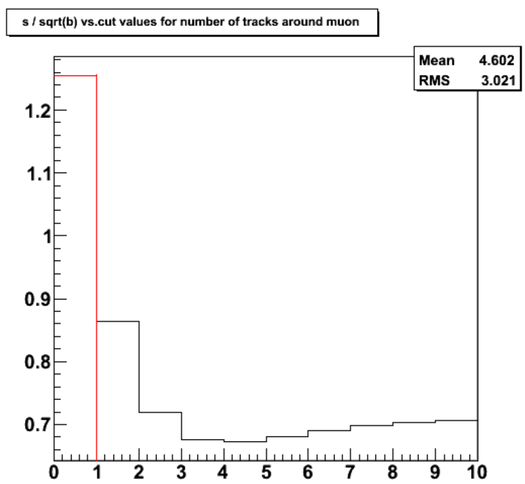

(f) $\frac{t\bar{t}}{\sqrt{QCD}}$ for total number of tracks in a cone $\Delta R < 0.2$

Figure 5.12: Isolation parameter and ratio of signal passing those cuts for a muon reconstructed with a medium tightness

Process	electron tightness	muon tightness	# Events
$t\bar{t}$	tight	tight	6500
$t\bar{t}$	medium, isolated	tight	7067
$t\bar{t}$	tight, isolated	tight	5781
$t\bar{t}$	tight	medium, isolated	6043
$t\bar{t}$	tight	tight, isolated	4645
$t\bar{t}$	medium, isolated	medium, isolated	5172
$t\bar{t}$	tight, isolated	tight, isolated	4131
$t\bar{t}$ AcerMC	tight	tight	6500
$t\bar{t}$ AcerMC	medium, isolated	tight	6990
$t\bar{t}$ AcerMC	tight, isolated	tight	5758
$t\bar{t}$ AcerMC	tight	medium, isolated	5673
$t\bar{t}$ AcerMC	tight	tight, isolated	4395
$t\bar{t}$ AcerMC	medium, isolated	medium, isolated	4810
$t\bar{t}$ AcerMC	tight, isolated	tight, isolated	3855
WW	tight	tight	7599
WW	medium, isolated	tight	8738
WW	tight, isolated	tight	6964
WW	tight	medium, isolated	9271
WW	tight	tight, isolated	7004
WW	medium, isolated	medium, isolated	8205
WW	tight, isolated	tight, isolated	6432
$Z \to \tau\tau \leq$ 5partons	tight	tight	1120
$Z \to \tau\tau \leq$ 5partons	medium, isolated	tight	1275
$Z \to \tau\tau \leq$ 5partons	tight, isolated	tight	956
$Z \to \tau\tau \leq$ 5partons	tight	medium, isolated	1292
$Z \to \tau\tau \leq$ 5partons	tight	tight, isolated	1045
$Z \to \tau\tau \leq$ 5partons	medium, isolated	medium, isolated	1203
$Z \to \tau\tau \leq$ 5partons	tight, isolated	tight, isolated	888
QCDbbj2 $\leq$ 5partons	tight	tight	89
QCDbbj2 $\leq$ 5partons	medium, isolated	tight	13
QCDbbj2 $\leq$ 5partons	tight, isolated	tight	8
QCDbbj2 $\leq$ 5partons	tight	medium, isolated	11
QCDbbj2 $\leq$ 5partons	tight	tight, isolated	7
QCDbbj2 $\leq$ 5partons	medium, isolated	medium, isolated	0
QCDbbj2 $\leq$ 5partons	tight, isolated	tight, isolated	0
QCDj2 $\leq$ 5partons	tight	tight	12
QCDj2 $\leq$ 5partons	medium, isolated	tight	17
QCDj2 $\leq$ 5partons	tight, isolated	tight	3
QCDj2 $\leq$ 5partons	tight	medium, isolated	5
QCDj2 $\leq$ 5partons	tight	tight, isolated	3
QCDj2 $\leq$ 5partons	medium, isolated	medium, isolated	3
QCDj2 $\leq$ 5partons	tight, isolated	tight, isolated	2

Table 5.4: Different selection requirements and their impact on number of final $e\mu$ events from different processes. Number of events before selection can be seen in Tables 5.2 and 5.3

medium and tight, isolated demands have been applied for both leptons. This gives us two scenarios; one with more statistical power, and one with maximum background rejection.

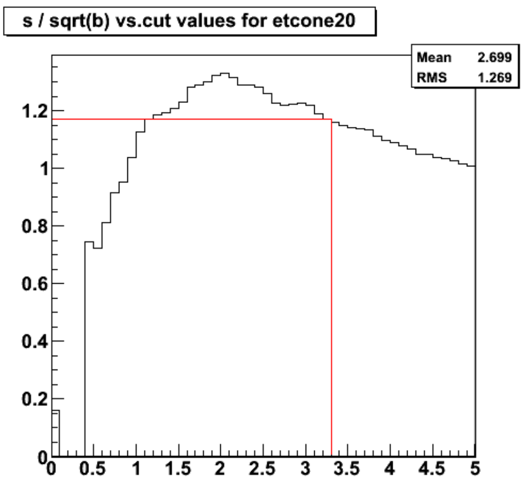

(a) $\frac{t\bar{t}}{\sqrt{QCD}}$ for E_T^{isol} in a cone $\Delta R < 0.2$

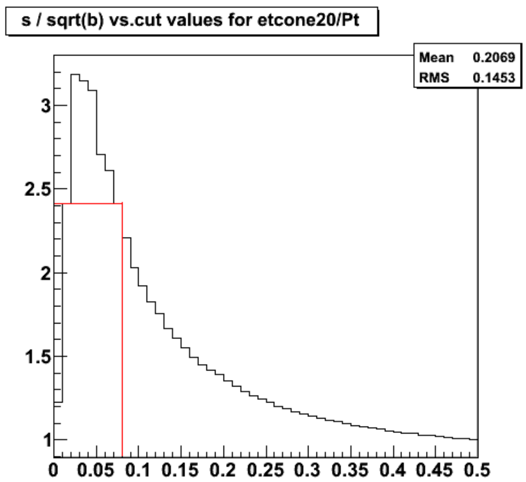

(b) $\frac{t\bar{t}}{\sqrt{QCD}}$ for $\frac{E_T^{isol}}{P_T}$ in a cone $\Delta R < 0.2$

Figure 5.13: Isolation parameter and ratio of signal passing those cuts for a electron reconstructed with a medium tightness

5.5 Results of final selection criteria

The probability distributions in N_{jets} and $\not{E}_T$ for a reconstruction demanding simply a tight electron and tight muon with P_T above 15 GeV can be seen in appendix A.3. The total signal from the three processes amounts to 63 events in 10 pb^{-1} but the background contribution is 149 events for the same luminosity resulting in a signal over background ratio of 0.42. Clearly a fit of the different signal cross section from their shapes will be very difficult. If the background was limited to a certain area of the N_{jets}–$\not{E}_T$ space the fit could still be performed but unfortunately this is not the case as can be seen from the distribution plots in appendix A.3.

The final values after selection including both medium, isolated and tight, isolated selection cuts are listed in Tab. 5.5 and Tab. 5.6. Signal over background ratios have been calculated for the entire samples to clarify the differences. The number of events are scaled to 1 pb^{-1} to allow for easy rescaling to any desired integrated luminosity. Looking at the signal over background ratio of the medium, isolated selection, the value is 1.9. The selection with just tight electron and tight muon gave a signal over background ratio of 0.42 so the gain is significant. Table 5.5 shows that 62 events pass the medium, isolated selection in 10 pb^{-1}, so very little statistics is lost with regard to the 63 events from the simple tight - tight selection without isolation.

For the tight, isolated selection in Tab. 5.6 the signal to background is even higher. Here we have the value 6.5 while 48 signal events still pass the selection in 10 pb^{-1}. The distributions in the $N_{jets} - \not{E}_T$ plane of the different signal and background processes will act as our probability distribution functions for fitting data. That is, the shapes that we get from the simulation processes, which are plotted in Figures 5.14 and 5.15, are used as shapes describing the probability of an event ending up in any of the different bins in $\not{E}_T - N_{jets}$ space from a given process.

5.5.1 The distribution of the three processes in $\not{E}_T - N_{jets}$

Figure 5.14a to 5.14f show the three signal processes plotted with a contour plot to show the distributions in the $\not{E}_T - N_{jets}$ space. The figures have all been scaled to 10 pb^{-1}. $Z \rightarrow \tau\tau$ is located in the low $\not{E}_T$ and low N_{jets} region, whereas WW differ by having higher $\not{E}_T$ as expected due to the larger fraction of energy the neutrinos receive from W's compared to taus from Z. $t\bar{t}$ is both higher in number of jets peaking at three to four and higher in $\not{E}_T$ with the distribution centred around 75 GeV. It is seen, that events from Z constitutes the bulk of the distribution and that it might be difficult to separate out WW from the two other. The last two figures show the combined background distribution. It lies predominantly in the lower region of both $\not{E}_T$ and N_{jets} and will therefore affect $t\bar{t}$ the least.

In Fig. 5.15 the same distributions have been plotted for the tight, isolated selection again scaled to 10 pb^{-1}. The distributions closely resemble the distributions of Fig. 5.14 with the exception, that the background distribution is suppressed further, especially in the low jet region. It now lies predominantly in the same region as the WW signal. The peaks in the distribution stem from the QCD background's lack of statistics.

Table 5.5: Signal for reconstructed eμ with medium, isolated electron and medium, isolated muon

Process	Events generated	e μ events selected	acceptance after selection	initial filter-efficiency	after scaling to 1 pb^{-1}
$t\bar{t}$	199828	5172 ± 72	2.59%	0.50	2.30
WW	249837	8205 ± 91	3.28%	0.324	0.59
$Z \rightarrow \tau\tau + 0$partons	303359	870 ± 29	0.29 %	1.0	2.26
$Z \rightarrow \tau\tau + 1$parton	63481	275 ± 16	0.43%	1.0	0.72
$Z \rightarrow \tau\tau + 2$partons	19492	104 ± 10	0.53%	1.0	0.26
$Z \rightarrow \tau\tau + 3$partons	5497	21 ± 5	0.38%	1.0	0.05
$Z \rightarrow \tau\tau + 4$partons	1499	5 ± 2	0.33%	1.0	0.01
$Z \rightarrow \tau\tau + 5$partons	499	3 ± 2	0.6%	1.0	0.01
					Total: 6.2
$We\nu \leq 5$partons	1896152	16 ± 4	0.00021%	-	0.64
$W\mu\nu \leq 5$partons	1897183	200 ± 14	0.011%	-	1.0
$W\tau\nu \leq 5$partons	1876156	10 ± 3	0.00053%	-	0.05
$Wbb \leq 5$partons	6499	8 ± 3	0.12%	-	0.048
WZ	249830	1300 ± 36	0.52%	-	0.028
ZZ	249725	909 ± 30	0.36%	-	0.0043
$W\mu^+ + \gamma$	50000	252 ± 16	0.50%	-	0.17
$W\mu^- + \gamma$	49992	233 ± 15	0.47%	-	0.16
$Z \rightarrow ee \leq 5$ partons	394651	2 ± 1	0.00051%	-	0.0042
$Z \rightarrow \mu\mu \leq 5$ partons	393431	236 ± 15	0.060%	-	0.50
single top Wt $\rightarrow$ inclusive	14995	242 ± 16	1.61%	-	0.24
$QCDJ2 \leq 5$ partons	380820	3 ± 2	0.0008%	-	0.50
$QCDJ3 \leq 5$ partons	84457	0 ± 0	0%	-	0
$QCDbbJ2 \leq 5$ partons	105919	0 ± 0	0%	-	0
$QCDbbJ3 \leq 5$ partons	26493	0 ± 0	0%	-	0
					Total: 3.3
					$\frac{S}{B} = 1.9$

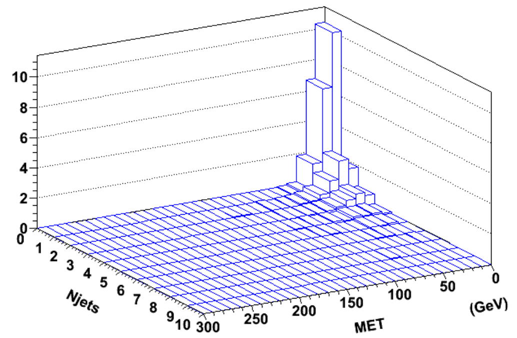

(a) Alpgen $Z\tau\tau \rightarrow e\mu \leq 5$partons

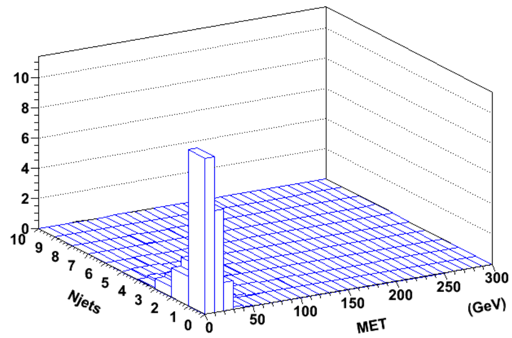

(b) Alpgen $Z\tau\tau \rightarrow e\mu \leq 5$partons

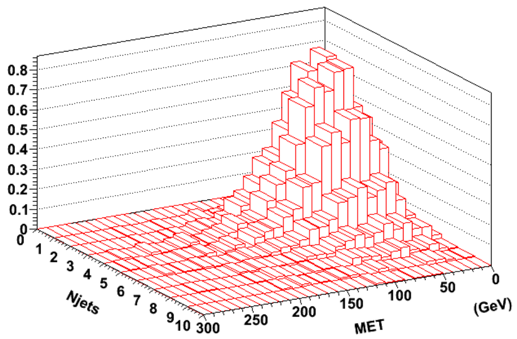

(c) MC@NLO $t\bar{t} \rightarrow e\mu$

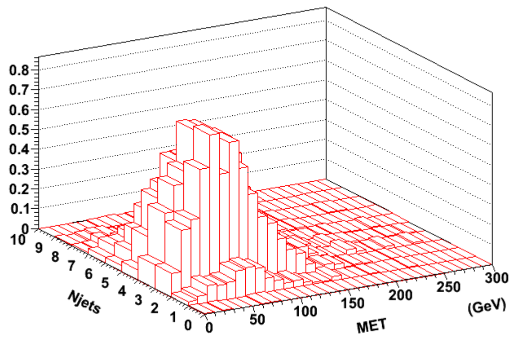

(d) MC@NLO $t\bar{t} \rightarrow e\mu$

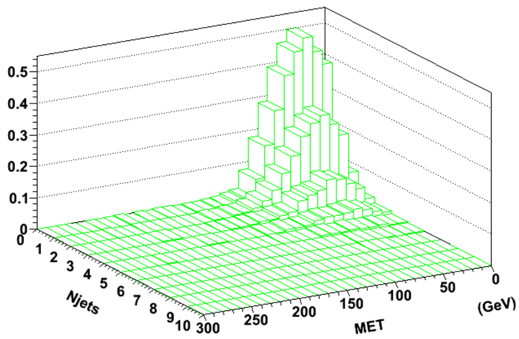

(e) Herwig $WW \rightarrow e\mu$

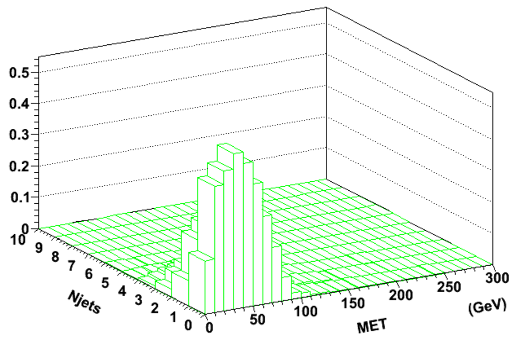

(f) Herwig $WW \rightarrow e\mu$

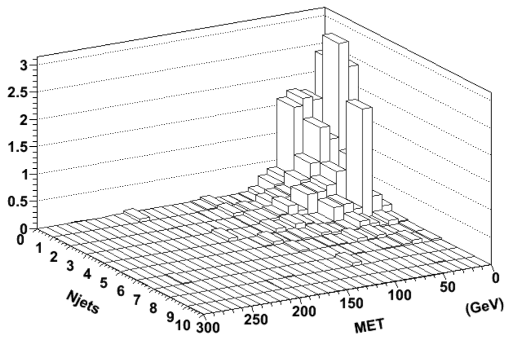

(g) $e\mu$ from combined $Wl\nu + jets, WZ, ZZ, Zee, Z\mu\mu$, single top $Wt, W\mu\gamma$ and $QCD_{b\bar{b}}$

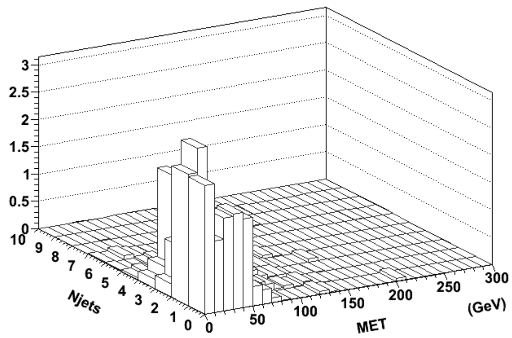

(h) $e\mu$ from combined $Wl\nu + jets, WZ, ZZ, Zee, Z\mu\mu$, single top $Wt, W\mu\gamma$ and $QCD_{b\bar{b}}$

Figure 5.14: signal and background from reconstructed medium, isolated e and μ events

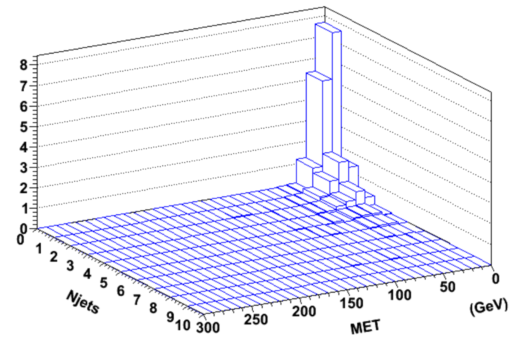

(a) Alpgen $Z\tau\tau \rightarrow e\mu \leq 5$partons

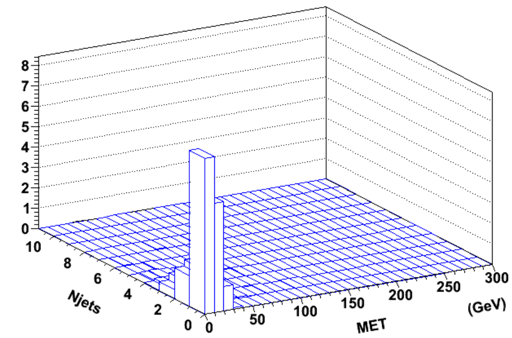

(b) Alpgen $Z\tau\tau \rightarrow e\mu \leq 5$partons

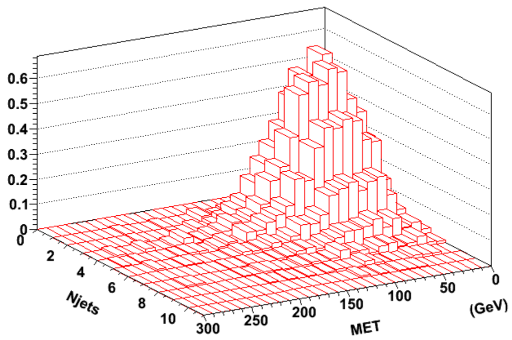

(c) MC@NLO $t\bar{t} \rightarrow e\mu$

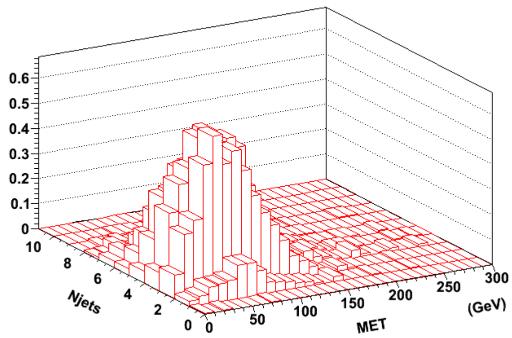

(d) MC@NLO $t\bar{t} \rightarrow e\mu$

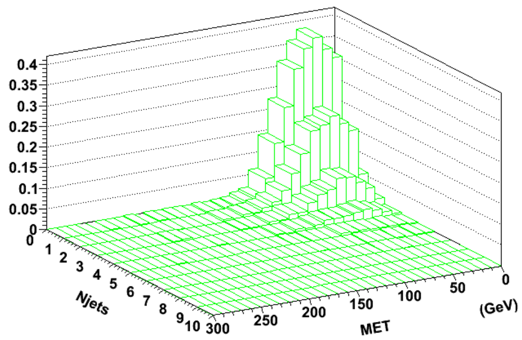

(e) Herwig $WW \rightarrow e\mu$

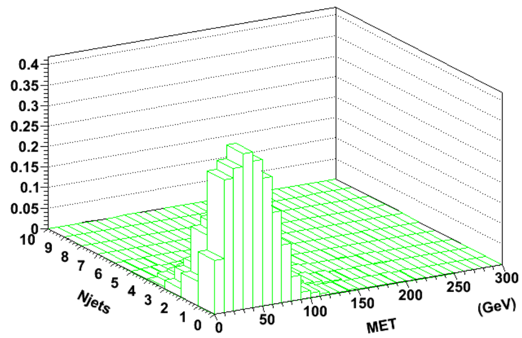

(f) Herwig $WW \rightarrow e\mu$

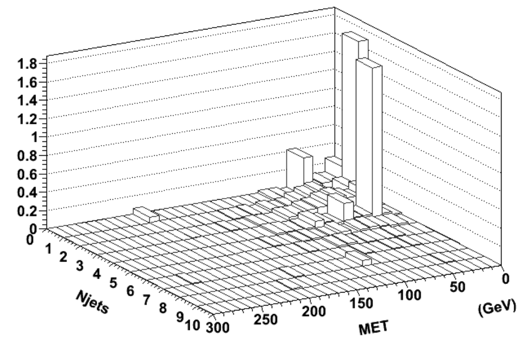

(g) $e\mu$ from combined $Wl\nu + jets, WZ, ZZ, Zee, Z\mu\mu$, single top $Wt, W\mu\gamma$ and $QCD_{b\bar{b}}$

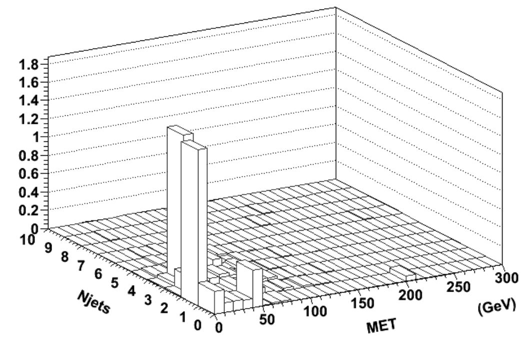

(h) $e\mu$ from combined $Wl\nu + jets, WZ, ZZ, Zee, Z\mu\mu$, single top $Wt, W\mu\gamma$ and $QCD_{b\bar{b}}$

Figure 5.15: signal and background from reconstructed tight, isolated e and μ events

Table 5.6: Signal for reconstructed eμ with tight, isolated electron and tight, isolated muon

Process	Events generated	e μ events generated	acceptance after selection	initial filter-efficiency	after scaling to 1 pb^{-1}
$t\bar{t}$	199828	4131 ± 64	2.07%	0.50	1.84
WW	249837	6432 ± 80	2.57%	0.324	0.46
$Z \rightarrow \tau\tau + 0$partons	303359	647 ± 25	0.213%	1.0	1.68
$Z \rightarrow \tau\tau + 1$parton	63481	226 ± 15	0.36%	1.0	0.57
$Z \rightarrow \tau\tau + 2$partons	19492	78 ± 9	0.40%	1.0	0.19
$Z \rightarrow \tau\tau + 3$partons	5497	14 ± 4	0.25%	1.0	0.034
$Z \rightarrow \tau\tau + 4$partons	1499	4 ± 2	0.133%	1.0	0.0096
$Z \rightarrow \tau\tau + 5$partons	499	2 ± 1	0.4%	1.0	0.0034
					Total: 4.8
$We\nu \leq 5$partons	1896152	6 ± 3	0.00032%	-	0.03
$W\mu\nu \leq 5$partons	1897183	15 ± 4	0.00079%	-	0.075
$W\tau\nu \leq 5$partons	1876156	2 ± 1	0.00011 %	-	0.01
$Wbb \leq 5$partons	6499	3 ± 2	0.046%	-	0.0018
WZ	249830	1199 ± 35	0.48%	-	0.026
ZZ	249725	755 ± 28	0.30%	-	0.0035
$W\mu^+ + \gamma$	50000	11 ± 3	0.022%	-	0.0075
$W\mu^- + \gamma$	49992	11 ± 3	0.022%	-	0.0075
$Z \rightarrow ee \leq 5$ partons	394651	0±0	0%	-	0
$Z \rightarrow \mu\mu \leq 5$ partons	393431	23 ± 5	0.0058%	-	0.048
single top Wt → inclusive	14995	201 ± 14	0.013%	-	0.20
$QCDJ2 \leq 5$ partons	380820	2 ± 1	0.00053%	-	0.33
$QCDJ3 \leq 5$ partons	84457	0 ± 0	0%	-	0
$QCDbbJ2 \leq 5$ partons	105919	0 ± 0	0%	-	0
$QCDbbJ3 \leq 5$ partons	26493	0 ± 0	0%	-	0
					Total: 0.7
					$\frac{S}{B} = 6.5$

5.6 AcerMC PowHeg_Pythia vs. MCNLO Jimmy/Herwig

As a bi-product of the work on the thesis it became clear, that reconstruction from two of the otherwise widely used generators for $t\bar{t}$ production gave noticeable different results. Figure 5.16 shows the distribution for different selections. The plots show that AcerMC with PowHeg-Pythia hadronisation lies about 7% lower than MC@NLO with Jimmy/Herwig for hadronisation. As was seen in Tab. 5.4 the number of events with simply the tight - tight selection was the same namely 6500 before scaling. Therefore the difference must lie in the degree of isolation of the leptons. To determine whether this stems from the generator or the hadronisation would require further investigation and is beyond the scope of this thesis. The peak of the distribution seems to be shifted slightly towards higher $\not{E}_T$ while number of jets are very similar. Apart from this and the lower integrals of AcerMC the distributions are very similar.

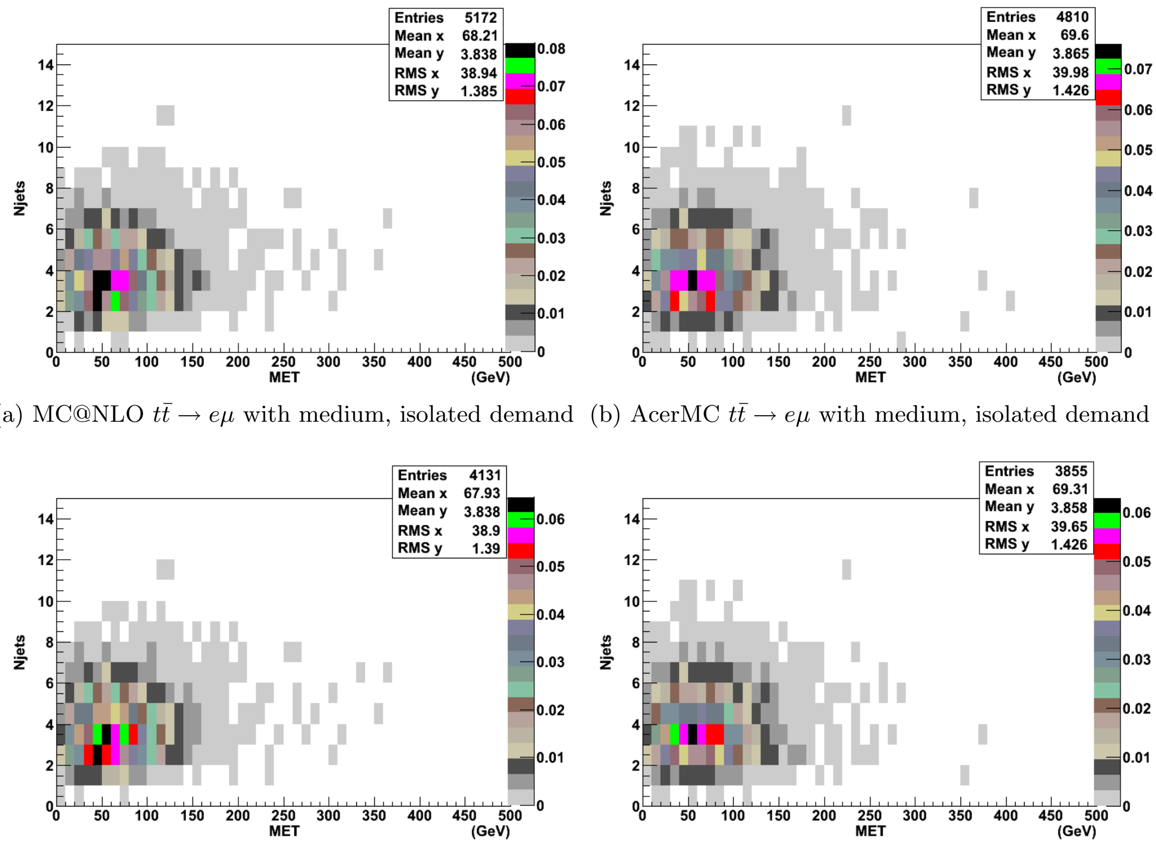

(a) MC@NLO $t\bar{t} \to e\mu$ with medium, isolated demand (b) AcerMC $t\bar{t} \to e\mu$ with medium, isolated demand

(c) MC@NLO $t\bar{t} \to e\mu$ with tight, isolated demand (d) AcerMC $t\bar{t} \to e\mu$ with tight, isolated demand

Figure 5.16: Comparison of AcerMC and MCNLO

The difference is important, as it gives an idea of the lower bound on the systematic uncertainty of the generator. It is not only relevant for the $t\bar{t}$ process, but also for single top Wt channel, as this is produced by AcerMC. It is not clear from the above, which MC generator is not correctly reproducing number of jets or $\not{E}_T$ or even whether any of them are. The conclusion is however, that the difference between generators can vary with a significant percentage and this should be taken into account when studying systematic uncertainties.

For the same reason the systematic error will be included for all samples.

Chapter 6

Fitting

6.1 The minimum log likelihood method

The cross sections for the different processes can be derived by doing what is called a log(likelihood) fit of a simulated or real sample of data, containing all the SM processes contributing to the di-lepton final state, to the MC generated distributions for signal and background plotted in Figures 5.14 and 5.15. If a set of variables, x_i, is distributed according to a probability distribution function $f(x;\theta)$, where θ represents unknown parameters, then these parameters can be estimated for a finite data sample. In our case the parameters are production cross sections for the different processes and the data is simulated or real data binned in the $\not{E}_T - N_{jets}$ space. The probability that the first measurement will be in $[x_1, X_1 + dx_1]$ is $f(x_1;\theta)$ for a given θ. Since all measurements are assumed independent this means that

$$\text{probability that} \quad x_i \quad \text{in} \quad [x_i, x_i + dx_i] \quad \text{for all i is:} \quad \prod_{i=1}^{n} f(x_i;\theta)dx_i. \tag{6.1}$$

In our case the data intervals are bins and f the probabilities, that a data point falls in that bin for a given distribution or in other words, the probability that a given data point in a bin is coming from a given process. If the hypothesised function $f(x_i;\theta)$ (our MC generated distributions) and the parameters (fitted cross section) are correct, we expect a high probability for the data that was actually measured. As dx_i is independent of the parameters the same reasoning applies to the *likelihood function*

$$L(\theta) = \prod_{i=1}^{n} f(x_i;\theta). \tag{6.2}$$

This function should be large if the data fits the hypothesis and small if data and hypothesis does not match. The estimators for this are given by

$$\frac{\partial L}{\partial \theta_i} = 0, \tag{6.3}$$

for the range of parameters i. In the case of a Gaussian distribution, the parameters will be the mean, μ, and the width, σ. Rather than using the likelihood function the logarithm of it is often more convenient to use. Since the logarithm is a monotonically increasing function, the value of the parameter, that maximises L, will also maximise $log(L)$. For large samples the likelihood becomes gaussian [54] and takes the form

$$L = \prod_i f(x_i^{pred}(\theta), \sigma_i) \tag{6.4}$$

Our likelihood function is formed from the Poisson probabilities comparing each bin in the $\not{E}_T - N_{jets}$ space of the simulated or real data with each bin in the Monte Carlo generated Standard Model distributions. For this case, the likelihood is defined as:

$$L = \prod_i \rho_i = \frac{\mu_i^{n_i} e^{-\mu_i}}{n_i!} \tag{6.5}$$

where i runs over all bins in our 2-D distributions and where n_i is the bin content for that particular bin in the data. μ_i is the total expected number of events given by:

$$\mu_i = \alpha N_{t\bar{t}_i} + \beta N_{WW_i} + \gamma N_{Z \to \tau\tau_i} + n_{other_i} \tag{6.6}$$

When only considering Standard Model contributions in the $e\mu$ channel, the data distributions are given by:

$$\frac{\delta^2 N}{\delta \not{E}_T \delta N_{jets}} = \alpha N_{t\bar{t}} + \beta N_{WW} + \gamma N_{Z \to \tau\tau} + n_{other}, \tag{6.7}$$

where the $t\bar{t}$, WW and $Z \to \tau\tau$ distributions (N_i) are normalised to 1 and the parameters α, β and γ are the fit variables from each contribution. They are related to the cross sections through $N = \sigma A \mathcal{L}$ where σ is the cross section, A is total acceptance including the branching ratios, and $\mathcal{L}$ is the integrated luminosity.

To find the best fit, the negative of the logarithm of this likelihood function, as a function of the variables α, β and γ, is minimised. This is done using the CERN package MINUIT [55], [56] together with a framework developed by CDF and adapted for ATLAS in cooperation with Mark Kruse from the University of Duke, North Carolina.

The actual form of the likelihood function we use for our fits is not as simple as the above. When fitting to real data, we have to account for systematics errors from acceptances and luminosity when measuring cross-sections. This is done by adding Gaussian constraints for acceptances and luminosity. In other words, the true value can be regarded as a Gaussian random variable centred about the quantity's true value. This can be described by terms G_f to be multiplied to the likelihood function.

$$G_f = e^{-\frac{(A_f - \hat{A}_f)^2}{2\sigma_{A_f}^2}} \tag{6.8}$$

where, f refers to a given parameter with systematic uncertainty for each source, $\hat{A}_f$ is its expected value, σ_{A_f} is its uncertainty, and A_f is it's value in the fit. The description follows from the central limit theorem [57] when the total error, i.e. deviation from the true value, can be seen as the sum of a number of small contributions. For this reason the value of A_f is only allowed to float so far, that G_f doesn't reduce the Likelihood significantly.

6.2 Fit values

To determine the precision that can be achieved when extracting simultaneously the cross section for the three SM processes, we use a MC fully simulated control sample and fit against it. This sample is a combined sample of Standard Model signal and background processes for lepton studies, that contain all the relevant processes for this study. Using this sample as data-input for the fit will give an estimate of what our statistical errors are and how well we can fit the different signals with our shapes. The size of the sample corresponds to an integrated luminosity of 9.655 pb^{-1}.

Using the medium, isolated selection and allowing all signal processes to float gives the values seen in Tab. 6.1. The values listed here are the values of the fitted cross sections divided by the expected SM cross sections, denoted α. The fit has been done both without any systematic uncertainties and with a 10% uncertainty. As our distributions for $t\bar{t}$ are based on MC@NLO and the control sample was made with AcerMC, the 10% systematic uncertainty is imposed to reflect a very conservative estimate of the discrepancies between the generators used, that was seen to be 7% between the MC@NLO and AcerMC $t\bar{t}$ samples. It has been imposed on all three processes.

As a further test of the behaviour of the fit, $t\bar{t}$ and $Z \to \tau\tau$ were each allowed to float in separate fits, where all other processes were kept fixed at the Standard Model expectation.

Table 6.1: Fit values for all processes floating after medium, isolated selection

Process	$\alpha_i = \frac{\sigma_i A_i \mathcal{L}_i}{N_i}$	statistical errors	events in data	systematics
$t\bar{t}$	1.02	$+0.27 - 0.24$	22.2	no
WW	0.62	$+0.79 - 0.51$	5.7	no
$Z \to \tau\tau$	0.91	$+0.23 - 0.21$	30.0	no
$t\bar{t}$	1.07	$+0.33 - 0.27$	22.2	yes
WW	0.66	$+0.85 - 0.54$	5.7	yes
$Z\tau\tau$	0.95	$+0.29 - 0.24$	30.0	yes
		$t\bar{t}$ fixed - all other floating		
$t\bar{t}$	1.08	$+0.33 - 0.27$	22.2	no
$t\bar{t}$	1.00	$+0.27 - 0.24$	22.2	yes
		$Z\tau\tau$ fixed - all other floating		
$Z\tau\tau$	0.89	$+0.23 - 0.20$	30.0	no
$Z\tau\tau$	0.93	$+0.28 - 0.24$	30.0	yes

6.2.1 Cross sections from the fit

When using the fitted α parameter to get an actual cross section, the following is done. The generated cross sections are given with filters included e.g. $\sigma_{t\bar{t}} = 80.201$pb, is the production cross-section multiplied by an acceptance for a filter demanding one lepton with a certain P_T. This filter efficiency is known and can be combined with our own acceptance to give us the cross section for $t\bar{t} \to e\mu$. From this we can, by dividing by the branching ratio $\Gamma_{t\bar{t}\to e\mu}$, get the final cross section for $t\bar{t}$. The generalised equation is shown in Eq. 6.9.

$$\sigma_i = \frac{\alpha_i \cdot N_i}{A_i \cdot \mathcal{L}_i}, \tag{6.9}$$

where A_i is the combined acceptance including branching ratios, reconstruction efficiency and filter efficiency. The values are summarised in Tab. 6.2.

Table 6.2: Acceptances and efficiencies used in determining cross sections from the fit.

Process	acceptance	filter efficiency
	medium, isolated	
$t\bar{t}$	0.026	0.50
WW	0.033	0.32
$Z \to \tau\tau$	0.004	1.00
	tight, isolated	
$t\bar{t}$	0.021	0.50
WW	0.026	0.32
$Z \to \tau\tau$	0.003	1.00

Equations 6.10 to 6.12 show the calculations to extract the cross-sections for the three signal processes for the medium, isolated selection.

$$\sigma_{Z\tau\tau} = \frac{\alpha_{Z\tau\tau} \cdot 30.0473}{0.0043 \cdot 9.655\text{pb}^{-1}} = \alpha_{Z\tau\tau} \cdot 729\text{pb} \tag{6.10}$$

$$\sigma_{t\bar{t}} = \frac{\alpha_{t\bar{t}} \cdot 22.2171}{0.026 \cdot 0.5 \cdot 9.655\text{pb}^{-1}} = \alpha_{t\bar{t}} \cdot 178\text{pb} \tag{6.11}$$

$$\sigma_{WW} = \frac{\alpha_{ww} \cdot 5.66349}{0.033 \cdot 0.324 \cdot 9.655\text{pb}^{-1}} = \alpha_{ww} \cdot 55\text{pb} \tag{6.12}$$

The results are shown in Tab. 6.3. It should be noted, that $\gamma^* \to \tau\tau$ corrections have not been made for the $Z \to \tau\tau$ ($Z/\gamma* \to \tau\tau$) process, as the contribution has been shown to be low. The results are also shown for fits where the $Z \to \tau\tau$ and $t\bar{t}$ distributions respectively were allowed to float while other processes have been kept fixed. Although the fundamental idea of this analysis is the fitting of all cross sections simultaneously it is interesting to see how the program behaves when only one is allowed to float. The method will still have a statistical advantage over an exclusive fit, but will also demand that we understand the two other distributions well enough to trust the shape of their distributions. This will not be the case for early data. The gain with regard to statistical errors is however only there for $Z \to \tau\tau$ whereas $t\bar{t}$ actually has higher statistical errors when keeping the other two processes fixed.

In Tab. 6.4 the fit has been performed with shapes and samples selected with a tight, isolated electron and muon. Recalling the discussion earlier, this scenario will give the highest background rejection, but also lower statistics. The results indicate, that the larger statistical uncertainties is a problem for the tight, isolated selection for sample size of order 10 pb^{-1}.

6.3 Goodness of fit

To test the goodness of fit, two statistical fits have been made. A χ^2 test has been calculated based on a fit of the entire sample, whereas a Kolmogorov-Smirnov (KS) test has been performed on each slice of number of jets in the $N_{jets}-\not{E}_T$ space. The KS test is a distribution independent test of the goodness of fit between two distributions. In short the closer the value is to 1, the better the fit, whereas the smaller the value, the poorer the fit. Values of exactly 1 might not necessarily indicate a perfect fit but could be caused by poor statistics. The χ^2 test is calculated by the equation

$$\chi^2 = \Sigma \frac{(O - E)^2}{\sigma^2}, \tag{6.13}$$

where O is observations, E is expected and σ^2 is the variance of the observation. To normalise for number of data points and model complexity, the reduced χ^2 test is used, where the χ^2 is divided by the number of degrees of freedom, ndf. ndf is normally given by $N - n - 1$, where N is observations and n is number of fitted parameters. The value of $\frac{\chi^2}{ndf}$ should be close to one, with values higher than one indication a poor fit, and value too much below one indicating that the model is "overconstraining" the data. Here values of exactly one generally indicate a perfect fit.

In Fig. 6.1 the fit of all control sample data points to the signal and background shapes has been plotted. The χ^2 test gives a value within reasonable distance of one, indicating, that the fit although not perfect, is acceptable.

A better understanding of the goodness of fit can be derived from Fig. 6.2 where the KS values of the fit to the individual slices in number of jets has been plotted. The values all lie close to one with the exception of $N_{jets} = 7$ where there is no data and therefore obviously no agreement between the fit and the data. The shapes go up to $N_{jets} = 15$ and slices have been done for the entire range, but there is no discrepancy with the presented picture in any of the above slices.

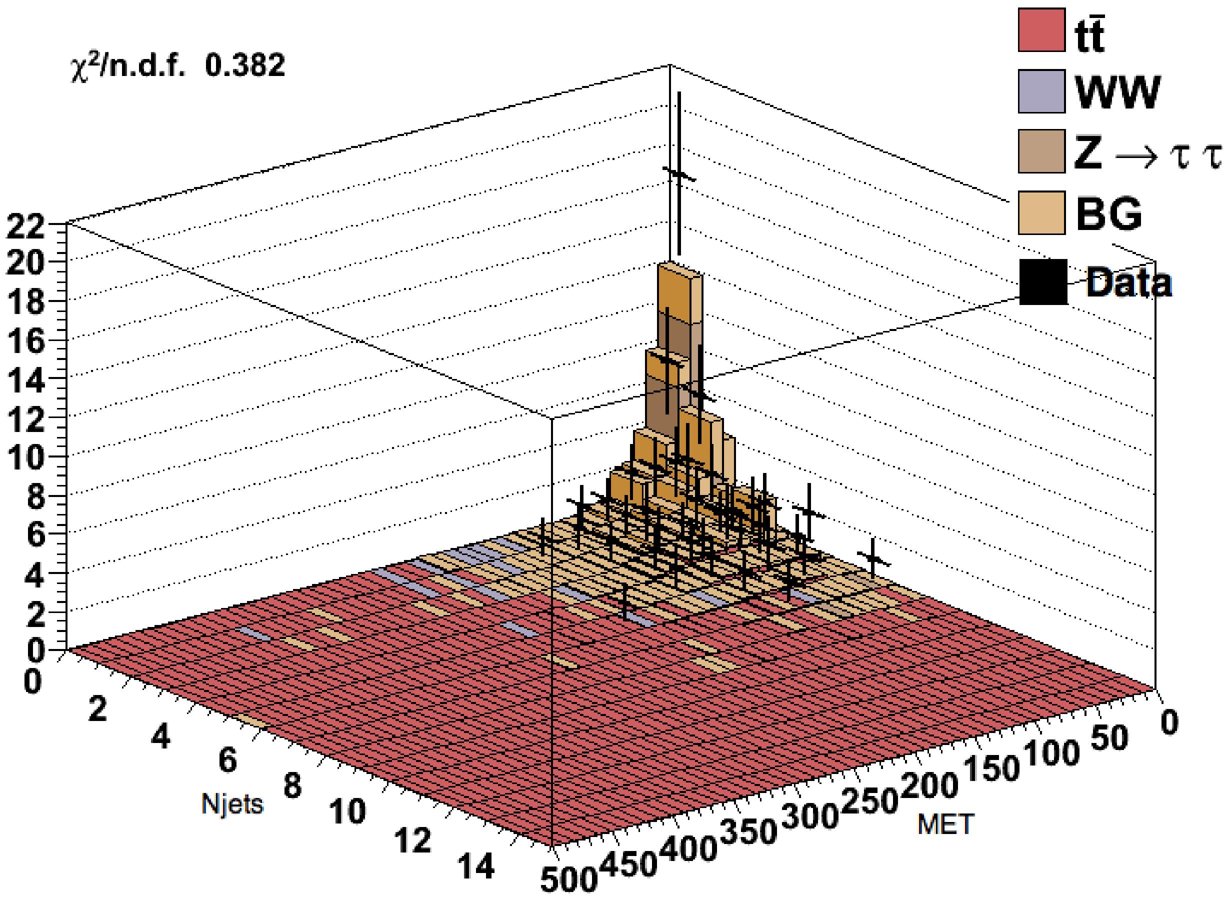

Figure 6.1: Data points from control sample with statistical errors and fit values for all signals floating.

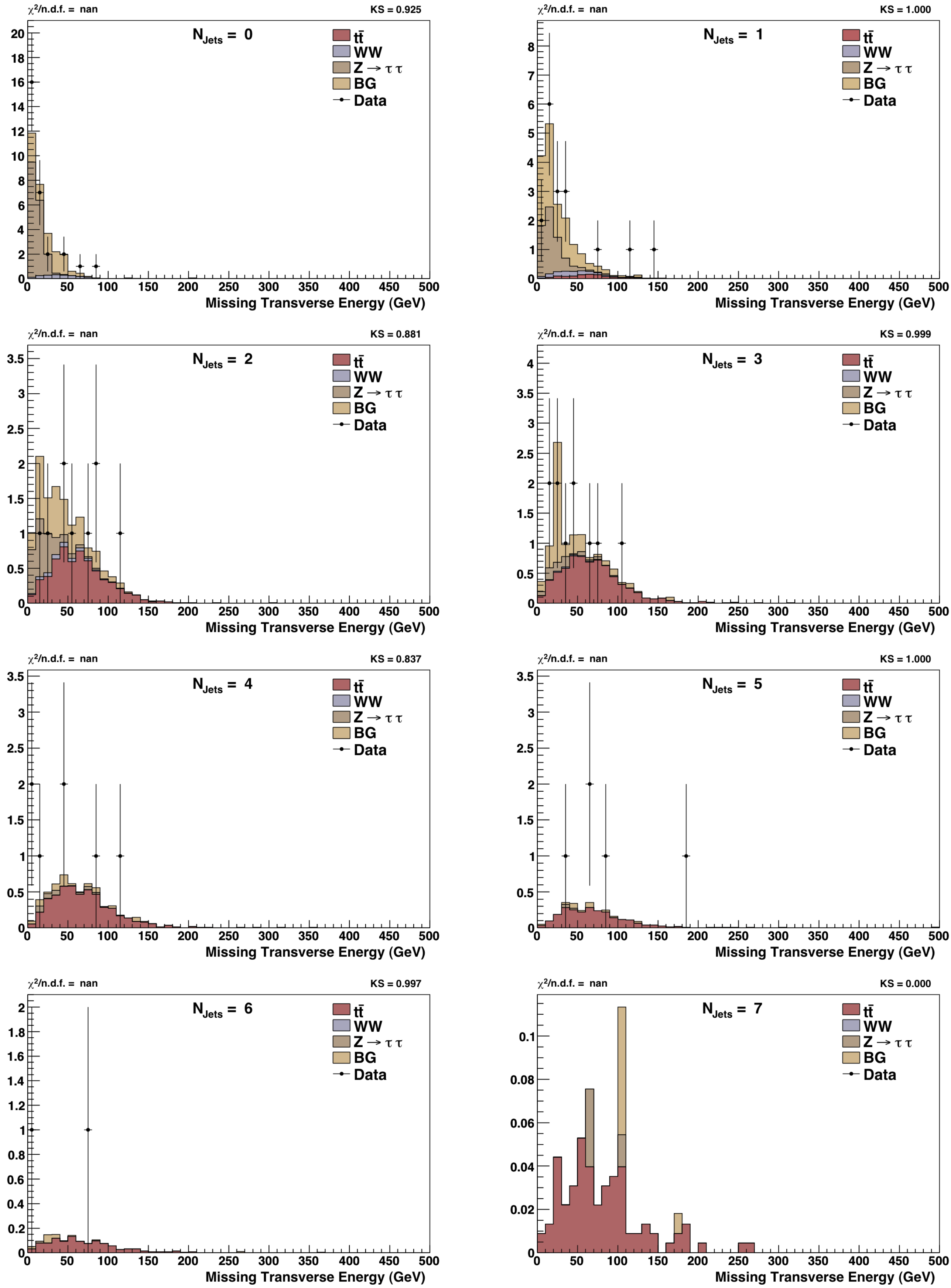

Figure 6.2: Fit values for slices in number of jets for the $9.65\ \mathrm{pb}^{-1}$ all signals floating pseudodata sample. Errors are purely statistical.

Table 6.3: Fitted cross sections for all processes floating after medium, isolated selection in 10 pb^{-1}

Process	$\sigma_i = \frac{\alpha_i N_i}{\Gamma_i A_i \mathcal{L}_i}$ (pb)	statistical errors	expected events	events in pseudodata	systematics
$t\bar{t}$	182	$+49 - 43$	22.2	22.2	no
WW	34	$+44 - 28$	5.7	3.5	no
$Z \to \tau\tau$	660	$+168 - 150$	30.0	27.2	no
$t\bar{t}$	189	$+58 - 48$	22.2	22.9	yes
WW	37	$+47 - 30$	5.7	3.6	yes
$Z\tau\tau$	689	$+208 - 173$	30.0	27.5	yes
	$t\bar{t}$ floating - all other fixed				
$t\bar{t}$	192	$+58 - 49$	22.2	22.2	no
$t\bar{t}$	177	$+48 - 42$	22.2	22.9	yes
	$Z\tau\tau$ floating - all other fixed				
$Z\tau\tau$	647	$+165 - 147$	30.0	27.2	no
$Z\tau\tau$	679	$+203 - 171$	30.0	27.5	yes

Table 6.4: Fitted cross sections for all processes floating with tight, isolated selection in 10 pb^{-1}

Process	$\sigma_i = \frac{\alpha_i N_i}{\Gamma_i A_i \mathcal{L}_i}$ (pb)	statistical errors (pb)	expected events	events in pseudodata	systematics
$t\bar{t}$	216	$+56 - 48$	17.7	21.6	no
WW	79	$+55 - 40$	4.4	6.4	no
$Z \to \tau\tau$	807	$+206 - 181$	22.2	22.8	no
$t\bar{t}$	220	$+64 - 53$	18	21.6	yes
WW	81	$+58 - 41$	4.4	6.4	yes
$Z\tau\tau$	825	$+237 - 198$	22.2	22.8	yes

6.3.1 Test of fit-method

To test the reliability of the results of the fit method 10.000 pseudo experiments (PE) have been performed. The pseudo experiments varies the results around the central fit values and test a series of variables to clarify the reliability of the fit method. One of the possible ways of expressing the reliability through these PE's is by plotting the "pull-distributions" for the three processes. The pull distributions clarify the difference between the fitted and the expecterd cross-section with the spread representing the errors. More precisely, the statistical error calculated for the fit will be reliable if 67% of the PE-generated values lie within one standard deviation of the cross section found by the fit. The pull distribution is defined as:

$$\frac{\sigma_{Fit} - \sigma_{mean,PE}}{\sqrt{\Delta\sigma^2_{Fit} - \Delta\sigma^2_{mean,PE}}}, \tag{6.14}$$

where $\Delta\sigma_{Fit}$ is the statistical error on σ_{Fit}. It should be a gaussian distribution centred around 0 with a width of 1 if the errors are reliable. When using the CERN MINUIT package [55] the errors returned will be asymmetric. In this case, the pull distributions are defined as:
if (fit result) $\leq$ (true value):

$$g = \frac{\text{(true value)} - \text{(fit result)}}{\text{positive MINOS error}} \tag{6.15}$$

otherwise:

$$g = \frac{\text{(true value)} - \text{(fit result)}}{\text{negative MINOS error}}, \tag{6.16}$$

where MINOS is the algorithm used for error calculations in MINUIT.

The pull distributions have been plotted in Fig. 6.3. The width and mean for all three processes fitted with a gaussian are very reasonable and the error estimates of the distributions are therefore reliable. The $\frac{\chi^2}{ndf} = \frac{454.2}{42}$ of the WW pull distribution constitute the largest deviation from a gaussian, but the width indicate, that the errors are only around 1.5% off.

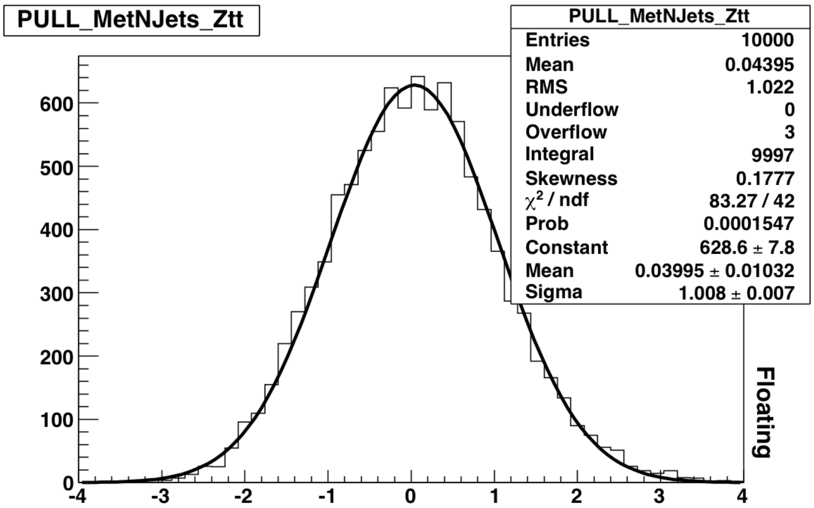

(a) Pull distribution for PE experiments varying the$Z\tau\tau$ fit value

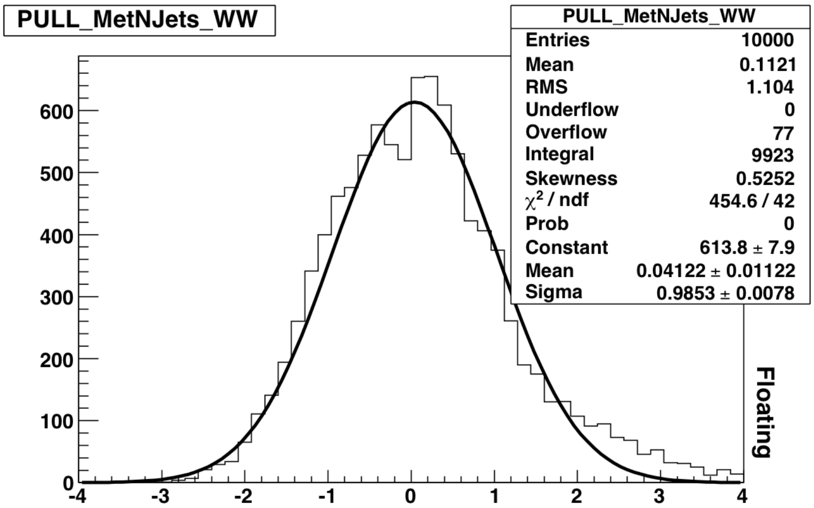

(b) Pull distribution for PE experiments varying the WW fit value

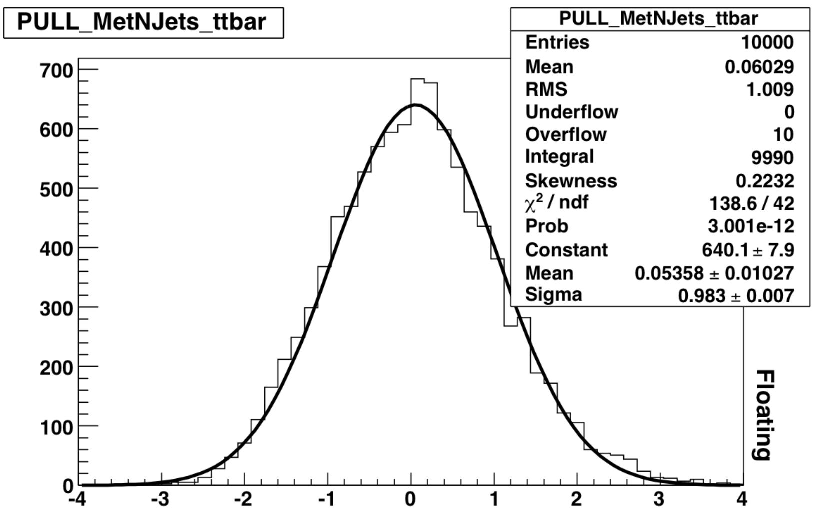

(c) Pull distribution for PE experiments varying the $t\bar{t}$ fit value

Figure 6.3: Fit values for slices in number of jets for the 9.65 pb^{-1} all signals floating sample without systematic errors.

6.4 Comparison to exclusive measurements in ATLAS

The $t\bar{t}$ cross-section in Tab. 6.3 can be compared with the cross section achieved by the top working group in their draft paper on top exclusive cross section [58]. The article presents measurements of $t\bar{t}$ production in pp collisions at a centre-of-mass energy $\sqrt{(s)} = 7$ TeV. In a data sample of 2.9 pb^{-1} recorded by the ATLAS detector at the Large Hadron Collider, 37 candidate events where observed in the single lepton topology with electrons or muons, and 9 in the dilepton topology. Backgrounds from non-$t\bar{t}$ Standard Model processes are estimated largely from data control samples in the article. When all channels are combined, the background-only hypothesis is excluded at a significance level of 4.9 standard deviations in the article. The results are not yet public but can within the regulations of ATLAS be referred to in a Master Thesis. The presented numbers are for the combined semileptonic and dilepton channels:

$$\sigma(t\bar{t}) = 146^{+37}_{-33}(stat)^{+49}_{-30}(syst)\text{pb}. \tag{6.17}$$

The paper also gives a cross section based only on the dilepton channel including opposite sign ee,$\mu\mu$ and $e\mu$ [59]. The result is:

$$\sigma(t\bar{t}) = 151^{+85}_{-68}(stat)^{+39}_{-26}(syst)\text{pb}. \tag{6.18}$$

Comparing the two numbers with our $t\bar{t}$ production cross-section from the $e\mu$ channel in Tab. 6.3, the statistical uncertainty is smaller for the single lepton topology but larger for the dilepton channel. Bearing in mind, that the dilepton channel is both ee, $e\mu$ and $\mu\mu$ the method presented in this thesis will give a fit with smaller statistical errors.

For $Z \to \tau\tau$ the cross section has also been measured and is published in [60]. The measurement is performed in the dilepton channel with only ee and $\mu\mu$ events of opposite charge for the ATLAS experiment at LHC with centre-of-mass energy $\sqrt{(s)} = 7$ TeV. Furthermore the measurement is performed in the invariant mass window of the leptons $66 < m_{ll} < 116GeV$). The study included a total of 320 nb^{-1} and gave the following result:

$$\sigma_{Z\to ll(all)} = 0.82^{+0.06}_{-0.06}(stat)^{+0.05}_{-0.05}(syst)^{+0.09}_{+0.09}(lumi)nb \tag{6.19}$$

(within the invariant mass window $66 < m_{ll} < 116GeV$).

As noted, the Z/W cross-section is measured for leptons with an invariant mass between 66 and 116 GeV to select only those coming from the Z in $Z/\gamma*$. As we have the entire mass range in our study, the result has to be corrected to compared with ours which in nb is:

$$\sigma_{Z\to\tau\tau} = 0.66^{+0.17}_{-0.15}(stat)\text{nb} \tag{6.20}$$

We expect our errors to be larger in this channel compared to the ee and $\mu\mu$ dilepton channels due to our demand on P_T of leptons. The P_T demand of 15 GeV is much harder, when imposed on the electron and muon from Z through tau decays, than when imposed on the electron or muon pairs originating directly from a Z. The leptons from the taus share transverse momentum with the neutrinos generated in the decay and the tau will require a P_T of e.g. 45 GeV to produce an electron or muon with P_T larger than 15 GeV, if the neutrinos carry two thirds.

At the time of writing there has been performed no measurement of the WW production cross section or the $Z \to \tau\tau \to e\mu$ production cross section with collisions at LHC so a measurement of these would be the first. This serve as further motivation for performing the fit on real data.

6.5 Analysis performed on 20 pb^{-1} data

To conclude the analysis presented in this thesis, we would like to present a fit of real data to our estimated Standard Model contributions. The results shown in this section are not meant to be a detailed and accurate analysis of real data, ready for publication. They are a first step towards that. Nonetheless, it is very promising to observe the level of agreement between data and MC simulations shown in the following.

6.5.1 Data used

Not all the recorded data of the ATLAS experiment are good for physics analysis. To determine which runs were of adequate quality, studies have been performed by a dedicated data quality group at ATLAS and a list of good runs, the Good Run List (GRL), has been made.

The GRLs are based on so called Data Quality status flags or DQ flags in short. DQ flags are the traffic lights of data monitoring and are issued by each sub-detector and the combined performance groups.

During 2010 most of the DQ flags came directly from sub-detectors but some combined performances like jet, missing energy and tau reconstruction also set the status of DQ flags. The data used here are from such a GRL and stem from the latest period of data recording called period I. To get manageable sizes of data, the recorded data have been skimmed with the demand of an electron in the event with a P_T above 15 GeV identified with the so called RobustLoose criteria, where a track matching has been added to the Loose requirement or alternatively with P_T above 15 GeV and with a loose isolation demand[1]. The data from the period correspond to an integrated luminosity of roughly 20 pb^{-1}.

The lowest trigger for electron identification, that has not been prescaled for period I, is EF_e15_medium. As the selection in our analysis is requiring leptons with P_T above 15 GeV, a fraction of the data might actually be lost, as leptons with P_T just around 15 GeV might not trigger the event. The fraction is however low and will probably not influence the final result significantly.

Further studies could be based on a combination of electron and muons triggers or even $\not{E}_T$ or jet triggers to reduce lost events. Care should be taken with the combination of triggers to not count events more than once.

6.5.2 Data at first look

As a first step we look at a few of the relevant variables. Figures 6.4a to 6.4d show the $\not{E}_T$ from the refined calibrated and topologically reconstructed containers for Monte Carlo generated events and the real data. For both containers, the distribution mean is shifted slightly rightwards. It is worth noting, that there are significantly fewer events with between 0 and 20 GeV $\not{E}_T$ in the refined calibrated container. This could indicate, that the calibration is not yet optimal, and that some energy loss is still occurring, that is not taken into account in the calibration. The plots indicate, that further studies of $\not{E}_T$ could be made and that this would decrease the significant systematic uncertainty, that will have to be imposed if the understanding is not improved. There exist various $\not{E}_T$ reconstructions method, that calibrate topological read-out to get a good estimate for data without having the full understanding of the object behaviour in the event needed for the refined calibrated $\not{E}_T$.

[1]The exact demand is an isolation energy, within a cone of $\Delta R \leq 0.2$, below $4GeV + 0.023 \cdot P_T$

Figures 6.4e to 6.4h show the P_T distributions of e and μ. They look similar to the Monte Carlo expectation. Noticeably the μ P_T distribution seem to have more low P_T muons than expected from MC.

Finally Figures 6.5a and 6.5b show the number of reconstructed AntiKtH1Topo jets distributions from Monte Carlo and data respectively. There are a couple of things worth noticing. First of all the number of events with no reconstructed jets, is significantly lower in data. When colliding protons are recorded in ATLAS, the event will sometimes have more than two colliding protons. Furthermore remnants from earlier collisions can accidentally be recorded as part of the event. This is referred to as pileup. The MC used here has no pileup while the data for these periods have an average pileup of 3 with large tails. Studying pile-up in Monte Carlo and data would be interesting in the future, to establish what influence it has on especially the number of jets. There is one event with 10 jets, in addition to the isolated electron and muon, surviving the selection in data. This event is interesting in itself, as it lies in the region where we expect new physics to be seen. It is however not improbable that a 10 jet event can stem from e.g. $t\bar{t}$ with pile-up. The figures shown here indicate, as could be expected, that the data and Monte Carlo distributions have discrepancies. To compensate for the difference in distributions of number of jets, $\not{E}_T$ and lepton P_T, systematical uncertainties can be imposed.

6.5.3 Systematic uncertainties

The systematic uncertainties demand an entire study by themselves. We can however give an estimate of the value by using the systematic uncertainties found from exclusive studies for $t\bar{t}$, Z and W cross sections studies in ATLAS. The uncertainties for Z and W from [60] and [58] can be seen in Tab. 6.5. The Luminosity is giving an overall uncertainty of 11% and a 5% uncertainty is taking into account the possible event loss from triggers.

α_{reco} in Tab. 6.5 includes $\not{E}_T$ resolution and reconstruction efficiency uncertainty from the electromagnetic clusters. The MC generated cross section and distributions are given a 7 % uncertainty from parton distribution functions, combined with a 10 % uncertainty to take into account the uncertainties in both the generators shapes and cross section estimates.

Table 6.5: Systematic uncertainties used

	$\sigma_{t\bar{t}}$	$\sigma_{Z\to\tau\tau}$	σ_{WW}	$\sigma_{background}$
Luminosity	11 %	11 %	11 %	11 %
electron ID efficiency	5.2 %	4.2 %	5.2 %	5.2 %
muon ID efficiency	2.7 %	2.7 %	2.7 %	2.7 %
trigger efficiency	5 %	5 %	5 %	5 %
α_{reco}	4.5 %	3.3 %	4.5 %	4.5 %
pdf	7 %	7 %	7 %	7 %
σ_{gen}	10 %	10 %	10 %	10 %

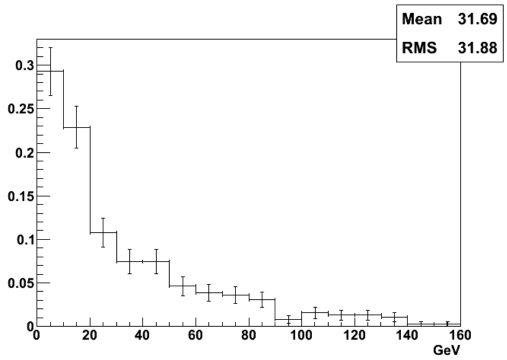

(a) Refined calibrated $\not{E}_T$ as expected from Monte Carlo simulated Standard Model events.

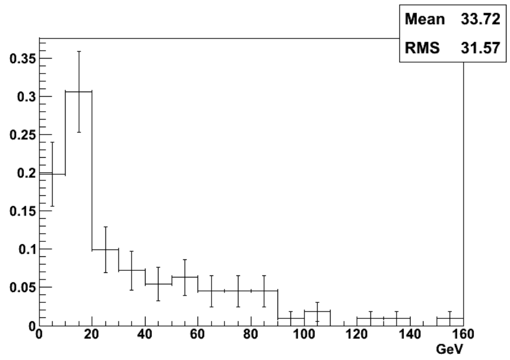

(b) Refined calibrated $\not{E}_T$ in real data from period I recorded at ATLAS during 2010.

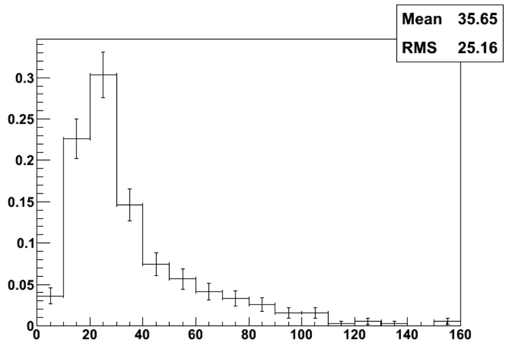

(c) Topologically calculated $\not{E}_T$ as expected from Monte Carlo simulated Standard Model events.

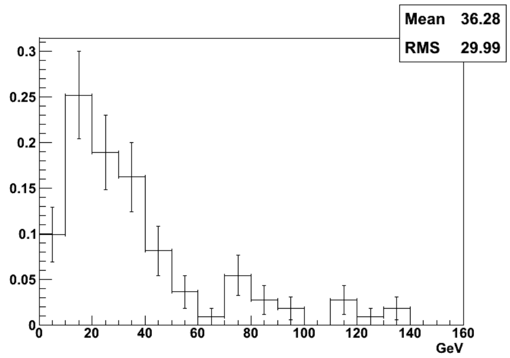

(d) Topologically calculated $\not{E}_T$ in real data from period I recorded at ATLAS during 2010.

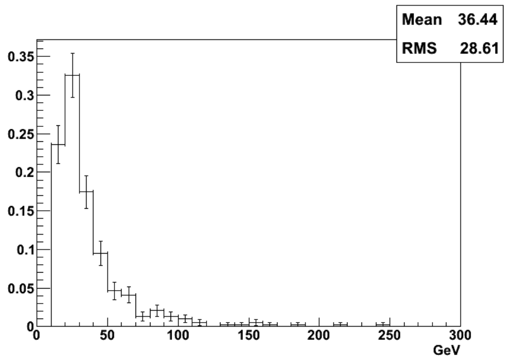

(e) P_T of the electrons as expected from Monte Carlo simulated Standard Model constributions

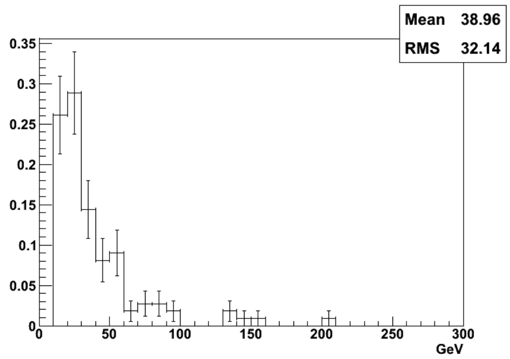

(f) P_T of the electrons in real data from period I recorded at ATLAS during 2010

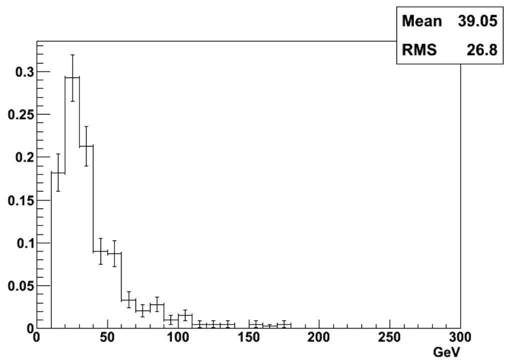

(g) P_T of the muons as expected from Monte Carlo simulated Standard Model contributions

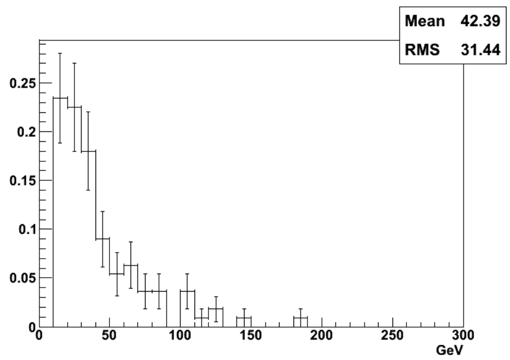

(h) P_T of the muons in real data from period I recorded at ATLAS during 2010

Figure 6.4: Lepton P_T and $\not{E}_T$ compared for Monte Carlo simulated and real data. Errors are statistical.

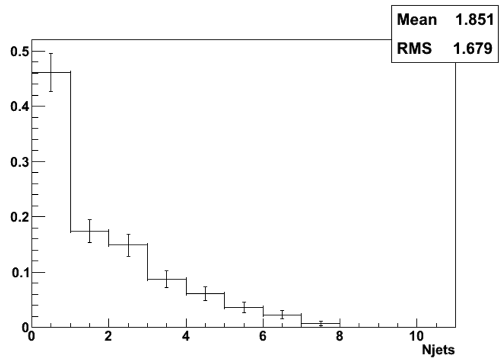

(a) Number of AntiKtH1Topo reconstructed jets as expected from Monte Carlo simulated Standard Model contributions

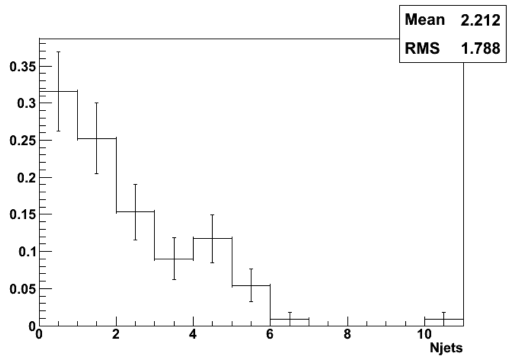

(b) Number of AntiKtH1Topo reconstructed jets in real data from period I recorded at ATLAS during 2010

Figure 6.5: Number of AntiKtH1Topo reconstructed jets for Monte Carlo simulated and real data.

6.5.4 Fit results

The results for the fitted cross sections are listed in Tab. 6.6 for the selection using medium, isolated leptons. The first thing to notice, is that the statistical errors are smaller than for our fit against the Monte Carlo generated control sample. This is expected as the data contains a total integrated luminosity of 20 pb^{-1} compared to the 10 pb^{-1} of the control sample. The value of the fitted cross sections agree well with Standard Model expectations within errors for the medium, isolated sample.

Before concluding anything from this, let us recall that the QCD sample used to estimate the Standard Model QCD contribution to the background contained events corresponding to only 10 pb^{-1} integrated luminosity. The derived shapes will thus be scaled by a factor two. As very few events from QCD pass the selections, these probability shapes will not be very reliable. Whatever might be the explanation, a thorough study of the systematics is needed for a final validation of the method and to compare with theoretical predictions.

Process	$\sigma_i = \frac{\alpha_i N_i}{\Gamma_i A_i \mathcal{L}_i}$ (pb)	stat. errors	syst. error	expected events	events in fit of data
$t\bar{t}$	195	$+58 - 46$	$+16 - 10$	46	43
WW	33	$+36 - 24$	$+6 - 3$	12	6
$Z \to \tau\tau$	843	$+254 - 199$	$+73 - 48$	63	62

Table 6.6: Fitted cross sections for all processes floating after medium, isolated selection in 20 pb^{-1} real data

Slices in N_{jets}

The data fit has, like the control sample fit, been plotted in N_{jets} slices. Figure 6.6 shows this for all slices with data points. It is interesting to see that the data points fit to the distributions within their errors for most slices. A few are slightly above but, bearing in mind the Standard Model expectation shapes also have errors, they are reasonable. The KS test values support that it is a rather good fit. The event recorded with 10 jets does however not fit with any expectations. For the same reason the KS test gives a value of 0. Reconstructing the same event with the Cone4Tower jet algorithm results in 8 jets, so obviously the number of reconstructed jets could be wrong. A further study of the event would be very interesting.

6.5.5 Event display of a 10 jet event from data recorded in 2010

A 10 jet event is very unlikely to come from any of the Standard Model processes with the given selection. Such an event has not been generated for any of the samples considered in this thesis. To investigate this event it has been plotted using the graphical event display tool VP1 [61].

The overview of the event is drawn in Fig. 6.7 with the outline of the TRT switched on. The orange lines are tracks, the green line a particle identified as a muon and the green clusters correspond to transverse energy deposited in the calorimeters. The event is seen to contain predominantly straight tracks indicating, that particles are mostly high P_T . The jets vary in transverse energy, but a total of 10 is reconstructed with P_T above 15 GeV. For the Cone4Tower algorithm only 8 jets are reconstructed in the same event. A simple counting of the jets based on energy deposited in clusters confirms that this is a multi-jet event.

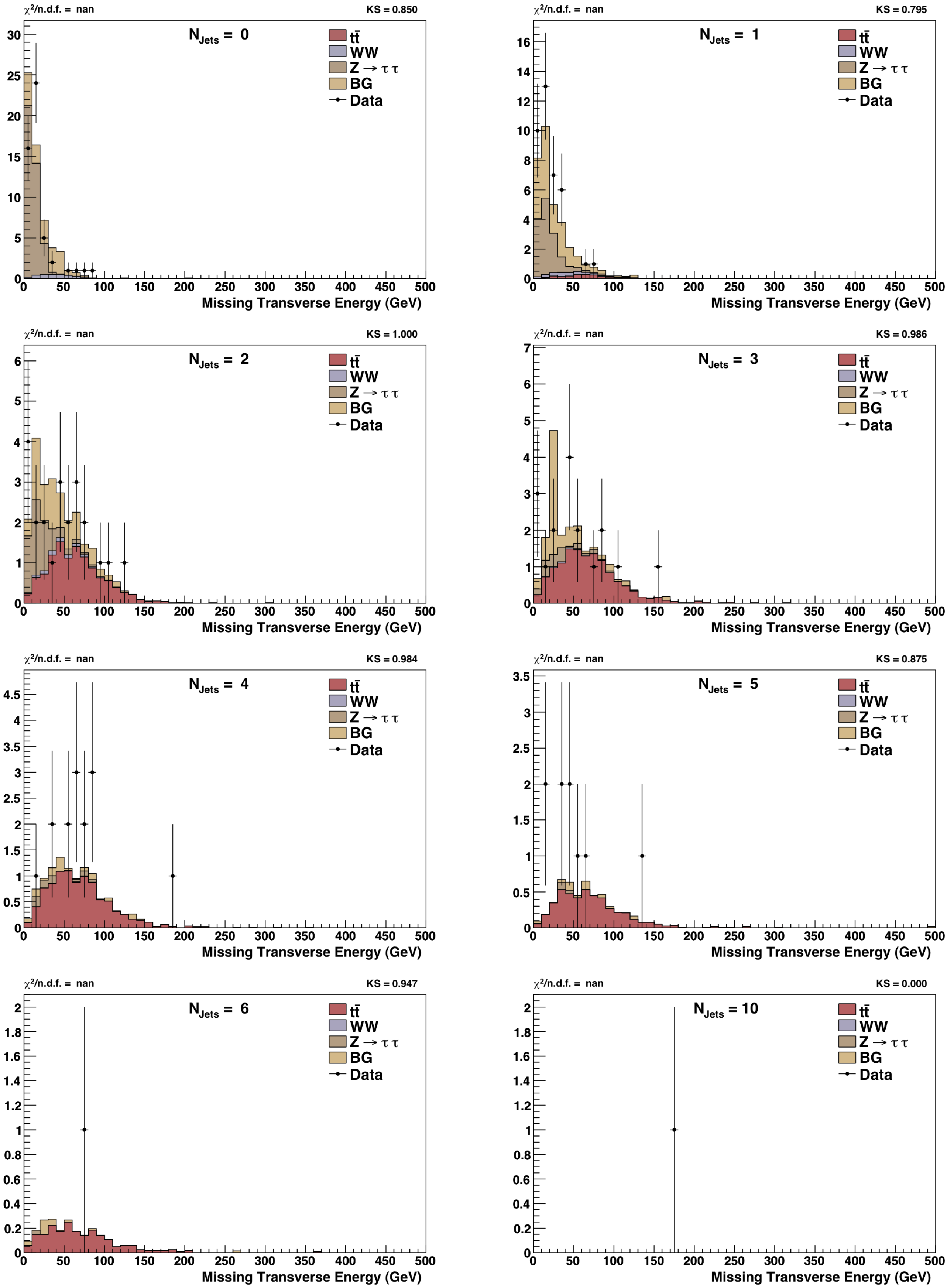

Figure 6.6: Fit values for slices in number of jets for real data from ATLAS recorded in 2010. The sample corresponds to 20 pb^{-1} and errors are statistical.

To probe whether this is indeed a single collision, a close-up of the interaction region is presented. The demand of a silicon hit has been imposed to sort away tracks only reconstructed in the TRT, that might have deviating primary vertices. The primary vertex has been drawn with a blue sphere and the coordinate unit represents 1 mm in each direction, to give a feel for the distances (It should be noted, that the coordinate unit is slightly closer to the viewer than the primary vertex, and that the sphere of the primary vertex is 2 mm in diameter). Some secondary vertices, i.e. tracks that start outside the primary vertex, seem to be present. Most interesting to note, is that there does not seem to be two primary vertices, so from this brief study of the event, pile-up does not seem to be the explanation for the large number of jets in the event. To conclude this a much more thorough study is needed. Nonetheless the event is very interesting and proves, that the method can be used as a probe for interesting and possibly new physics.

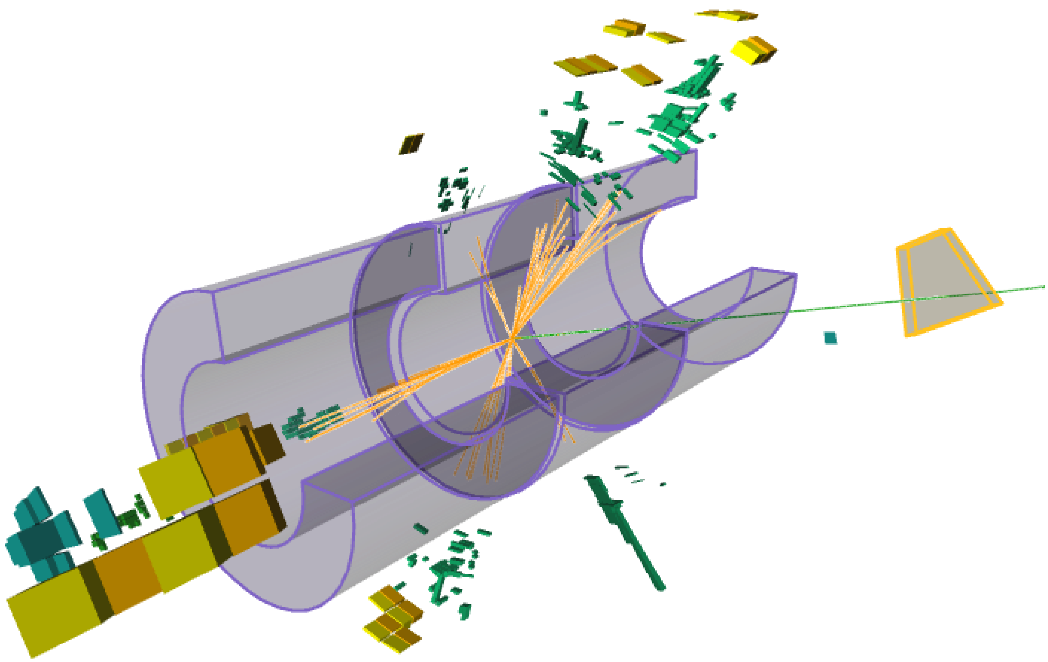

Figure 6.7: Graphical display of a 10 jet event from ATLAS data recorded in 2010, drawn using [61].

6.6 Conclusion

The study of this thesis has shown, that the Standard Model contributions can be separated in an $N_{jets}-\not{E}_T$ phase-space. The background contributions can be suppressed with selection and isolation, leaving clear signal shapes for fitting. From these the cross sections of the Standard Model processes can be fitted.

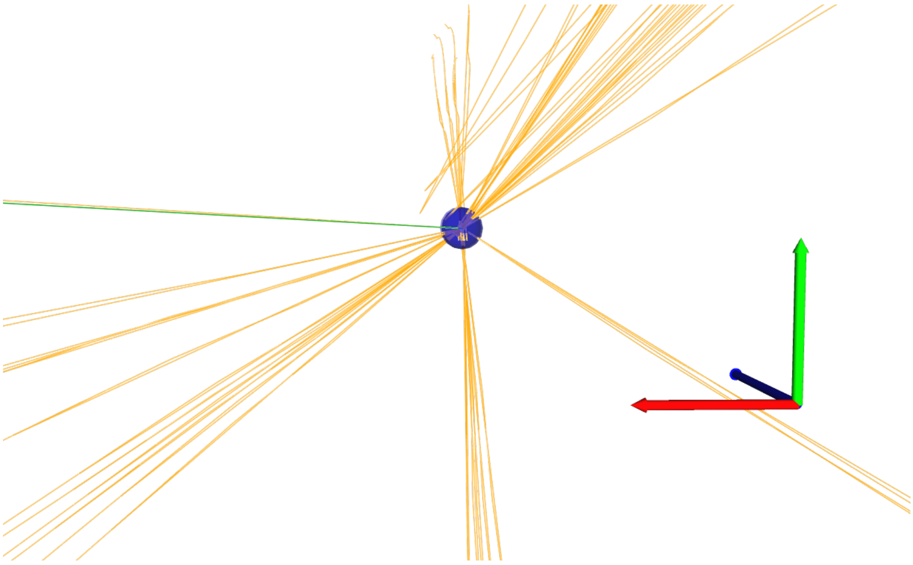

Figure 6.8: Close-up of the 10 jet event from ATLAS data recorded in 2010, drawn using [61]. The axes shown are 1 mm each.

When fitting with the maximum likelihood fit,the resulting $t\bar{t}$ cross section is:

$$\sigma_{t\bar{t}} = 195^{+58}_{-46}(\text{stat})^{+16}_{-10}(\text{syst})\text{pb}. \tag{6.21}$$

The best measurement of the $t\bar{t}$ cross section existing today is from the exclusive measurement [59]:

$$\sigma(t\bar{t}) = 151^{+85}_{-68}(\text{stat})^{+39}_{-26}(\text{syst})\text{pb}. \tag{6.22}$$

A fit of the $t\bar{t}$ cross section with the inclusive method presented in this study gives a significantly better statistical result. The results for WW and $Z\tau\tau$ are:

$$\sigma_{WW} = 33^{+36}_{-24}(\text{stat})^{+6}_{-3}(\text{syst})\text{pb}. \tag{6.23}$$

$$\sigma_{Z\rightarrow\tau\tau} = 843^{+254}_{-199}(\text{stat})^{+73}_{-48}(\text{syst})\text{pb}. \tag{6.24}$$

At the time of writing there exist no measurement of the Z production cross section from the tau channel and no measurement of any diboson production cross section. The measurements of both of these would therefore be very interesting. Any fit performed with this method will be interesting as a comparison to already existing exclusive fits. Furthermore the method could serve as a valuable test of the Standard Model and especially how well our estimates of it behave.

Finally the method is interesting as a probe for new physics. The Standard Model does not predict a significant amounts of events with high $\not{E}_T$ and high N_{jets}, so any signal found in that region is interesting. Various theories that go beyond the Standard Model like Supersymmetry and the idea of microscopic black holes could give rise to high $\not{E}_T$ and large number of jets in a single event.

Appendix A

Appendix

A.1 Calculations regarding the $Z/\gamma *$ cross section in Chapter 3

The amplitude of $e^+e^- \to Z \to \mu^+\mu^-$ is given by the Feynman rules

$$\bar{v}^{s'}(p')(-ie\gamma^\mu)u^s(p)\left(\frac{-ig_{\mu\nu}}{q^2 - m_Z^2}\right)\bar{u}^r(k)(-ie\gamma^\nu)v^{r'}(k'), \tag{A.1}$$

where p and p' are the momentum of e^- and e^+ respectively and k and k' for μ^- and μ^+. This can be rearranged (leaving the spin superscript implicit) into

$$i\mathcal{M}(e^-(p)e^+(p') \to \mu^-(k)\mu^+(k')) = \frac{ie^2}{q^2 - m_Z^2}\left(\bar{v}(p')\gamma^\mu u(p)\right)\left(\bar{u}(k)\gamma_\nu v(k')\right) \tag{A.2}$$

To get the invariant squared matrix, we use that $\bar{v}(p')\gamma^\mu u(p)$ can be complex-conjugated as follows

$$(\bar{v}(p')\gamma^\mu u(p))* = u^\dagger(\gamma^\mu)^\dagger(\gamma^0)^\dagger v = u^\dagger(\gamma^\mu)^\dagger\gamma^0 v = u^\dagger\gamma^0\gamma^\mu v = \bar{u}\gamma^\mu v \tag{A.3}$$

so that we get

$$|\mathcal{M}|^2 = \frac{e^4}{(q^2 - m_Z^2)^2}\left(\bar{v}(p')\gamma^\mu u(p)\bar{u}(p)\gamma^\nu v(p')\right)\left(\bar{u}(k)\gamma_\mu v(k')\bar{v}(k')\gamma_\nu u(k)\right) \tag{A.4}$$

Now we have an expression that can be made simpler as we do not have to keep spins of the leptons. The experiments we will be performing, are not set up to measure the polarisation of particles and we can therefore correctly make the assumption, that we want to compute the spin-averaged matrix element. This adds a factor $\frac{1}{4}$ to our results and means we can forget the spin indices.

$$\frac{1}{2}\sum_s\sum_{s'}\frac{1}{2}\sum_r\sum_{r'}|\mathcal{M}(s, s' \to r, r')|^2 \tag{A.5}$$

After rewriting in spinor indices, and using the following completeness relations

$$\sum_s u^s(p)\bar{u}^s(p) = \not{p} + m \quad \text{and} \quad \sum_s v^s(p)\bar{v}^s(p) = \not{p} - m, \tag{A.6}$$

(where $\not{p} \equiv \gamma^\mu p_\mu$) we get a simplified version of the matrix element expressed with γ matrices as opposed to u and v spinors

$$\frac{1}{4}\sum_{spins}|\mathcal{M}|^2 = \frac{e^2}{(q^2-m_Z^2)^2} tr\left[(\not{p}'-m_e)\gamma^\mu(\not{p}+m_e)\gamma^\nu\right] tr\left[(\not{k}+m_\mu)\gamma_\mu(\not{k}'-m_\mu)\gamma_\nu\right] \quad (A.7)$$

This equation could seem hard to calculate anything meaningful from but luckily there exist a number of tricks for the calculation of traces involving γ matrices. These are thoroughly described in e.g. chapter 5.1 in [3]. For now we simply state that the first trace in Eq. A.7 can be evaluated as

$$tr\left[(\not{p}'-m_e)\gamma^\mu(\not{p}+m_e)\gamma^\nu\right] = 4\left[p'^\mu p^\nu + p'^\nu p^\mu - g^{\mu\nu}(p\cdot p' + m_e^2)\right] \quad (A.8)$$

and similarly for the second part. The electron mass here, is so much smaller than the muon mass, that it can be left out without significant impact, yielding the simple equation which is also in the chapter:

$$\frac{1}{4}\sum_{spins}|\mathcal{M}|^2 = \frac{8e^2}{(q^2-m_Z^2)^2}\left[(p\cdot k)(p'\cdot k') + (p\cdot k')(p'\cdot k) + m_\mu^2(p\cdot p')\right] \quad (A.9)$$

A.2 Datasets used in final shapes

Process	dataset number	atlas release
$Z \to \tau\tau$	106052	r1250_r1260
$t\bar{t}$	105200	r1250_r1260
WW	105985	r1250_r1260
$W \to e\nu \leq 5$ partons	107680-85	r1250_r1260
$W \to \mu\nu \leq 5$ partons	107690-95	r1250_r1260
$W \to \tau\nu \leq 5$ partons	7700-05	r1250_r1260
WZ	105987	r1250_r1260
ZZ	105986	r1250_r1260
single top Wt-channel	108346	r1250_r1260
$Z \to ee$	107650-55	r1250_r1260
$Z \to \mu\mu$	107660-65	r1250_r1260
QCD J1 2-3 partons	107912-13	r1302_r1306
QCD J2 2-6 partons	108818-22	r1302_r1306
QCD J3 2-6 partons	108823-27	r1302_r1306

Table A.1: The official AOD's used in estimating standard model contributions for various processes.

A.3 Signal from reconstructed $e\mu$ without isolation

The initial selection used was with a tight electron and a tight muon of opposite charge and with a P_T above 15GeV. This selection gives a very good idea of the distribution and significance of the various processes. Tab. A.2 gives the value for the signal processes, $t\bar{t} \to e\mu + \nu's$, $WW \to e\mu + \nu's$ and $Z\tau\tau \to e\mu + \nu's$ when selecting true electrons and muon.

In Tab. A.3 the same values are given when selection is based on the tight reconstructed electron and muon. In Tab. A.3 the values for the different processes contributing to or faking the $e\mu$ signal are also listed. Comparing the two tables give efficiencies for the tight selection of around 60-70% for electron and muon respectively, and an efficiency after both cuts of 40-60%. This agrees with the comparable electron reconstruction efficiency value of 61.66 ± 0.07 for $Z \rightarrow ee$ from [46] and muon efficiency from [49] with the slightly higher value of around 80% for muons from $t\bar{t}$. The muon reconstruction efficiencies are much higher for simple reconstruction of the tracks as is the electron efficiency for medium electrons.

Table A.2: Signal from true $e + \mu$ events

Process	Events generated	e μ events selected	acceptance after selection	initial filter-efficiency	after scaling to 1 pb^{-1}
$t\bar{t}$	199828	10818 ± 104	5.4%	0.5	4.8
WW	249837	17457 ± 132.1	6.9%	0.324	1.2
$Z \rightarrow \tau\tau + 0$ partons	303359	2004 ± 45	0.66%	1.0	5.2
$Z \rightarrow \tau\tau + 1$ partons	63481	451 ± 21	0.71%	1.0	1.2
$Z \rightarrow \tau\tau + 2$ partons	19492	166 ± 13	0.85%	1.0	0.42
$Z \rightarrow \tau\tau + 3$ partons	5497	39 ± 6.2	0.71%	1.0	0.094
$Z \rightarrow \tau\tau + 4$ partons	1499	13 ± 3.6	0.87%	1.0	0.031
$Z \rightarrow \tau\tau + 5$ partons	499	9 ± 3.0	1.80%	1.0	0.015

Table A.3: Signal from reconstructed $e + \mu$ events

Process	Events generated	e μ events generated	acceptance after selection	initial filter-efficiency	after scaling to 1 pb^{-1}
$t\bar{t}$	199828	6500 $\pm$ 80.6	3.25%	0.5	2.89
WW	249837	7312 $\pm$ 85.5	2.93%	0.324	0.5228
$Z \to \tau\tau + 0$ partons	303359	807 $\pm$ 28	0.266%	1.0	2.098
$Z \to \tau\tau + 1$ partons	63481	207 $\pm$ 14	0.326%	1.0	0.5382
$Z \to \tau\tau + 2$ partons	19492	78 $\pm$ 8.8	0.400%	1.0	0.195
$Z \to \tau\tau + 3$ partons	5497	19 $\pm$ 4.4	0.346%	1.0	0.0456
$Z \to \tau\tau + 4$ partons	1499	7 $\pm$ 2.6	0.467%	1.0	0.0168
$Z \to \tau\tau + 5$ partons	499	2 $\pm$ 1.4	0.401%	1.0	0.0034
					Total: 6.3
$We\nu \leq 5$ partons	1896152	348 $\pm$ 19	0.018%	-	1.7
$W\mu\nu \leq 5$ partons	1897183	67 $\pm$ 8.2	0.0035%	-	0.34
$W\tau\nu \leq 5$ partons	1876156	36 $\pm$ 6.0	0.0019%	-	0.18
$Wbb \leq 5$ partons	6499	64 $\pm$ 8	0.98%	-	0.038
WZ	249830	1520 $\pm$ 39	0.6%	-	0.021
ZZ	249725	979 $\pm$ 31	0.39%	-	0.0038
$W\mu^+ + \gamma$	50000	17 $\pm$ 4.1	0.034%	-	0.0095
$W\mu^- + \gamma$	49992	23 $\pm$ 4.8	0.046%	-	0.0129
$Z \to ee \leq 5$ partons	394651	22 $\pm$ 4.7	0.0056%	-	0.046
$Z \to \mu\mu \leq 5$ partons	393431	20 $\pm$ 4.5	0.0051%	-	0.042
single top tchan $\to$ e	9993	128 $\pm$ 11	1.28%	-	0.092
single top tchan $\to$ mu	9997	28 $\pm$ 5.3	2.8%	-	0.020
single top tchan $\to$ tau	10000	9 $\pm$ 3.0	0.09%	-	0.0064
single top Wt $\to$ inclusive	14995	261 $\pm$ 16	1.74%	-	0.25
				Total:	2.8
$qcdJ1 + 3$ partons	10497	0	0%	-	0
$qcdJ2 \leq 3$ partons	380820	12 $\pm$ 3.46	0.0032%	-	1.9884
$qcdJ3 \leq 3$ partons	84457	16 $\pm$ 4	0.019%	-	1.6
$qcdbbJ2 + 0$ partons	50981	58 $\pm$ 7.6	0.114%	-	5.7652
$qcdbbJ2 + 1$ partons	40441	22 $\pm$ 4.7	0.0544%	-	2.1802
$qcdbbJ2 + 2$ partons	11498	6 $\pm$ 2.4	0.0522%	-	0.5772
$qcdbbJ2 + 3$ partons	2499	3 $\pm$ 1.7	0.1200%	-	0.2769
$qcdbbJ2 + 4$ partons	500	1 $\pm$ 1	0.200%	-	0.0868
$qcdbbJ3 + 0$ partons	4000	5 $\pm$ 2.24	0.0013%	-	0.4806
$qcdbbJ3 + 1$ partons	11996	22 $\pm$ 4.69	0.183%	-	2.1318
$qcdbbJ3 + 2$ partons	6999	4 $\pm$ 2	0.0572%	-	0.3764
$qcdbbJ3 + 3$ partons	2498	1 $\pm$ 1	0.040%	-	0.0925
$qcdbbJ3 + 4$ partons	1000	2 $\pm$ 1.41	0.20%	-	0.1732
(bb samples used)				Total	QCD: 12.1
				Total	BG: 14.9
					$\frac{S}{B} = 0.42$

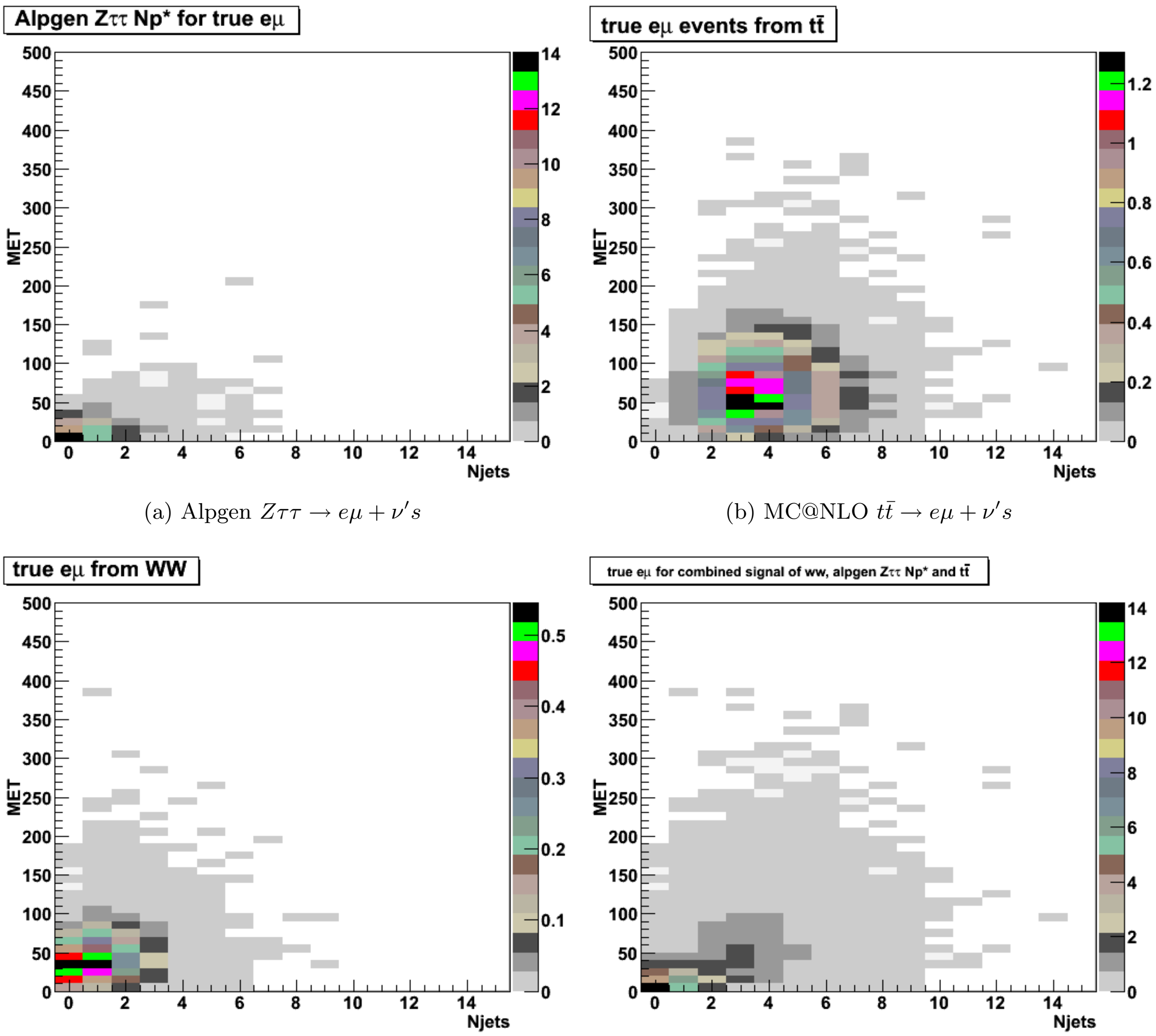

(a) Alpgen $Z\tau\tau \rightarrow e\mu + \nu' s$

(b) MC@NLO $t\bar{t} \rightarrow e\mu + \nu' s$

(c) Herwig $WW \rightarrow e\mu + \nu' s$

(d) MC truth eμ from $Z\tau\tau, t\bar{t}$ and WW

Figure A.1: signal from MC truth $e + \mu$ events

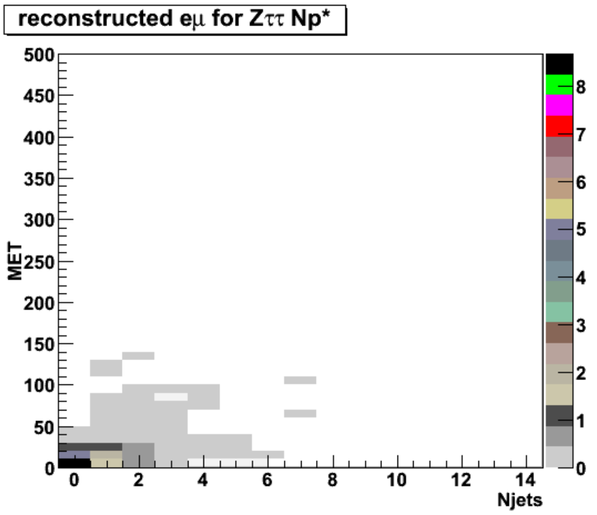

(a) Alpgen $Z\tau\tau \rightarrow e\mu + \nu's$

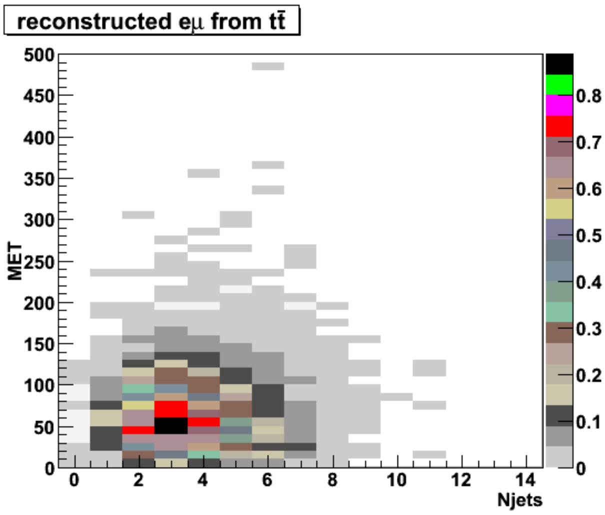

(b) MC@NLO $t\bar{t} \rightarrow e\mu + \nu's$

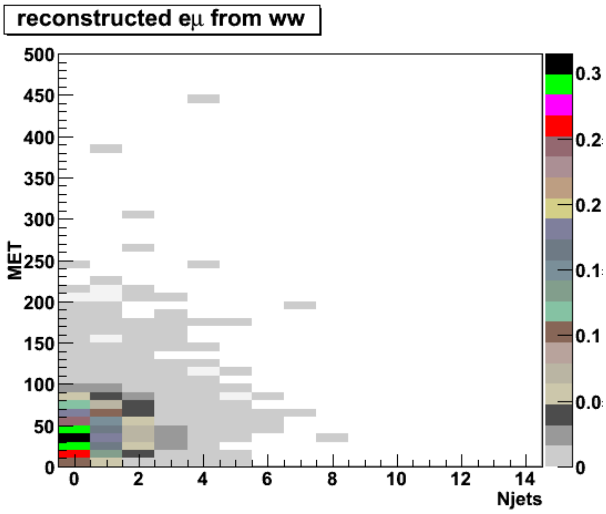

(c) Herwig $WW \rightarrow e\mu + \nu's$

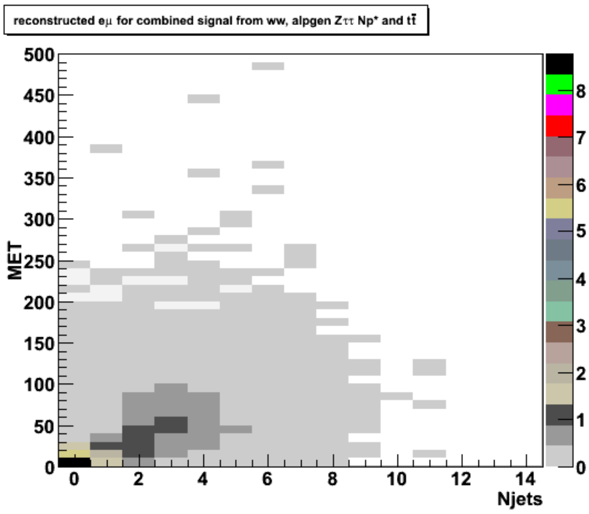

(d) Combined eμ from $Z\tau\tau, t\bar{t}$ and WW

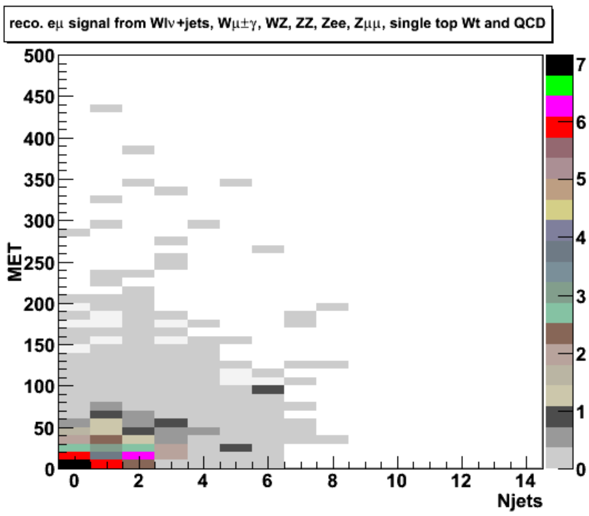

(e) $W + jets, WZ, ZZ, QCD, W + \gamma$

Figure A.2: Signal and background from reconstructed $e + \mu$ events

List of Figures

List of Tables

Bibliography

[1] Sebastian Carron, Mircea Coca, and Mark Kruse. A global analysis of the high-p_T dilepton sample using 200 pb^{-1} of run 2 data - public note. *CDF*, note 7192, 2006.

[2] Ask E. Jensen and Mark Kruse. A global study of e $-\mu$ final states in the $n_{jets} - \not{E}_T$ parameter space for ATLAS. *ATL-COM-PHYS-2010-1067*, 2010.

[3] Michael E. Peskin and Daniel V. Schroeder. *An Introduction to Quantum Field Theory.* Westview Press, 1995.

[4] G. Scharf. *Historical Introduction of Scharf's original book.* Springer, 1995.

[5] Michael E. Peskin and Daniel V. Schroeder. *An Introduction to Quantum Field Theory.* Westview Press, 1995. 77–78 pp.

[6] Jan Ambjorn and Jens Lyng Petersen. *Quantum Field Theory.* København Universitet, 2009.

[7] Michael E. Peskin and Daniel V. Schroeder. *An Introduction to Quantum Field Theory.* Westview Press, 1995. 700–719 pp.

[8] B.R.Martin and G. Shaw. *Particle Physics.* John Wiley and Sons, 2007. 22 - 28 pp.

[9] Shlomo Sternberg. Lie algebras, 1999. preprint November.

[10] Iris Rottländer. *Development of a Benchmark Parameter Scan for Higgs Bosons in the NMSSM model and a Study of the Sensitivity for $H \rightarrow AA \rightarrow 4\tau$ in Vector Boson Fusion with the ATLAS Detector.* PhD thesis, Bonn University, Physics Institute, 2008.

[11] Peter W. Higgs. Broken symmetries and the masses of gauge bosons. *Phys. Rev. Lett.*, 13(16):508–509, Oct 1964.

[12] J. Horejsi. Fundamentals of electroweak theory. *Prague, Czech Republic: Karolinum Pr. 351 p*, 2002.

[13] R W Assmann, M Lamont, and S Myers. A brief history of the lep collider. *Nucl. Phys. B, Proc. Suppl.*, 109(CERN-SL-2002-009-OP):17–31. 15 p, Apr 2002.

[14] Michael E. Peskin and Daniel V. Schroeder. *An Introduction to Quantum Field Theory.* Westview Press, 1995. 545–649 pp.

[15] J. Ohnemus. Order-α calculation of hadronic w^-w^+ production. *Physical Review Letters D*, 44, 1991.

[16] Johan Alwall, Pavel Demin, Simon de Visscher, Rikkert Frederix, Michel Herquet, Fabio Maltoni, Tilman Plehn, David L. Rainwater, and Tim Stelzer. Madgraph/madevent v4: the new web generation. *Journal of High Energy Physics*, JHEP09, 2007.

[17] T. Binoth, M. Ciccolini, N. Kauer, and M. Krämer. Gluon-induced w-boson pair production at the lhc. *Journal of High Energy Physics*, JHEP0612:046, 2006.

[18] Robert W. Seidel. Giant Ring on the Prairie. *Science*, 323(5920):1430–1431, 2009. URL `http://www.sciencemag.org/content/323/5920/1430.short`.

[19] B.R.Martin and G. Shaw. *Particle Physics*. John Wiley and Sons, 2007. 51+ pp.

[20] H. L. Lai et al. Global QCD analysis of parton structure of the nucleon: CTEQ5 parton distributions. *Eur. Phys. J.*, C12:375–392, 2000.

[21] A. D. Martin, R. G. Roberts, W. J. Stirling, and R. S. Thorne. MRST partons and uncertainties. *hep-ph/0307262*, 2003.

[22] A Kupco. Cluster hadronization in herwig 5.9. *hep-ph/9906412*, 1999.

[23] T Sjostrand. Monte carlo generators. oai:cds.cern.ch:999717. *hep-ph/0611247. CERN-LCGAPP-2006-06*, page 23 p, Nov 2006.

[24] S. Mrenna T. Sjöstrand and P. Skands. Pythia 8.135. *Comput. Phys. Comm. 178*, 852, 2008. [arXiv:0710.3820].

[25] G. Corcella, I.G. Knowles, G. Marchesini, S. Moretti, K. Odagiri, P. Richardson, M.H. Seymour, and B.R. Webber. Herwig 6.5. *010 [hep-ph/0011363]; hep-ph/0210213*, JHEP 0101, 2001.

[26] S. Frixione and B.R. Webber. Matching nlo qcd computations and parton shower simulations. *029 [hep-ph/0204244]*, JHEP 0206, 2002.

[27] M.L. Mangano, M. Moretti, F. Piccinini, R. Pittau, and A. Polosa. a generator for hard multiparton processes in hadronic collisions. *hep-ph/0206293*, JHEP 0307:001, 2003.

[28] Michelangelo L. Mangano, Mauro Moretti, Fulvio Piccinini, and Michele Treccani. Matching matrix elements and shower evolution for top-quark production in hadronic collisions. *hep-ph/0611129*, 2006.

[29] Borut Paul Kersevan and Elzbieta Richter-Was. The Monte Carlo event generator AcerMC version 2.0 with interfaces to PYTHIA 6.2 and HERWIG 6.5. *hep-ph/0405247*, 2004.

[30] J. M. Butterworth, Jeffrey R. Forshaw, and M.H. Seymour. Multiparton interactions in photoproduction at HERA. *Z. Phys.*, C72:637–646, 1996.

[31] Elzbieta Richter-Was, Daniel Froidevaux, and Luc Poggioli. ATLFAST 2.0 a fast simulation package for ATLAS atlas note atl-phys-98-131.

[32] J Allison. Geant4 developments and applications. *IEEE Trans. Nucl. Sci.*, 53:270, 2006.

[33] R. Keith Ellis, Chris T. Hill, and Joe D. Lykken. *Perspectives in the standard model: proceedings of the Theoretical Advanced Study Institute in Elemetary Particle Physics.* World Scientific Publishing Co. Pte. Ltd., 1991.

[34] Wikipedia. Higgsless model — wikipedia, the free encyclopedia, 2010. URL `$http://en.wikipedia.org/w/index.php?title=Higgsless_model\&oldid=4000% 35295$`. [Online; accessed 22-December-2010].

[35] B.R.Martin and G. Shaw. *Particle Physics.* John Wiley and Sons, 2007.

[36] ATLAS collaboration. The atlas experiment at the cern large hadron collider. *Journal of Instrumentation*, 3, August 2008.

[37] Ulrik Egede. *The search for a standard model Higgs at the LHC and electron identification using transition radiation in the ATLAS tracker.* PhD thesis, Lund University, Faculty of mathematics and natural sciences, 1998.

[38] E. Laure, C. Gr, S. Fisher, A. Frohner, P. Kunszt, A. Krenek, O. Mulmo, F. Pacini, F. Prelz, J. White, M. Barroso, P. Buncic, R. Byrom, L. Cornwall, M. Craig, A. Di Meglio, A. Djaoui, F. Giacomini, J. Hahkala, F. Hemmer, S. Hicks, A. Edlund, A. Maraschini, R. Middleton, M. Sgaravatto, M. Steenbakkers, J. Walk, and A. Wilson. Programming the grid with glite. In *Computational Methods in Science and Technology*, page 2006, 2006.

[39] C. Amsler et al. (Particle Data Group). 2009 partial update for the 2010 edition. *Physics Letters B667*, 1, 2008.

[40] Emanuele Re. Single-top Wt-channel production matched with parton showers using the POWHEG method. *1009.2450*, 2010.

[41] Atlas Hadronic Calibration Workshop, Tucson, Arizona. *Theoretical aspects of jet-finding*, volume 4th, 14–16 March 2008.

[42] ATLAS collaboration. *Expected performance of the ATLAS experiment: detector, trigger and physics.* CERN, Geneva, 2009. 261-297 pp.

[43] Yuri L. Dokshitzer, G. D. Leder, S. Moretti, and B. R. Webber. Better Jet Clustering Algorithms. *JHEP*, 08:001, 1997.

[44] Gavin P. Salam and Gregory Soyez. A practical seedless infrared-safe cone jet algorithm. *Journal of High Energy Physics*, 2007(05):086, 2007. URL `http://stacks.iop.org/1126-6708/2007/i=05/a=086`.

[45] Gavin P. Salam Matteo Cacciari and Gregory Soyez. *FastJet 2.4.2 user manual*, 2009. URL `www.lpthe.jussieu.fr/$\sim$salam/fastjet/`.

[46] ATLAS collaboration. *Expected performance of the ATLAS experiment: detector, trigger and physics.* CERN, Geneva, 2009. 43-161 pp.

[47] *Performance of E_T miss reconstruction in first ATLAS data*, volume Phenomenology Symposium 10 - 12 May, 2010.

[48] R. Nicolaidou, L. Chevalier, S. Hassani, J.F. Laporte, E. Le Menedeu, and A. Ouraou. Muon identification procedure for the atlas detector at the lhc using muonboy reconstruction package and tests of its performance using cosmic rays and single beam data. *Journal of Physics: Conference Series*, 219, 2010.

[49] ATLAS collaboration. *Expected performance of the ATLAS experiment: detector, trigger and physics*. CERN, Geneva, 2009. 161-229 pp.

[50] R Nicolaidou, L Chevalier, S Hassani, J F Laporte, E Le Menedeu, and A Ouraou. Muon identification procedure for the atlas detector at the lhc using muonboy reconstruction package and tests of its performance using cosmic rays and single beam data. *Journal of Physics: Conference Series*, 219(3):032052, 2010. URL `http://stacks.iop.org/1742-6596/219/i=3/a=032052`.

[51] The atlas metadata interface, ami: http://ami.in2p3.fr/. URL `http://ami.in2p3.fr/`.

[52] J. Butterworth et al. Single boson and diboson production cross sections in pp collisions at sqrts=7 tev. *ATL-COM-PHYS-2010-695*, (31.08.2010).

[53] *ATLAS Search Strategy for Single Top Production*, Jun 2010.

[54] Luc Demortier and Louis Lyons. Everything you always wanted to know about pulls. *CDF/ANAL/PUBLIC/5776*, Version 2.10, August 20, 2002.

[55] F. James. Minuit reference manual, version 94.1.

[56] Alfio Lazzaro and Lorenzo Moneta. Minuit package parallelization and applications using the roofit package. *J. Phys.: Conf. Ser.*, 219 042044, 2010.

[57] Glen Cowen. *Statistical Data Analysis*. Clarendon Press - Oxford, 1998.

[58] ATLAS. the top working group draft on top cross section. *ATL-COM-PHYS-2010-855*, 2010/2011.

[59] ATLAS. Supporting document for the dilepton channel for top working group draft on top cross section. *ATL-COM-PHYS-2010-856*, 2010/2011.

[60] ATLAS collaboration. Measurement of the $W \rightarrow l\nu$ and $Z/\gamma* \rightarrow ll$ production cross sections in proton-proton collisions at $\sqrt(s) = 7$ TeV with the ATLAS detector. *1010.2130*, 2010.

[61] The vp1 graphical tool for event displays: http://atlas-vp1.web.cern.ch/atlas-vp1/index.php. URL `http://atlas-vp1.web.cern.ch/atlas-vp1/index.php`.